1989

Use of Infrared Piezobirefringence for Observation of Dislocations in Semiconductors With Cubic Symmetry.

Aloke Kumar Dutta
Louisiana State University and Agricultural & Mechanical College

Order Number 9025301

Use of infrared piezobirefringence for observation of dislocations in semiconductors with cubic symmetry

Dutta, Aloke Kumar, Ph.D.

The Louisiana State University and Agricultural and Mechanical Col., 1989

U·M·I
300 N. Zeeb Rd.
Ann Arbor, MI 48106

USE OF INFRARED PIEZOBIREFRINGENCE FOR OBSERVATION OF DISLOCATIONS IN SEMICONDUCTORS WITH CUBIC SYMMETRY

A Dissertation

Submitted to the Graduate Faculty of the
Louisiana State University and
Agricultural and Mechanical College
in partial fulfillment of the
requirements for the degree of
Doctor of Philosophy

in

The Department of
Electrical and Computer Engineering

by
Aloke Kumar Dutta
B.E.E., Jadavpur University, 1982
M.S., Louisiana State University, 1985
December 1989

ACKNOWLEDGMENTS

I wish to express my sincere gratitude and thanks to my major professor, Dr. Pratul K. Ajmera, for his invaluable support, guidance, assistance, encouragement, and friendly attitude throughout my doctoral program. I would like to acknowledge support from Dr. Burke Huner who provided valuable assistance in all phases of this work. I would also like to extend my appreciation to Dr. Craig S. Hartley with whom important discussions were held during the early phases of this work. Special thanks go to Dr. Alan H. Marshak for providing me with financial assistance through a teaching assistantship during the last two years of my program.

I am especially grateful to my brother-in-law and sister, Drs. Subhash and Manju Basu of University of Notre Dame, without whose moral and financial support, I would not be where I am today. I would like to thank my parents for standing by my side through the adversities.

I express my thanks to all the faculty members and students of the Department of Electrical Engineering with whom I have had many interactions during my stay here at LSU. Last, but not the least, I want to thank the most important person in my life, my wife Ruchira, for her love, understanding, support, and encouragement - which made the tough periods bearable.

The research reported herein was sponsored by the U.S. Army Research Office (Grant# DAAG29-84-K-0153) and its support is sincerely acknowledged. Special thanks also go to Mr. Warren Kirsch of Ethyl Corporation for providing GaAs samples used in this study.

TABLE OF CONTENTS

	Page
ACKNOWLEDGMENTS	ii
TABLE OF CONTENTS	iv
LIST OF TABLES	vii
LIST OF FIGURES	viii
ABSTRACT	xv
CHAPTER 1. INTRODUCTION	1
1.1 Outline of the Technique Used	3
1.2 Literature Review	4
1.3 Scope of the Present Work	16
CHAPTER 2. IMAGE SIMULATIONS	17
2.1 Introduction	17
2.2 Background	17
2.3 Semiconductor Discs under Diametrical Compression	19
2.4 Dislocations in Crystals	28
2.4.1 Edge Dislocations	36
2.4.2 Screw Dislocations	38
2.4.3 Mixed Dislocations	40
2.5 Use of the Algorithm for Some Special Cases	53
2.5.1 An edge dislocation with the dislocation line along the <100> direction and the Burger vector on (001) plane on a (100) oriented sample	54

TABLE OF CONTENTS (contd.)

Page

2.5.2 A screw dislocation with the dislocation line along the <010> direction and the Burger vector on (001) plane on a (100) oriented sample 57

2.5.3 A mixed dislocation with the dislocation line along the <110> direction and the Burger vector on (001) plane on a (111) oriented sample with an angle κ between the dislocation line and the Burger vector 58

2.5.4 A mixed dislocation with the dislocation line along the <110> direction and the Burger vector on (001) plane on a (100) oriented sample with an angle κ between the dislocation line and the Burger vector 60

CHAPTER 3. RESULTS AND DISCUSSIONS 63

3.1 Experimental Setup 63

3.2 Results for Diametrically Compressed Semiconductor Discs 69

3.3 The Stress-Optic Coefficient 79

3.4 Results for Dislocation Images 88

CHAPTER 4. SUMMARY, CONCLUSIONS AND RECOMMENDATIONS 108

REFERENCES 112

TABLE OF CONTENTS (contd.)

Page

APPENDICES 120

A. Calculation of the Direction Cosines between the Sample Axes and the Crystal Principal Axes for a {100} Oriented Sample under any Arbitrary Direction of Loading 120

B. Calculation of the Direction Cosines between the Sample Axes and the Crystal Principal Axes for a {111} Oriented Sample under any Arbitrary Direction of Loading 122

C. Derivation of the Piezooptic Coefficients for Gallium Arsenide from the Elastooptic Coefficients and the Stiffness Constants 129

D. Proof that pure screw dislocations cannot be viewed end-on 136

VITA 139

LIST OF TABLES

Table		Page
2.1	Conversion technique from tensor to reduced notation.	24
2.2	The piezooptic coefficients for Si used in computation (after [14]).	29
2.3	The piezooptic coefficients of GaAs as derived from data of Booyens and Basson [47]. . . .	29
2.4	Most favorable orientations of the dislocation line and the Burger vector for a cubic lattice (after [8]).	54
C.1	The values of the elastooptic coefficients (p_{ij}) and the stiffness (c_{ij}) for GaAs after Booyens and Basson [47]. (p_{ij} are dimensionless, c_{ij} are in dyne/cm^2)	134

LIST OF FIGURES

Figure		Page
2.1	The sample geometry. Axis x_3'' is the outward normal from the plane of the paper.	20
2.2	A simple edge dislocation. ABCD is the dislocation slip plane, AD is the dislocation line perpendicular to the slip vector (after [4]). .	31
2.3	A simple screw dislocation. ABCD is the dislocation slip plane, AD is the dislocation line parallel to the slip vector (after [4]). . . .	32
2.4	Another view of a screw dislocation. The dislocation line AD (of which only the end A is visible) is parallel to the line BC and is parallel to the slip vector. The crystal can be viewed as a single atomic plane in the form of a helicoid, or a spiral ramp (after [4]).	33
2.5	FS/RH Burger's circuit in a) an imperfect crystal and b) a perfect crystal. $\bar{\xi}$ points into the paper (after [10]).	34
2.6	An edge dislocation with the Burger vector $\bar{b}$ perpendicular to the sense of the dislocation $\bar{\xi}$. The coordinate system (x_1,x_2,x_3) is used to represent the stresses.	37

LIST OF FIGURES (contd.)

Page

2.7 A screw dislocation with the Burger vector parallel to the dislocation line. The coordinate system (x_1, x_2, x_3) is used to represent the stresses. 39

2.8 A mixed dislocation with its Burger vector inclined at an angle κ to the dislocation line. 41

2.9 The sample coordinate system (x_1''', x_2''', x_3'''). Axis x_3''' comes out from the plane of the paper. . . . 43

2.10 The relation between the sample axes system (x_1''', x_2''', x_3''') and the crystal principal axes system (x_1', x_2', x_3') for a {100} oriented sample. . . 47

2.11 a) The relation between the three axes systems and b) the axes systems as seen looking along direction x_1'''. 59

2.12 The three axes systems as seen looking along direction x_2'''. 61

3.1 a) The general view and b) the schematic arrangement of the experimental setup. 64

3.2 The spatial sensitivity of the laser (Jodon HN-50) used in this work. 65

3.3 Typical signal output with illumination for the Hamamatsu (C-1000-03) vidicon camera. . . . 68

LIST OF FIGURES (contd.)

Page

3.4 The arrangement for application of compressive load on samples. 70

3.5 a) Experimentally observed and b) simulated image on a {111} oriented silicon disc of radius 0.873 cm and thickness 1.6 mm under a diametrical compression load of 19 kg and angle of polarization α = 90°. Arrows indicate the loading direction. 71

3.6 a) Experimentally observed and b) simulated image on a {111} oriented silicon disc of radius 0.873 cm and thickness 1.6 mm under a diametrical compression load of 38 kg and angle of polarization α = 90°. Arrows indicate loading direction. 73

3.7 a) Experimentally observed image reported by Appel et al.[20] for a silicon sample of unknown orientation with a radius of 4.37 mm, thickness of 1.88 mm, load of 38 kg, and the angle of polarization α = 60°. b) Simulated image for the same conditions as a) for {100} oriented sample. c) Simulated image for the same conditions as a) for {111} oriented sample. Arrows indicate the loading direction. 74

LIST OF FIGURES (contd.)

Page

3.8 a) Simulated and b) experimentally obtained image on a {100} oriented gallium arsenide disc 1.9 cm in diameter and 1.65 mm in thickness under a diametrical compression load of 20 kg, and angle of polarization $\alpha = 0°$. Arrows indicate the loading direction. 76

3.9 a) Simulated and b) experimentally obtained image on a {100} oriented gallium arsenide disc of diameter 1.9 cm and thickness 1.65 mm under a diametrical compression load of 40 kg and angle of polarization $\alpha = 45°$. Arrows indicate the loading direction. 78

3.10 Wafer map of the computed values of the stress-optic coefficient C for a) $\phi = 45°$ and b) $\phi = 75°$ for a load of 19 kg for a {100} oriented silicon wafer with diameter of 1.746 cm and thickness of 1.6 mm. Plotted in 11 levels of a linear gray scale with white for $C > 2.95 \times 10^{-12}$ cm²/dyne and black for $C < 2.05 \times 10^{-12}$ cm²/dyne. Arrows indicate the loading direction. 83

LIST OF FIGURES (contd.)

Page

3.11 Wafer map of the computed values of the stress-optic coefficient C for a) $\phi = 45°$ and b) $\phi = 75°$ for a load of 20 kg for a {100} oriented gallium arsenide wafer with diameter of 1.9 cm and thickness of 1.65 mm. Plotted in 10 levels of a linear gray scale with white for $C > 2.5 \times 10^{-12}$ cm²/dyne and black for $C < 0.9 \times 10^{-12}$ cm²/dyne. Arrows indicate the loading direction. . . . 84

3.12 Simulation results for a pure edge dislocation with the dislocation line along the <100> direction and the Burger vector on (001) plane for a (100) oriented silicon sample. The incident light is along the dislocation line. . . . 89

3.13 Simulation results for a pure screw dislocation with the dislocation line along the <010> direction and the Burger vector on (001) plane pointing along <010> direction for a (100) oriented silicon sample. The viewing direction is along the <100> axis. 90

3.14 Simulation results for a mixed dislocation with the dislocation line along the <100> direction and the Burger vector on (001) plane making 45° angle with the dislocation line for a (100) oriented silicon sample. 93

LIST OF FIGURES (contd.)

Page

3.15 Simulation results for a mixed dislocation with the dislocation line along the <010> direction and the Burger vector on (001) plane making 45° angle with the dislocation line for a (100) oriented silicon sample. 95

3.16 Simulation results for a mixed dislocation with the dislocation line along the <110> direction and the Burger vector on (001) plane making an angle of 45° with the dislocation line for a (100) oriented silicon sample. 96

3.17 Simulation results for a mixed dislocation with the dislocation line along the <110> direction and the Burger vector on (001) plane making an angle of 60° with the dislocation line for a (111) oriented silicon sample. 97

3.18 Experimentally observed image on (100) oriented silicon sample #8 for the polarization angle of 0°. Magnification ×40. 99

3.19 Experimentally observed image on (100) oriented silicon sample #8 for the polarization angle of 45°. Magnification ×40. 100

LIST OF FIGURES (contd.)

Page

3.20 Experimentally observed image on (100) oriented silicon sample #5 for the polarization angle of 45°. Magnification ×40. 102

3.21 Experimentally observed image on (100) oriented silicon sample #5 for the polarization angle of 0°. Magnification ×40. 103

3.22 Experimentally observed image on (100) oriented silicon sample #6 for the polarization angle of 0°. Magnification ×40. 105

3.23 Experimentally observed image on (100) oriented silicon sample #6 for the polarization angle of 45°. Magnification ×40. 106

A.1 The loading and the crystal principal axes systems for a {100} oriented plane. 121

B.1 The loading axes coordinate system. 123

B.2 The crystal axes system and its orientation with respect to the plane of the wafer. 124

B.3 The (x_1, x_2, x_3) coordinate system and its relationship to the loading axes system and the crystal principal axes system. 125

ABSTRACT

The use of infrared piezobirefringence for characterization of defects in cubic semiconductor materials is investigated in this work. Under stress, these normally isotropic materials become birefringent. The stress can result from an applied external load or from defects present in the material. Defects can be generated in the material during its growth and/or processing. As a first step towards defect characterization, the case of diametrically loaded discs of semiconductor materials was simulated. This was done to obtain a better understanding of the simulation algorithm prior to its subsequent use in dislocation characterization. A dark-field plane polariscope was constructed using a He-Ne laser tuned to 1.15 μm wavelength as the light source. The computer simulated images matched well with the experimentally observed ones on diametrically loaded discs of silicon and gallium arsenide.

The behavior of the stress-optic coefficient C was also investigated, which has been treated as a constant by other investigators in earlier works. In this work, it was found that for (100) oriented Si and GaAs discs under diametrical compression, the stress-optic coefficient C is a strong function of position for a given load, and also changes with the direction of the applied load with respect to the principal crystal axes. However, no such dependence was found

for (111) oriented Si and GaAs discs under diametrical compression, as expected from the crystal symmetry. The values of C for (100) oriented Si disc under diametrical compression ranged from 2.0×10^{-12} $cm^2/dyne$ to 3.0×10^{-12} $cm^2/dyne$ and for (100) oriented GaAs disc under diametrical compression ranged from 0.8×10^{-12} $cm^2/dyne$ to 2.6×10^{-12} $cm^2/dyne$ for the cases investigated. The corresponding figures for (111) oriented Si and GaAs discs under diametrical compression are 2.33×10^{-12} $cm^2/dyne$ and 1.94×10^{-12} $cm^2/dyne$ respectively.

Next, an accurate algorithm was developed for the simulation of the images of dislocations as a function of the sample orientation, the orientation of the dislocation line with respect to the principal crystal axes, the orientation of the Burger vector with respect to the dislocation line, and the polarization angle of the incident light. An image data bank has been created for different dislocations. This data bank can be utilized to obtain an accurate characterization of the image of a dislocation by comparing the experimentally obtained images with the simulated ones. In this work, images of the dislocations were observed experimentally and were matched with the simulated images. This approach provides a fast, non-destructive alternative technique for defect characterization in semiconductor materials.

CHAPTER 1

INTRODUCTION

Defects in semiconductor crystals play a significant role in the final yield of a manufacturing process, where the yield is defined as the number of good integrated circuit chips on a wafer divided by the total number of chips on the wafer. The defects also have a significant impact on device terminal properties as it affects parameters such as minority carrier lifetime, carrier mobility, carrier generation rate, and the impurity diffusion rate. These factors can lead to poor reliability of the device and/or low circuit yield. An efficient way of characterizing these defects will not only help improve the yield of the manufacturing process, but may also help improve the device performance.

Any imperfection in the periodicity of a perfect crystal lattice results in a defect. Defects can be classified into three groups namely the point defects, the line defects, and the plane defects. Point defects involve single atom vacancies, interstitials, or vacancy-interstitial pairs. Line defects are arrays of point defects. A line defect is also known as a dislocation and is generally classified as an edge dislocation or a screw dislocation or a mixed dislocation. Plane defects are combinations of dislocations such as twin planes, grain boundaries, and stacking faults. Point defects are generally too microscopic to cause major

catastrophe in a device. However, dislocations do occur during the growth and the subsequent processing of a wafer and hence, are of some concern. The primary objective of this work is to non-destructively detect line defects in semiconductor materials in an accurate and efficient manner.

Some of the commonly used techniques for materials characterization are given elsewhere [1]. Of these, the most commonly used technique today for characterizing dislocations in a semiconductor sample is X-ray topography [2]. This technique is based on the theory of the diffraction of X-rays from crystal planes. The diffracted beams from each set of planes follow a defined pattern. However, if that plane contains any dislocation, then the diffracted beam will be different and the resulting image of the dislocation can be characterized. An excellent treatise on how to accurately characterize a dislocation using X-ray topography is given elsewhere [2]. The average characterization time of each sample by this technique is of the order of one to two days due to relatively long exposure time needed for characterizing each wafer. This fact precludes testing of each individual sample, and the usability of a wafer lot is determined by statistical estimates. The fact that all the wafers are not tested allows the possibility of some defective wafers in a lot to pass through. Therefore, a technique which is accurate, and efficient in that it permits characterization of each sample in a reasonable time is

likely to improve the circuit yield and the device performance. The infrared piezobirefringence technique considered in this work has the potential to be one such technique.

Section 1.1 gives the outline of the infrared piezobirefringence technique. A literature review of the work done in this field is given in Section 1.2. Section 1.3 describes the scope of the proposed work.

1.1 Outline of the Technique Used

Certain optically isotropic crystalline materials become anisotropic with two indices of refraction when stressed. This phenomenon of stress-induced splitting of the refractive index into two components is known as piezobirefringence. The materials which show piezobirefringence are known as photoelastic materials. Silicon and gallium arsenide, the two main semiconductors of interest to the device fabrication industries are piezobirefringent materials. Both silicon and gallium arsenide are opaque to visible light but are transparent in the near infrared. Silicon having a band gap of 1.12 eV has an absorption cutoff at 1.11 μm wavelength. The corresponding values for gallium arsenide are 1.42 eV and 0.89 μm, respectively. A radiation with wavelength longer than 1.11 μm will normally pass through these two materials. Since the radiation does not experience any relative phase change while traversing

through an optically isotropic sample, a dark image results when a stress-free sample is placed between the polarizer and the analyzer with their axes crossed.

However, under stress, the semiconductor sample becomes birefringent. The stress can be either applied externally by loading or generated internally due to defects caused by processing and/or material preparation. The radiation while passing through the stressed regions of the sample splits into two components in mutually orthogonal directions having different refractive indices and thus velocities along the two directions. A phase difference builds up between the two components as they traverse the sample. Now, if the sample is placed between a polarizer and an analyzer with their axes crossed, an image characteristic of the phase shift between the two components can be seen. The stress fields associated with each type of defect will be different and thus different fringe patterns or images will be seen for different types of defects such as an edge dislocation or a screw dislocation. Since infrared radiation is used to observe these defects, this technique is termed infrared piezobirefringence.

1.2 Literature Review

The dislocations in crystals are well known. The types of dislocations and the stress fields that they produce are

described by various authors [3-10]. The elastic displacements and the energy of arbitrarily oriented dislocations for crystalline materials are given by Eshelby [3]. Eshelby et al. [5] have derived the general displacement equations and stress and strain fields of dislocations. They presented the guidelines for obtaining the stiffness constants for any arbitrary orientation of the dislocation line with respect to the principal crystal axes. For stress fields which are independent of one coordinate, for example a pure edge dislocation, the discontinuity in the displacement is equal to the lattice translation vector or the slip vector. This vector is also known as the Burger vector and is defined as the shortest vector connecting two atoms in the crystal which have identical surroundings. A more formal definition of the Burger vector will be given in Section 2.4.

Spence [6] developed formulae for the stress components of dislocations in hexagonal and cubic crystals. He took crystal anisotropy into account and came to a very important conclusion that the form of the stress components in the symmetry directions are similar to those for isotropic solids. Chou [7] used the theory of anisotropic elasticity to analyze the stress field of a single dislocation, the force between two parallel dislocations, and the stress fields of various types of infinite dislocation arrays for a hexagonal crystal.

In a second study, Chou [8] found the stress fields of cubic crystals taking crystal anisotropy into account. He obtained the values of the stiffness constants depending on the orientation of the dislocation line and the Burger vector from the isotropic stiffness constants. The effect of crystal growth parameters such as pull rate and rotation rate on the dislocation density and the residual stress distributions in Czochralski-grown silicon crystals have been discussed by DeNicola and Tauber [11]. The refractive indices of silicon and germanium at different wavelengths have been measured by Briggs [12].

Use of piezobirefringence for the evaluation of stresses within a material has been investigated by a number of authors [13-21]. Poindexter [13] observed the phenomenon of piezobirefringence in diamond and gave its piezooptic coefficients. He found that in diamond, the piezobirefringence does not significantly depend on the orientation of the sample. The first paper on piezobirefringence studies in silicon was published by Giardini [14]. He carried out a stress-birefringence investigation on high purity silicon at a wavelength of 1.11 μm, and obtained the values of its piezooptic coefficients. He established experimentally the linearity of the stress-optical relationship in silicon upto stress values of approximately 450 kg/cm^2. The birefringence in silicon caused by residual stresses due to rapid cooling of large samples was investigated by Hornstra and

Penning [15]. This caused plastic deformation, and subsequently, dislocations. They calculated the stress-optical constant from a comparison of the tensile stress and the optical phase difference. The values were somewhat smaller than those reported by Giardini [14]. Prussin and Stevenson [16] evaluated the average value for the stress-optic coefficient C for silicon by subjecting bars of silicon to pure bending.

Lederhandler [17] used infrared birefringence to relate the presence of birefringence in silicon to two factors: i) plastic deformation caused by the severe thermal gradients during crystal growth and ii) work damage caused by surface abrasion, sand blasting, or diamond saw cutting. Because the birefringence pattern remains unaffected in samples, he termed the strain produced by plastic deformation as 'frozen-in' strain. The strain produced by the work damage was termed 'elastic' strain, because the strain pattern changed with a change in the sample geometry. He was able to obtain an average value for the stress-optic coefficient C for silicon. Schimdt-Tiedemann [18] found the value of the stress-optic coefficient of germanium. He used a xenon arc light source with an interference filter for wavelength range of about 2.2 μm, and a PbS detector.

Work on photoelastic constants of GaAs and Si were initiated by Nikitenko and Martynenko [19]. Their results

showed that the photoelastic constants were strongly dependent upon the wavelength of the light source used. They, however, did not give the absolute values of the constants. Appel et al. [20] devised a dark-field polariscope for infrared photoelastic studies of semiconductors. They presented the fringe patterns produced by externally applied forces on silicon using a wavelength of 1.1 μm. They assumed a constant value for the stress-optic coefficient C. Pictures of residual strain in silicon boules viewed parallel to the growth axis were given, and the quantitative values of the frozen-in strain were obtained by comparing the fringe order with the fringe value. Carron and Walford [21] compared the X-ray topography and the infrared birefringence techniques used for the study of the stresses induced in single crystal silicon wafers by electron-beam heating. Their results indicated that the patterns were created by the thermally induced stresses surrounding the electron-beam spot areas, and both techniques produced almost identical pictures.

Several papers have been published on the use of stress-induced birefringence or piezobirefringence for the observation of dislocations in crystals [22-41]. However, no work has so far been presented which can be effectively used for characterization of dislocations in semiconductor samples in a systematic fashion using this technique. The work which has been done in the area of dislocation detec-

tion is quite large and diverse. The pioneering work on dislocation detection was carried out by Bond and Andrus [22]. They were the first to photograph the images of dislocations using infrared piezobirefringence. However, they did not explain the images analytically. Fathers and Tanner [23] observed that screw dislocations in Barium Titanate viewed along the dislocation axis were invisible and commented that this happened because the refractive indices are independent of the stress field. Chuan-Zhen et al. [24] reported the images of screw dislocations viewed along the dislocation axis in Gadolinium Gallium Garnet (GGG) and Yttrium Aluminum Garnet (YAG) crystals. However, it is not clear what they really observed, as theoretically a screw dislocation cannot be viewed along its axis.

The first comprehensive work on imaging of dislocations in silicon using infrared birefringence was carried out by Bullough [25]. He gave the theoretical intensity distribution of edge dislocations in silicon for both plane and circularly polarized light. He, however, assumed a constant value for the stress-optic coefficient C in his work. He acknowledged, however, that the latter would be a function of position for a cubic crystal. In order to match his calculations with the observations of Bond and Andrus [22], Bullough adjusted the value of C. In the derivation of the intensity distribution, he failed to take into account the crystal orientation, the orientation of the dislocation line

with respect to the principal crystal axes, and the orientation of the Burger vector with respect to the dislocation line, and how the image is affected by the polarization angle of the incident light.

Indenbom and Tomilovskii [26] investigated the nature of glide lines. They observed that the density of dislocations uniquely defines the macroscopic stresses bordering the glide lines. They found that if the dislocation lines were curved or inclined with respect to the field of observation, the effects of the dislocation lines were superimposed and the individual dislocations could not be resolved. This same difficulty was encountered by Prescott and Basterfield [27] who studied dislocation lines in YAG. However, they noted that dislocations inclined to the surface normal were still observable, although it was not possible to accurately determine their Burger vectors. This observation was verified by Matthews et al. [28].

Indenbom et al. [29,30] were the first to predict and observe rosette patterns in the dislocation images. However, in their analysis they too assumed a constant value of C and thus could not predict how the images would be affected by varying orientations of the dislocation lines with respect to the crystal principal axes and varying orientations of the Burger vector with respect to the dislocation line. In some cases, all the rosette petals were

bright while in others the petals were alternately dark and bright. They explained the latter by suggesting that crystals have some built-in stresses associated with them. In places where these stresses compensate the stresses caused by dislocations, dark petals result. Whereas, in places where the built-in stress does not interfere with those produced by dislocations, all the rosettes are bright. This strain, known as the 'background' strain, was taken into consideration in the quantitative analysis of piezobirefringent dislocation images in transparent materials by Jenkins and Hern [31].

In his paper, Indenbom et al. [29] reported that the birefringence rosettes were most clearly visible when the dislocation lines were parallel to the viewing direction, and became less distinct with increasing inclination. The form of the rosette is determined by the angle between the slip plane and the polarization direction. When this angle was zero, the birefringence image of an edge dislocation consisted of six petals, and when the angle was 45°, the image contained four petals.

Indenbom et al. [30] were successful in imaging the birefringence pattern produced by the stresses surrounding etch pits. They found dislocations associated with each etch figure, concluding that probably the etch figures represent the end of atomic dislocations. Jenkins et al. [32]

observed images of dislocation lines due to birefringence in (111) oriented silicon wafers. They used Sirtl etch to develop etch pits at the points on the surface where the dislocation lines emerge and observed that some etch pits did not have any dislocation lines associated with them. Hence, etch pits do not necessarily appear to represent the ends of atomic dislocations.

Nikitenko and Dedukh [33] calculated the stress distribution around edge dislocations. They also commented on why the calculation of the Burger vector is difficult from the experimental birefringence images. First, the resolution is limited by the wavelength of light used. Second, the stress field of a dislocation is affected by the stress fields of other dislocations and internal stresses within the crystal.

Tanner and Fathers [34] derived the intensity distribution around dislocations using the same assumptions as Bullough [25]. Indenbom and Tomilovskii [35] observed dislocations in corundum crystals placed between crossed polarizers. Matthews et al. [36] observed dislocations in very large crystals of GGG by using stress-induced birefringence and by decoration methods. They suggested that both these techniques could be used without the need for image magnification. Matthews and Plaskett [37,38] determined the conditions under which edge dislocations were invisible by observing optical birefringence images of prismatic dislocation loops in GGG.

Matthews and Plaskett [39] found that imperfect neodymium gallium garnet (NdGG) crystals were good for birefringence studies as they contained grain boundaries, long and large straight dislocations, and prismatic loops. They observed that the size of the image of a dislocation depended upon the distance from its neighbor. When it was surrounded by other dislocations, the resultant image of a dislocation appeared to fade out because of the compensation of its stress field by those produced by its neighbors. Therefore, in a crystal with low density of dislocations, low magnification can be used to resolve dislocations as the individual dislocation images are larger and brighter.

Haydar and Labusch [40] studied defect induced birefringence in Cu_2O crystals. They commented that the association of this method with optical scanning photoconductivity could give precise information about the electrically active structural defects. Reflection birefringence topography was used by Xu and Feng [41] to study dislocations and subboundaries in $Bi_{12}GeO_{20}$ (BGO) crystals. Transmission techniques could not be applied to BGO crystals because of its strong optical activity. They found that when a dislocation is located at a large angle relative to the surface normal, the dislocation images appear as lines. Some dislocation images were found to be larger than others. The reason could be that the strain patterns of close, parallel, neighboring dislocations overlap one another.

Gallium Phosphide (GaP) is a convenient material to test the application of the birefringence technique. It has large elastooptical coefficients and is transparent to visible light [28,42,43]. Hilgarth [42] observed dislocation images in GaP single crystals by means of birefringence, X-ray topography, electroluminescence, and electron beam induced current (EBIC). A good match was found between the X-ray topography and the birefringence methods. However, a comment was made that because of the high absorption coefficient for X-rays of GaP, exposure time necessary to make a high resolution topograph was extremely long. For samples of the usual thickness, overlapping of dislocations occurred, which made it impossible to resolve single dislocation images by the X-ray method.

Both GaP crystals and GaP on GaP epitaxial layers were investigated by Loschke and Paufler [43]. They were able to observe edge dislocations but did not succeed in imaging screw dislocations. In another paper [44], Paufler and Loschke made two important observations that certain types of dislocations only became visible under stress, and that screw dislocations are not visible in isotropic media.

Heterostructures and their resultant stress-induced birefringent images have been reported by a few authors [45-50]. Ahearn et al. [45] observed stress-induced birefringent images of InGaP and GaAsP on GaP in visible

light and InGaAs on GaAs in the infrared. The stress was produced due to the misfit of the lattice structures of the epilayer and the substrate. Bartels and Nijman [46] observed individual misfit dislocations of GaInAs epitaxial layers grown on GaAs substrates covered with a GaAlAs layer using X-ray topography. Booyens and Basson [47] measured the interface stress produced by a GaP/GaAlAs/GaAs and a GaP/GaAs heterostructures using infrared piezobirefringence. In a second paper, Booyens and Basson [48] discussed the use of infrared birefringence for characterizing dislocations from the knowledge of the sign of the strain in III-V compounds.

Booyens et al. [49] observed that the substrate dislocations can influence the growing epitaxial layers in two ways. First, threading dislocations are produced by the substrate dislocation which lengthens as the layer grows. Second, section of a dislocation inside the epitaxial layer might bow out into the interface to form a mismatch relieving misfit dislocation, if enough misfit stress was present and if a certain critical layer thickness was exceeded. For substrates with relatively thick epilayers, the epilayer itself can produce enough stress on the substrate to induce dislocations. Booyens et al. [50] studied the strain fields produced by SiO stripes evaporated on GaAs and GaP substrates using piezobirefringence. They showed that the stress near the edge of a film is many times larger than the

average intrinsic stress, and can have normal and shear components. The stresses induced in a thin film below the SiO stripe were substantial and could be a source of poor yield or failure.

1.3 Scope of the Present Work

The preceding section shows the enormity of the work which has been performed in the field of the use of piezobirefringence for dislocation characterization in crystalline semiconductor materials. However, these works lack the generalization that would allow it to be effectively used for defect characterization in semiconductor materials. The primary objective of the current work here is to develop a generalized theory for the simulation of the images of dislocations in semiconductor materials and to create an image data base for different kinds of dislocations. The simulated images will be dependent on the substrate orientation, the orientation of the dislocation line with respect to the principal crystal axes, the orientation of the Burger vector with respect to the dislocation line, and the polarization direction of the incident light. An image matching routine between the experimental image and the simulated images stored in the image data bank could then be used to characterize the observed defects.

CHAPTER 2

IMAGE SIMULATIONS

2.1 Introduction

This chapter illustrates the image simulation algorithms. Section 2.2 gives the background of the technique used. As a first step towards dislocation characterization in semiconductors, the simulation algorithm was applied to diametrically compressed discs of Si and GaAs. Section 2.3 deals with the development of the simulation algorithm for this case. Section 2.4 gives a brief theoretical background of the dislocations in crystals. The stress equations for a pure edge dislocation and a pure screw dislocation are described in Sections 2.4.1 and 2.4.2, respectively. Section 2.4.3 illustrates a general image simulation algorithm for the case of mixed dislocations. Section 2.5 describes the use of the algorithm to obtain the image intensity distribution for some special cases of interest.

2.2 Background

The technique utilized in this work involves the observation of the phase shift introduced between the two components of a plane polarized light beam while passing through a stressed sample. The sample is placed between the polarizer and the analyzer and illuminated by a monochromatic,

plane-polarized light. A laser is used as the light source in this work. A beam expander is used in the optical path before the polarizer if a larger beam diameter is needed. After the light passes through the analyzer, it is detected by a camera and displayed on a video monitor.

The algorithms developed in this chapter calculate the magnitude of the phase shift between the two light components while traversing through a stressed sample, and then obtain the intensity distribution from the knowledge of the phase shift. The stress can be either applied externally or generated internally by defects. If the sample is unstressed, the light after passing through the sample does not experience any relative phase change and is subsequently blocked out by the analyzer which is placed crossed to the polarizer. Thus a dark image is obtained. However, if the sample is stressed, there will be a phase shift introduced between the two light components while traversing through the sample and can be resolved along the analyzer axis. Thus a resultant intensity distribution can be obtained.

The aim of this chapter is to develop a general image simulation algorithm which can be applicable for a variety of dislocations present in the material. The general nature of the algorithm permits use of different crystal orientations, different orientations of the dislocation line with respect to the crystal principal axes, different orienta-

tions of the Burger vector with respect to the dislocation line, and different incident light polarization directions.

2.3 Semiconductor Discs under Diametrical Compression

In this section, image simulation is carried out for infrared transparent semiconductor discs under externally applied load in the form of diametrical compression. This is done to obtain a better understanding of the simulation algorithm as a first step towards obtaining simulation images for dislocations in semiconductors.

The disc under consideration is of radius R, thickness d, and under a diametrical compression load P. The loading axes system is defined in Fig.2.1. The loading axis x_2'' is chosen arbitrarily and does not necessarily coincide with any of the crystal principal axes. Axis x_1'' is perpendicular to axis x_2'' and lies on the sample surface and axis x_3'' is coming out from the plane of the paper. The stress at any point (x_1'', x_2'') for a disc under diametrical compression is given by [51]:

$$\sigma_{11}'' = -\frac{2P}{\pi d}\left[\frac{(R-x_2'')x_1''^2}{r_1^4} + \frac{(R+x_2'')x_1''^2}{r_2^4} - \frac{1}{2R}\right], \qquad (2.1)$$

$$\sigma_{22}'' = -\frac{2P}{\pi d}\left[\frac{(R-x_2'')^3}{r_1^4} + \frac{(R+x_2'')^3}{r_2^4} - \frac{1}{2R}\right], \qquad (2.2)$$

$$\sigma_{12}'' = \frac{2P}{\pi d}\left[\frac{(R-x_2'')^2 x_1''}{r_1^4} - \frac{(R+x_2'')^2 x_1''}{r_2^4}\right] \qquad (2.3)$$

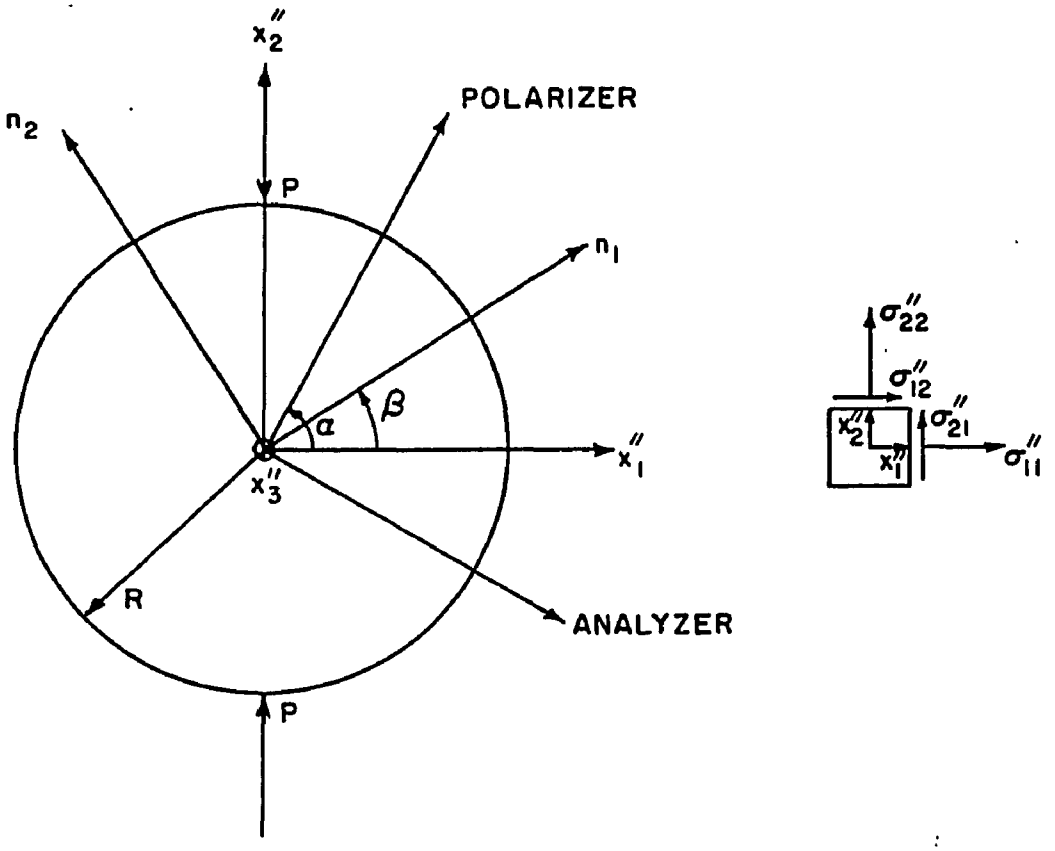

Fig.2.1 The sample geometry. Axis x_3'' is the outward normal from the plane of the paper.

where $r_1^2 = x_1''^2 + (R-x_2'')^2$ and $r_2^2 = x_1''^2 + (R+x_2'')^2$. Here σ_{ij}'' is the stress produced in direction x_i'' transmitted across a surface perpendicular to direction x_j''. The σ_{11}'' and σ_{22}'' components are the normal components of stress while σ_{12}'' is the shear component with $\sigma_{12}'' = \sigma_{21}''$ because there is no resultant torque in the system. In order to compute the stress components σ_{ij}'', the sample is divided into small squares and the stresses are calculated at the center of each of these squares. The semiconductor materials of primary interest in this work are Si and GaAs both of which belong to the cubic class of crystal symmetry. The indicatrix of a cubic crystal under unstressed condition is spherical with no preferred optic axis. However, under stress the indicatrix changes to an ellipsoid of revolution and can be given by a quadric surface [52]

$$\sum_{k,l} B_{kl}'' x_k'' x_l'' = 1 \quad (k,l=1,2,3) , \tag{2.4}$$

where k and l are summation indices and B_{kl}'' are the elements of the dielectric impermeability matrix defined by $B_{kl}'' = B_{kl}^{(0)} + \Delta B_{kl}''$, where $B_{kl}^{(0)}$ are the elements of the dielectric impermeability tensor. For an isotropic material, the only non-zero values of $B_{kl}^{(0)}$ are given by $B_{11}^{(0)} = B_{22}^{(0)} = B_{33}^{(0)} = B_0$ where $B_0 = 1/n_0^2$ and where n_0 is the isotropic value of the refractive index. Here, $\Delta B_{kl}''$ are the changes in $B_{kl}^{(0)}$ due to the stress components. When the light is incident along $-x_3''$ direction, the intersection ellipse as obtained from Eqn.(2.4) is given by

$$(B_0+\Delta B''_{11})x''^2_1 + (B_0+\Delta B''_{22})x''^2_2 + \Delta B''_{12}x''_1x''_2 + \Delta B''_{21}x''_2x''_1 = 1 \quad .(2.5)$$

The diagonalization of Eqn.(2.5) would give the major and the minor axes of the ellipse formed by the intersection of the incident light direction with the indicatrix. The result of the diagonalization yields B_1 and B_2, the dielectric impermeabilities along the minor and the major axes of the index ellipse, respectively. They are given as

$$B_1 = B_0 + (\Delta B''_{11}+\Delta B''_{22})/2 + (1/2)\sqrt{[(\Delta B''_{11}-\Delta B''_{22})^2+4\Delta B''_{12}\Delta B''_{21}]} \quad , \qquad (2.6)$$

and

$$B_2 = B_0 + (\Delta B''_{11}+\Delta B''_{22})/2 - (1/2)\sqrt{[(\Delta B''_{11}-\Delta B''_{22})^2+4\Delta B''_{12}\Delta B''_{21}]} \quad , \qquad (2.7)$$

In the above equations, $\Delta B''_{12} = \Delta B''_{21}$ for semiconductors with cubic symmetry. The corresponding refractive indices are given by $n_1 = 1/\sqrt{B_1}$ and $n_2 = 1/\sqrt{B_2}$. Due to these local differences in the refractive indices, the components of a plane polarized light beam traversing the sample will show a phase shift. When the light emerging from the sample is viewed through an analyzer, the resultant image will show a pattern characteristic of this phase shift.

The piezooptic coefficients π_{ijk} are used to compute the changes in the dielectric impermeability elements $\Delta B''_k$. The piezooptic coefficients are conventionally defined along the crystal principal axes. Therefore, the computation is

carried out in two steps. First, the stress components σ''_{ij} obtained from Eqns.(2.1-2.3) are transformed to the crystal principal axes. Then, the changes in the dielectric impermeability elements are obtained in the crystal principal axes system. These are then converted back to the loading axes system.

The equations for transforming the stress components from the loading axes system (x''_1,x''_2,x''_3) to the crystal principal axes system (x'_1,x'_2,x'_3) are given by [52] as

$$\sigma'_{kl} = \sum_{i,j} a'_{ki}a'_{lj}\sigma''_{ij} \qquad (i,j=1,2,3) \tag{2.8}$$

where i and j are summation indices and a'_{ki} is the direction cosine between the crystal principal axis x'_k and the loading axis x''_i. The calculations of the direction cosines for {100} and {111} oriented samples under arbitrary loading direction are discussed in Appendices A and B, respectively.

In terms of the piezooptic coefficients π_{ijkl}, the changes in the dielectric impermeability $\Delta B'_{ij}$ in the crystal principal axes system due to the loading are given by [52] as

$$\Delta B'_{ij} = \sum_{k,l} \pi_{ijkl}\sigma'_{kl} \qquad (k,l=1,2,3) \tag{2.9}$$

where k and l are summation indices and σ'_{kl} are given by Eqn.(2.8). The piezooptic coefficients π_{ijkl} form a fourth-

rank tensor having in general 81 terms. A reduced notation as suggested by Nye [52] is often used to express the fourth-rank tensor coefficients as given in Table 2.1.

Table 2.1

Conversion technique from tensor to reduced notation.

tensor notation	11	22	33	23,32	31,13	12,21
reduced notation	1	2	3	4	5	6

The dielectric impermeability elements ΔB_{ij} evaluated by Eqn.(2.9) are defined along the crystal principal axes. The last step of the procedure is to transform these elements back to the loading axes system, which is given by the transformation [52]

$$\Delta B'_{kl} = \sum_{i,j} a_{ik} a_{jl} \Delta B_{ij} \qquad (i,j=1,2,3) \qquad (2.10)$$

where i and j are summation indices and ΔB_{ij} are defined by Eqn.(2.9). The impermeability elements $\Delta B'_{kl}$ which are found from Eqn.(2.10) are used in Eqns.(2.6) and (2.7) to obtain the major and the minor axes of the intersection ellipse formed by the incident light with the indicatrix surface. Once B_1 and B_2 are known, the corresponding refractive indi-

ces can be found easily from $n_1 = 1/\sqrt{B_1}$ and $n_2 = 1/\sqrt{B_2}$, where n_1 and n_2 are the refractive indices along the minor and the major axes of the index ellipse, respectively. After the refractive indices are known, the intensity calculation can be carried out as given below.

A light wave after passing through the polarizer and incident upon the sample has the form $A\cos(\omega t-\phi+2\pi x_3''/\lambda)$ where λ is the wavelength, ω is the angular frequency and ϕ is an arbitrary phase angle. The component amplitude along the direction of the minor axis of the index ellipse is given by $A\cos(\alpha-\beta)$. As shown in Fig.2.1, α and β are respectively the angles subtended by the incident light polarization direction and the minor axis of the index ellipse with respect to the axis x_1''. The angle β is given by [51]

$$\beta = (1/2)\tan^{-1}[(\Delta B_{12}''+\Delta B_{21}'')/(\Delta B_{11}''-\Delta B_{22}'')] . \qquad (2.11)$$

In the above equation, $\Delta B_{12}'' = \Delta B_{21}''$ for semiconductors with cubic symmetry. The component amplitude along the major axis direction of the index ellipse is given by $A\sin(\alpha-\beta)$. The light intensity transmitted through the analyzer will be polarized along the analyzer direction. The components along the major and the minor axes directions are further resolved along the polarizer and the analyzer directions. Let the component amplitudes $A\cos(\alpha-\beta)$ and $A\sin(\alpha-\beta)$ be denoted by A_1 and A_2, respectively. Thus, for a ray travel-

ling along the minor axis, the component amplitudes along the polarizer and the analyzer directions are given by $A_1\cos(\alpha-\beta)$ and $A_1\sin(\alpha-\beta)$, respectively. Similarly, for the ray travelling along the major axis, the component amplitudes along the polarizer and the analyzer directions are given by $A_2\sin(\alpha-\beta)$ and $-A_2\cos(\alpha-\beta)$, respectively. The net light amplitude L coming out of the analyzer is, hence, written as

$$L = A\sin(\alpha-\beta)\cos(\alpha-\beta)\cos(\omega t-\phi+2\pi d/\lambda_1) - A\sin(\alpha-\beta)\cos(\alpha-\beta)\cos(\omega t-\phi+2\pi d/\lambda_2)$$

where $\lambda_1 = \lambda/n_1$ and $\lambda_2 = \lambda/n_2$ are the wavelengths along the minor and the major axes respectively. The above expression can be written as

$$L = (A/2)\sin 2(\alpha-\beta)[\cos(\omega t-\phi+2\pi d/\lambda_1) - \cos(\omega t-\phi+2\pi d/\lambda_2)].$$

Squaring and taking the time average to get the net resultant intensity I coming out of the analyzer, one finally obtains

$$I = (A^2/2)\sin^2 2(\alpha-\beta)\sin^2[\pi d(1/\lambda_1 - 1/\lambda_2)] . \qquad (2.12)$$

In general, for each point on the wafer, the stresses and hence, the angle β and the values for λ_1 and λ_2 will be different. Thus, the resultant intensity image will show dark and bright regions resulting in a fringe pattern. The computer program developed in this work uses the above

developed analytical approach to compute the intensity of the light transmitted through the diametrically stressed sample. The size of the squares for the stress calculation was selected carefully so that the intensity did not show any abrupt discontinuity. For example, in order to simulate the images for a diametrically compressed Si disc of 1.746 cm in diameter, the total area was divided into approximately 60,000 squares of uniform size with each side of the square being approximately equal to 0.063 mm. In the computer program, quadruple precision arithmetic was necessary to maintain numerical accuracy.

Silicon and gallium arsenide, the two main semiconductors of interest in this work belong to the cubic class of crystal symmetry, silicon is a member of the m3m group while gallium arsenide is a member of $\bar{4}3m$ group. All crystals having cubic symmetry have only three independent, non-equal and non-zero piezooptic coefficients out of a possible total of 81. In reduced notation, these three non-zero coefficients are denoted by π_{11}, π_{12}, and π_{44} [52]. They can be expressed as follows:

$$1)\ \pi_{11} = \pi_{22} = \pi_{33},$$

or explicitly as $\pi_{1111} = \pi_{2222} = \pi_{3333}$; (2.13)

$$2)\ \pi_{44} = \pi_{55} = \pi_{66},$$

or explicitly as $\pi_{1212} = \pi_{1221} = \pi_{2121} = \pi_{2112} = \pi_{2323} = \pi_{2332} = \pi_{3232} = \pi_{3223} = \pi_{3131} = \pi_{3113} = \pi_{1313} = \pi_{1331}$; (2.14)

and 3) $\pi_{12} = \pi_{23} = \pi_{31} = \pi_{13} = \pi_{32} = \pi_{21}$,

or explicitly as $\pi_{1122} = \pi_{2233} = \pi_{3311} =$

$$\pi_{1133} = \pi_{3322} = \pi_{2211}. \qquad (2.15)$$

For Silicon, the values used in Eqn.(2.9) in this program were taken from Giardini [14] and are shown in Table 2.2. These values were measured at a wavelength of 1.11 μm by Giardini [14] which is close to the wavelength of 1.15 μm used in this work. For Gallium Arsenide, to the best of our knowledge, the values for the piezooptic coefficients are not available in the open literature. However, the paper by Booyens and Basson [47] has reported the elastooptic coefficients and the stiffness values of Gallium Arsenide at a wavelength of 1.15 μm. The procedure of obtaining the piezooptic coefficients from the elastooptic coefficients and the stiffness values is given in Appendix C and the calculated values are shown in Table 2.3.

2.4 Dislocations in Crystals

In a perfect crystal, the atoms form a regular pattern. When the regular pattern breaks down and some atoms are not properly surrounded by neighbors, imperfections result. Examples of imperfections are vacancies, interstitials, impurity atoms, dislocations, grain boundaries, and stacking faults. The dislocation in a crystal results when some planes of the atoms slip with respect to other planes to

Table 2.2

The piezooptic coefficients for Si used in computation (after [14]).

Coefficient	Value (cm^2/dyne)
π_{1111}	-9.0×10^{-14}
π_{1122}	6.0×10^{-14}
π_{1212}	-5.0×10^{-14}

Table 2.3

The piezooptic coefficients of GaAs as derived from data of Booyens and Basson [47].

Coefficient	Value (cm^2/dyne)
π_{1111}	-9.115×10^{-14}
π_{1122}	-5.269×10^{-14}
π_{1212}	-6.061×10^{-14}

break the periodicity of the crystal. Figure 2.2 shows a simple edge dislocation. Here, an unit slip has occurred over a part of the slip plane ABCD. The boundary of the slipped area within the crystal is a dislocation. In the figure, the line AD is the boundary of the slipped area ABCD within the crystal, and it is known as the dislocation line. For an edge dislocation, the slip vector is at right angles to the dislocation line.

Figure 2.3 shows a simple screw dislocation. Here again the slip has occurred along the plane ABCD and the line AD forming the boundary of the slipped area within the crystal is the dislocation line. For a screw dislocation, the slip vector is parallel to the dislocation line. Figure 2.4 shows a screw dislocation parallel to a cube edge in a simple cubic crystal. The unit cells are shown as distorted cubes. Figure 2.5 depicts two cases with one containing a dislocation and the other without a dislocation. Figure 2.5b) shows a perfect arrangement of the atoms in the lattice, where the lattice points are related by the translation vector $mt_1 + nt_2$, where m and n can only have integer values and t_1 and t_2 are the translation vectors in the two-dimensional lattice. The definition of the Burger vector $\overline{b}$ depends on the sense of the dislocation line $\overline{\xi}$, which can be arbitrarily chosen along the dislocation line. In Fig.2.5, the positive sense of the dislocation $\overline{\xi}$ is taken to be into the paper. In order to define the Burger vector $\overline{b}$, first a

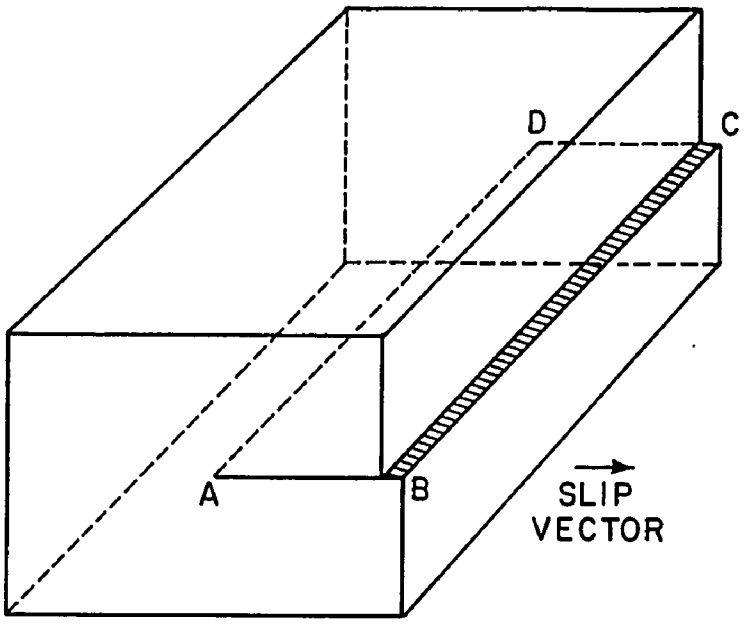

Fig.2.2 A simple edge dislocation. ABCD is the dislocation slip plane, AD is the dislocation line perpendicular to the slip vector (after [4]).

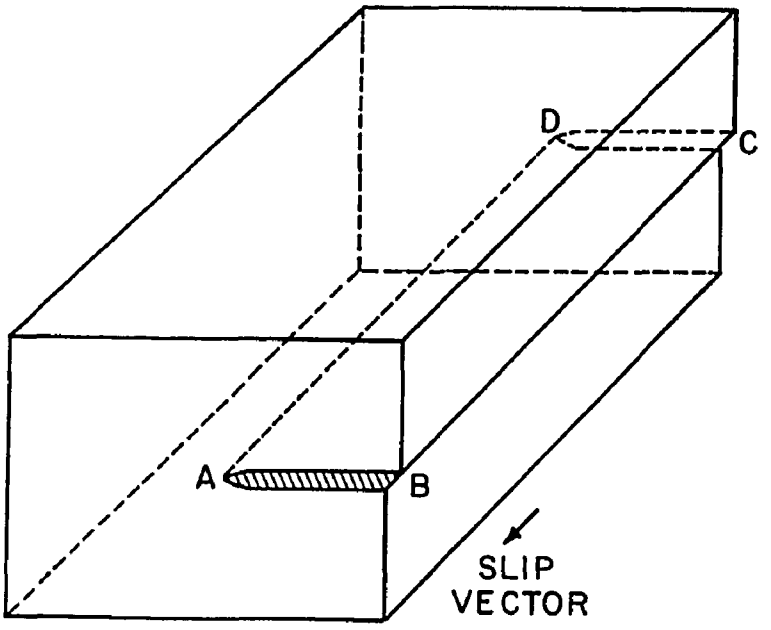

Fig.2.3 A simple screw dislocation. ABCD is the dislocation slip plane, AD is the dislocation line parallel to the slip vector (after [4]).

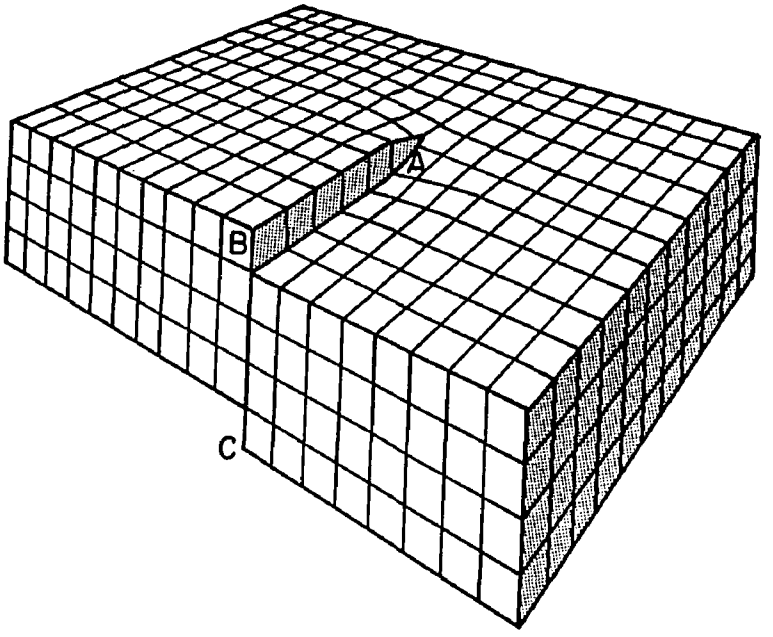

Fig.2.4 Another view of a screw dislocation. The dislocation line AD (of which only the end A is visible) is parallel to the line BC and is parallel to the slip vector. The crystal can be viewed as a single atomic plane in the form of a helicoid, or a spiral ramp (after [4]).

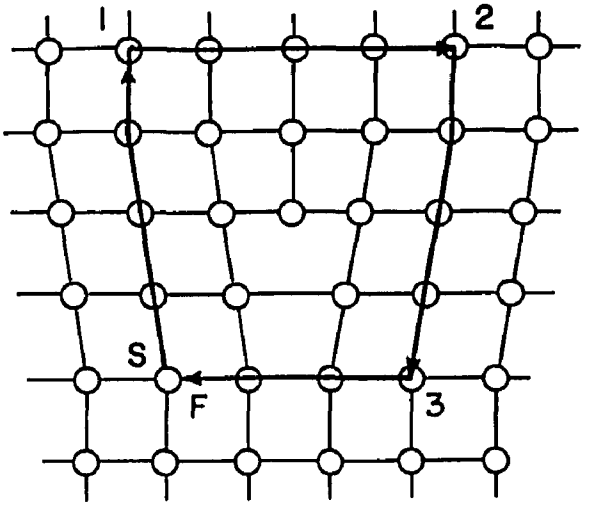

a)

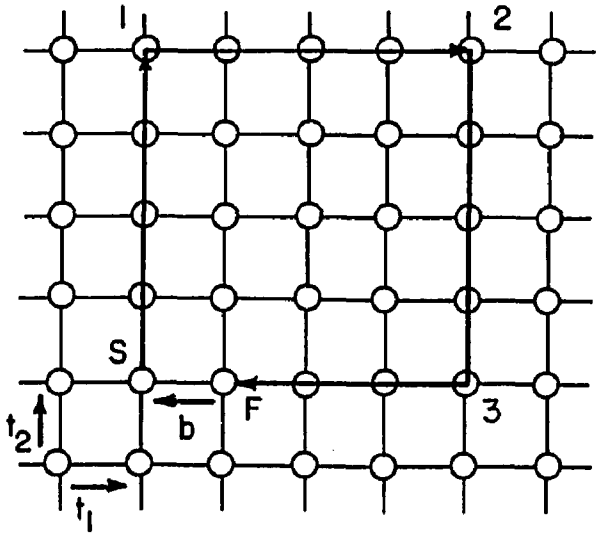

b)

Fig.2.5 FS/RH Burger's circuit in a) an imperfect crystal and b) a perfect crystal. $\bar{\xi}$ points into the paper (after [10]).

closed clockwise path called Burger's circuit depicted by S-1-2-3-F in Fig.2.5a) is formed. This path encloses the dislocation. Then the same circuit is drawn in the perfect crystal lattice as shown in Fig.2.5b). The vector required to close the latter circuit, drawn between F and S in Fig.2.5b), is defined as the Burger vector $\bar{b}$. Since the sense of the circuit is that of a right-handed screw RH, this convention for $\bar{b}$ is called the FS/RH convention.

One important point to note is that reversing the sense of the dislocation line causes $\bar{b}$ to reverse its direction. Based on this discussion, a dislocation can now be defined more formally as being characterized by a dislocation line or sense $\bar{\xi}$ and a Burger vector $\bar{b}$. For an edge dislocation, $\bar{b}.\bar{\xi} = 0$; for a right-handed screw dislocation, $\bar{b}.\bar{\xi} = b$; and for a left-handed screw dislocation, $\bar{b}.\bar{\xi} = -b$. The approach described here follows closely the procedure suggested by Hirth and Lothe [10].

In this section, the stress fields associated with dislocations are discussed and the resulting interference fringe patterns simulated using algorithm similar to the one developed in Section 2.3. Section 2.4.1 deals with the stress fields of a pure edge dislocation, and Section 2.4.2 deals with the same for a pure screw dislocation. Section 2.4.3 illustrates the procedure of obtaining the stress fields of a mixed dislocation, which is neither a pure edge

dislocation nor a pure screw dislocation. An algorithm is developed for obtaining the interference fringe patterns for a mixed dislocation. The algorithm can be used to determine the images caused by any arbitrary dislocation, taking into account any arbitrary orientation of the Burger vector with respect to the dislocation line, any arbitrary orientation of the dislocation line with respect to the principal crystal axes, and any arbitrary polarization angle of the light incident perpendicular to the sample.

2.4.1 Edge Dislocations

A stationary edge dislocation is shown in Fig.2.6 where x_1, x_2, and x_3 are the coordinate system chosen, $\bar{\xi}$ is the sense of the dislocation and $\bar{b}$ is the Burger vector. The line of the dislocation considered here is chosen to be along the x_3 direction, and its Burger vector is chosen to be along the x_1 direction. The stress fields associated with this dislocation are given by [10] as

$$\sigma_{11} = -\frac{\mu b}{2\pi(1-\nu)} \cdot \frac{x_2(3x_1^2+x_2^2)}{(x_1^2+x_2^2)^2} , \tag{2.16}$$

$$\sigma_{22} = \frac{\mu b}{2\pi(1-\nu)} \cdot \frac{x_2(x_1^2-x_2^2)}{(x_1^2+x_2^2)^2} , \tag{2.17}$$

$$\sigma_{12} = \sigma_{21} = \frac{\mu b}{2\pi(1-\nu)} \cdot \frac{x_1(x_1^2-x_2^2)}{(x_1^2+x_2^2)^2} , \tag{2.18}$$

$$\sigma_{33} = \nu(\sigma_{11}+\sigma_{22}) , \tag{2.19}$$

and

$$\sigma_{13} = \sigma_{31} = \sigma_{23} = \sigma_{32} = 0 . \tag{2.20}$$

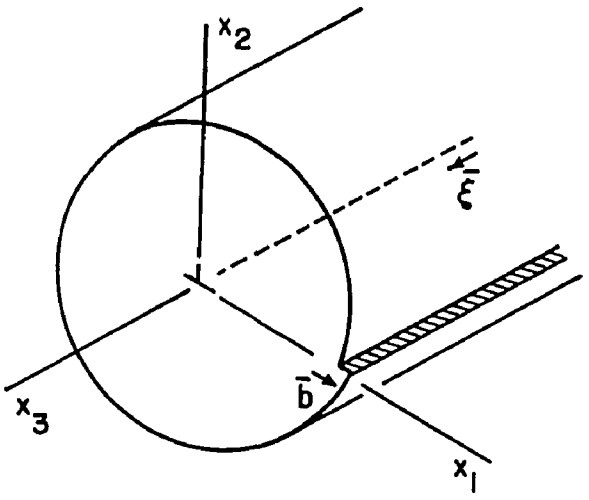

Fig.2.6 An edge dislocation with the Burger vector $\bar{b}$ perpendicular to the sense of the dislocation $\bar{\xi}$. The coordinate system (x_1, x_2, x_3) is used to represent the stresses.

In the above equations, μ is the shear modulus, b is the magnitude of the Burger vector, and ν is Poisson's ratio defined as the ratio of transverse contraction to longitudinal elongation in simple tension. Next, the stress fields associated with a screw dislocation are considered.

2.4.2 Screw Dislocations

A stationary screw dislocation with sense $\bar{\xi}$ and Burger vector $\bar{b}$ is shown in Fig.2.7. The sense of the dislocation and the Burger vector are chosen along the x_3 direction. The stress fields associated with this dislocation are given by [10] as

$$\sigma_{13} = \sigma_{31} = -\frac{\mu b}{2\pi}\cdot\frac{x_2}{x_1^2+x_2^2}\ , \tag{2.21}$$

$$\sigma_{23} = \sigma_{32} = \frac{\mu b}{2\pi}\cdot\frac{x_1}{x_1^2+x_2^2}\ , \tag{2.22}$$

$$\sigma_{11} = \sigma_{22} = \sigma_{33} = \sigma_{12} = \sigma_{21} = 0\ , \tag{2.23}$$

where μ is the shear modulus, and b is the magnitude of the Burger vector. In the next section, the stress field associated with a mixed dislocation is considered, which is a combination of the stress fields associated with a pure edge dislocation and a pure screw dislocation. The section also develops the general algorithm for the computation of the image intensity distribution associated with a mixed dislocation.

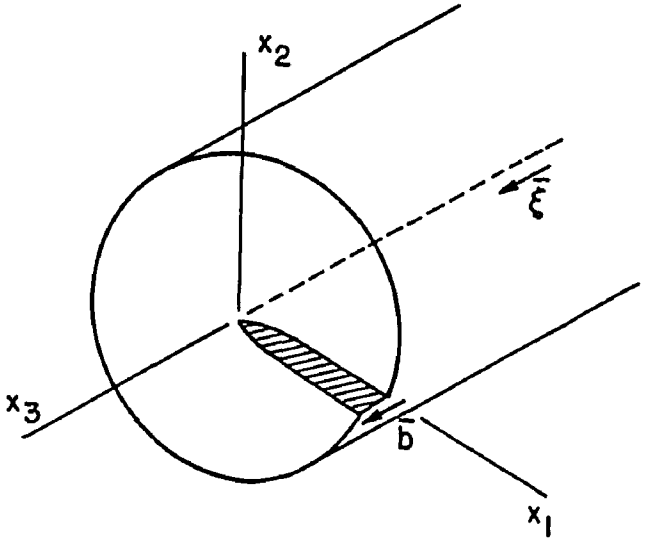

Fig.2.7 A screw dislocation with the Burger vector parallel to the dislocation line. The coordinate system (x_1, x_2, x_3) is used to represent the stresses.

2.4.3 Mixed Dislocations

A mixed dislocation is one which is neither a pure screw dislocation nor a pure edge dislocation. Its Burger vector is, hence, neither parallel nor perpendicular to the dislocation line. However, it can be resolved into two components - one corresponding to the pure edge dislocation $\bar{b}_e$, and the other corresponding to the pure screw dislocation $\bar{b}_s$ as shown in Fig.2.8 [53]. Here, the Burger vector for a mixed dislocation makes an arbitrary angle κ with the sense of the dislocation. From Fig.2.8, it can be seen that $\bar{b}_s = \bar{b} \cos \kappa$, and $\bar{b}_e = \bar{b} \sin \kappa$. As before, (x_1, x_2, x_3) denotes the stress axes system, and (x_1', x_2', x_3') denotes the crystal principal axes system. The sample axes system is denoted by (x_1'', x_2'', x_3''). These are linear rectilinear coordinate systems. The sense of the mixed dislocation defines the x_3 axis in the stress axes system. The Burger vector lies on the x_1x_3 plane and axis x_1 is at 90° with respect to axis x_3. This defines the direction of axis x_1. Axis x_2 is mutually perpendicular to both axes x_1 and x_3. Taking into consideration the stress fields associated with a pure edge and a pure screw dislocation as given in Eqns.(2.16-2.20) and Eqns.(2.21-2.23), the resulting stress fields for a mixed dislocation are given by:

$$\sigma_{11} = -\frac{\mu b_e}{2\pi(1-\nu)} \cdot \frac{x_2(3x_1^2+x_2^2)}{(x_1^2+x_2^2)^2}, \qquad (2.24)$$

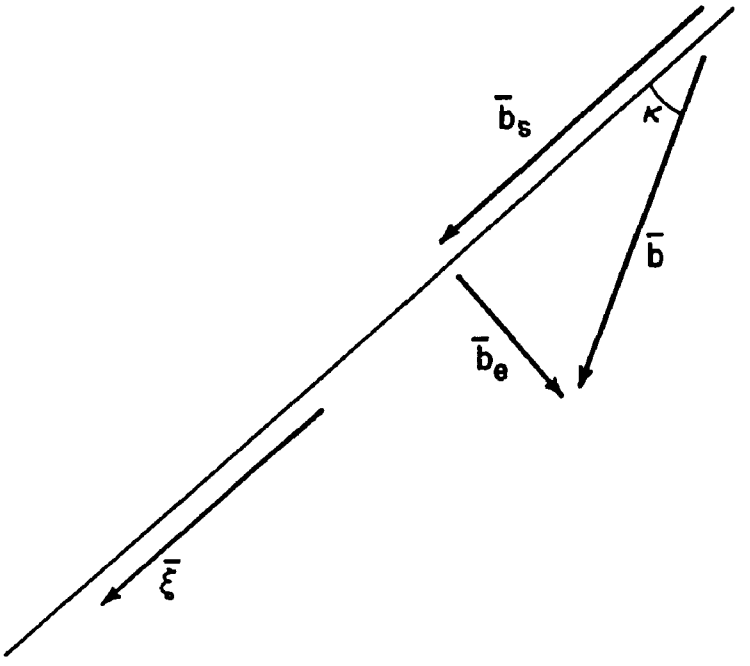

Fig.2.8 A mixed dislocation with its Burger vector inclined at an angle κ to the dislocation line.

$$\sigma_{12} = \sigma_{21} = \frac{\mu b_e}{2\pi(1-\nu)} \cdot \frac{x_1(x_1^2-x_2^2)}{(x_1^2+x_2^2)^2} , \qquad (2.25)$$

$$\sigma_{13} = \sigma_{31} = -\frac{\mu b_s}{2\pi} \cdot \frac{x_2}{x_1^2+x_2^2} , \qquad (2.26)$$

$$\sigma_{22} = \frac{\mu b_e}{2\pi(1-\nu)} \cdot \frac{x_2(x_1^2-x_2^2)}{(x_1^2+x_2^2)^2} , \qquad (2.27)$$

$$\sigma_{23} = \sigma_{32} = \frac{\mu b_s}{2\pi} \cdot \frac{x_1}{x_1^2+x_2^2} , \qquad (2.28)$$

$$\sigma_{33} = \nu(\sigma_{11}+\sigma_{22}) \qquad (2.29)$$

where μ is the shear modulus, and ν is Poisson's ratio.

Now the changes in the dielectric impermeabilities caused by these stresses need to be computed. This computation uses the piezoeptic coefficients π_{ijkl}, which are defined along the crystal principal axes. Therefore the stresses given by Eqns.(2.24-2.29) need to be transformed along the crystal axes system, for which one needs to know the direction cosines between the crystal principal axes (x_1',x_2',x_3') and the stress axes (x_1,x_2,x_3). This transformation is carried out in two steps. First, the stresses are converted from the stress axes system (x_1,x_2,x_3) to the sample axes system (x_1'',x_2'',x_3''), and then from the sample axes system to the crystal axes system (x_1',x_2',x_3').

The sample axes system is shown in Fig.2.9. The stress axes system (x_1,x_2,x_3) need not coincide with the sample axes system (x_1'',x_2'',x_3''). In other words, the disloca-

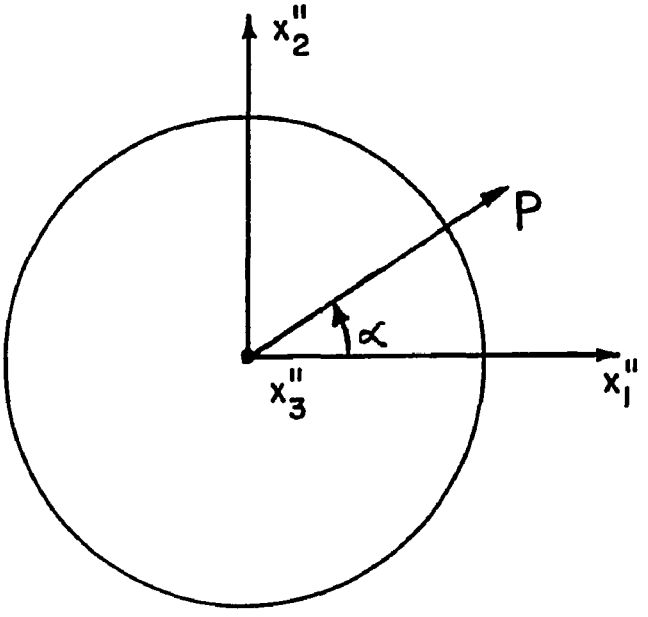

Fig.2.9 The sample coordinate system (x_1'', x_2'', x_3''). Axis x_3'' comes out from the plane of the paper.

tion line can lie at any arbitrary angle within the sample and the Burger vector can be at any arbitrary angle with the dislocation sense. Let the angles between the axis x_1'' and axes x_1, x_2, and x_3 be ζ_1, ζ_2, ζ_3 respectively, between the axis x_2'' and axes x_1, x_2, and x_3 be η_1, η_2, and η_3 respectively and between the axis x_3'' and axes x_1, x_2, and x_3 be χ_1, χ_2, and χ_3 respectively. Thus, any arbitrary orientation of the dislocation line can in general be treated. The direction cosines can now be given by

$$
\begin{aligned}
a_{11} &= \cos x_1''\hat{}x_1 = \cos \zeta_1 , \\
a_{12} &= \cos x_1''\hat{}x_2 = \cos \zeta_2 , \\
a_{13} &= \cos x_1''\hat{}x_3 = \cos \zeta_3 , \\
a_{21} &= \cos x_2''\hat{}x_1 = \cos \eta_1 , \\
a_{22} &= \cos x_2''\hat{}x_2 = \cos \eta_2 , \\
a_{23} &= \cos x_2''\hat{}x_3 = \cos \eta_3 , \\
a_{31} &= \cos x_3''\hat{}x_1 = \cos \chi_1 , \\
a_{32} &= \cos x_3''\hat{}x_2 = \cos \chi_2 , \\
\text{and} \quad a_{33} &= \cos x_3''\hat{}x_3 = \cos \chi_3 . \qquad (2.30)
\end{aligned}
$$

For the direction cosines

$$\sum_j a_{ij}^2 = 1 \quad (j=1,2,3) . \qquad (2.31)$$

Therefore, out of each set of three angles, if two of them are known, the value for the third angle is fixed and can be obtained from Eqn.(2.31).

Now the stresses given by Eqns.(2.24-2.29) can be transformed to the sample axes using the direction cosines given by Eqns.(2.30). The transformation equation is given by [52] as

$$\sigma''_{ij} = \sum_{k,l} a_{ik} a_{jl} \sigma_{kl} \quad (k,l=1,2,3) \ . \tag{2.32}$$

The double-primed notation such as σ''_{ij} is used here for quantities expressed in the sample axes system (x''_1, x''_2, x''_3). Depending on the specific situation, all the nine terms might be present in Eqn.(2.32). These stresses σ''_{ij} now will be transformed to the crystal principal axes system. In general, any arbitrary orientation of the sample can be treated. Let us assume that the crystal axis x'_1 makes angles of K_1, L_1, and M_1 with respect to the sample axes x''_1, x''_2, and x''_3 respectively, axis x'_2 makes angles of K_2, L_2, and M_2 with respect to the axes x''_1, x''_2, and x''_3 respectively, and axis x'_3 makes angles of K_3, L_3, and M_3 with respect to axes x''_1, x''_2, and x''_3 respectively. Thus the direction cosines between the crystal axes and the sample axes can be given by

$$\begin{aligned} &a'_{11} = \cos K_1, \quad a'_{12} = \cos L_1, \quad a'_{13} = \cos M_1, \\ &a'_{21} = \cos K_2, \quad a'_{22} = \cos L_2, \quad a'_{23} = \cos M_2, \\ \text{and} \quad &a'_{31} = \cos K_3, \quad a'_{32} = \cos L_3, \quad a'_{33} = \cos M_3. \end{aligned} \tag{2.33}$$

Therefore, in principle, any arbitrary orientation of the sample can be analyzed with this algorithm though for certain cases the calculation of the angles may be tedious. As

the crystal orientations {100} and {111} are of primary interest to the device fabrication industry, specifics of these two cases are given special attention in this work.

First, we take the case for a {100} oriented sample. It is assumed that the crystal axis x_1' is coming out of the plane of the paper and is coincident with the sample axis x_3'', and the crystal axis x_2' makes an angle ϕ with the sample axis x_1'' as shown in Fig.2.10. Thus, the direction cosines which are needed to convert the stresses from the sample axes system to the crystal principal axes system for a {100} oriented sample are given by

$$
\begin{aligned}
a'_{11} &= \cos x_1' \hat{} x_1'' = \cos K_1 = \cos 90^\circ = 0 , \\
a'_{12} &= \cos x_1' \hat{} x_2'' = \cos L_1 = \cos 90^\circ = 0 , \\
a'_{13} &= \cos x_1' \hat{} x_3'' = \cos M_1 = \cos 0^\circ = 1 , \\
a'_{21} &= \cos x_2' \hat{} x_1'' = \cos K_2 = \cos \phi , \\
a'_{22} &= \cos x_2' \hat{} x_2'' = \cos L_2 = \cos(90^\circ - \phi) , \\
a'_{23} &= \cos x_2' \hat{} x_3'' = \cos M_2 = \cos 90^\circ = 0 , \\
a'_{31} &= \cos x_3' \hat{} x_1'' = \cos K_3 = \cos(90^\circ + \phi) , \\
a'_{32} &= \cos x_3' \hat{} x_2'' = \cos L_3 = \cos \phi , \\
\text{and} \quad a'_{33} &= \cos x_3' \hat{} x_3'' = \cos M_3 = \cos 90^\circ = 0 . \qquad (2.34)
\end{aligned}
$$

The case for a {111} oriented sample is somewhat more complicated and is considered in detail in Appendix B. The resulting direction cosines needed to convert the stresses from the sample axes system to the crystal principal axes system for a {111} oriented sample are given by Eqns.(B.9) in the appendix and are rewritten here for convenience.

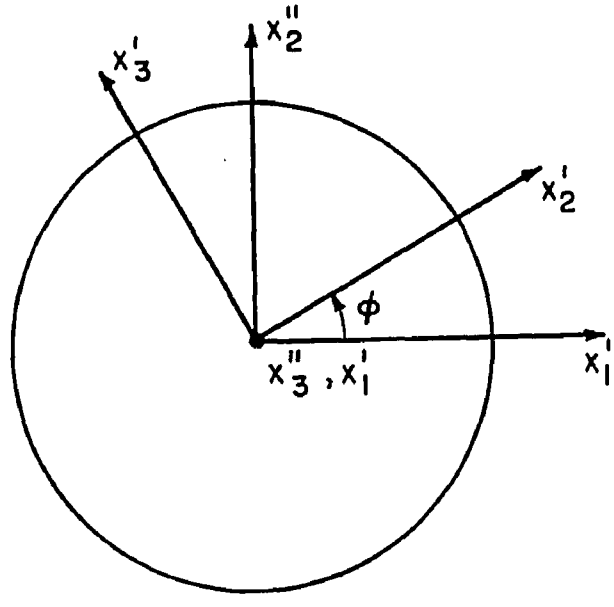

Fig.2.10 The relation between the sample axes system (x_1'', x_2'', x_3'') and the crystal principal axes system (x_1', x_2', x_3') for a {100} oriented sample.

$$a'_{11} = (2/\sqrt{6})\cos(90^\circ+\gamma) \ ,$$

$$a'_{12} = (2/\sqrt{6})\cos\gamma \ ,$$

$$a'_{13} = 1/\sqrt{3} \ ,$$

$$a'_{21} = -(1/\sqrt{2})\cos\gamma - (1/\sqrt{6})\cos(90^\circ+\gamma) \ ,$$

$$a'_{22} = -(1/\sqrt{2})\cos(90^\circ-\gamma) - (1/\sqrt{6})\cos\gamma \ ,$$

$$a'_{23} = 1/\sqrt{3} \ ,$$

$$a'_{31} = (1/\sqrt{2})\cos\gamma - (1/\sqrt{6})\cos(90^\circ+\gamma) \ ,$$

$$a'_{32} = (1/\sqrt{2})\cos(90^\circ-\gamma) - (1/\sqrt{6})\cos\gamma \ ,$$

$$a'_{33} = 1/\sqrt{3} \ , \qquad (2.35)$$

where γ is the angle between axes x''_2 and x^g_2 as shown in Fig.B.3a) on page 125.

The stress components given in Eqn.(2.32) can be converted from the sample axes system (x''_1,x''_2,x''_3) to the crystal axes system (x'_1,x'_2,x'_3) through the following transformation [52]:

$$\sigma'_{k1} = \sum_{i,j} a'_{ki}a'_{1j}\sigma''_{ij} \quad (i,j=1,2,3) \ . \qquad (2.36)$$

The single-primed notation such as σ'_{k1} is used here for quantities expressed in the crystal axes system (x'_1,x'_2,x'_3). The single exception to this notation is the use of π_{ijk1} for the piezooptic coefficients which are by convention defined along the crystal axes system. The values for the direction cosines used in Eqn.(2.36) can be taken either from Eqns.(2.34) or (2.35) depending on the specific situation, i.e., whether the sample is {100} oriented or {111}

oriented, respectively. The changes in the dielectric impermeability in the crystal axes system can now be computed using the following equation [52]:

$$\Delta B'_{ij} = \sum_{k,l} \pi_{ijkl}\sigma'_{kl} \quad (k,l=1,2,3) \tag{2.37}$$

where σ'_{kl} are given by Eqn.(2.36). To compute the resulting interference fringe patterns, one needs to convert these changes in the dielectric impermeabilities back to the sample axes system given by the following conversion equation [52]:

$$\Delta B''_{kl} = \sum_{i,j} a'_{ik}a'_{jl}\Delta B'_{ij} \quad (i,j=1,2,3) \tag{2.38}$$

where $\Delta B''_{kl}$ are now defined along the sample axes system. The equation of a quadric surface is given by [52]:

$$\sum_{k,l} B''_{kl}x''_k x''_l = 1 \quad (k,l=1,2,3)\ , \tag{2.39}$$

where $B''_{kl} = B''^{0}_{k} + \Delta B''_{kl}$. $\Delta B''_{kl}$ are given by Eqn.(2.38), and B''^{0}_{k} are the isotropic value of the dielectric impermeability. The only non-zero values of B''^{0}_{k} are given by $B''^{0}_{1} = B''^{0}_{2} = B''^{0}_{3} = B_0 = 1/n_0^2$, where n_0 is the isotropic value of the refractive index. The diagonalization of the indicatrix can be carried out upon fixing the direction of the incident light. To simplify the problem, it is assumed that the light falls along the sample - x''_3 direction, i.e., the sample is held perpendicular to the incident light. Note that

this does not in any way restrict the orientation of the dislocation line within the crystal. For this case, the intersection of the plane perpendicular to the ray direction is obtained by setting $x_3'' = 0$ and Eqn.(2.39) simplifies to give the cross-section of the indicatrix perpendicular to the ray direction as:

$$(B_0+\Delta B_{11}'')x_1''^2 + (B_0+\Delta B_{22}'')x_2''^2 + \Delta B_{12}''x_1''x_2'' + \Delta B_{21}''x_2''x_1'' = 1. \tag{2.40}$$

Diagonalization of the matrix yields the characteristic equation. The two roots are given by:

$$B_1 = B_0 + (\Delta B_{11}''+\Delta B_{22}'')/2 + (1/2)\sqrt{[(\Delta B_{11}''-\Delta B_{22}'')^2+4\Delta B_{12}''\Delta B_{21}'']} \tag{2.41}$$

and

$$B_2 = B_0 + (\Delta B_{11}''+\Delta B_{22}'')/2 - (1/2)\sqrt{[(\Delta B_{11}''-\Delta B_{22}'')^2+4\Delta B_{12}''\Delta B_{21}'']} \tag{2.42}$$

where B_1 and B_2 are the dielectric impermeabilities along the minor and the major axes of the cross-section ellipse respectively. The refractive indices along these two directions can be calculated from $n_1 = 1/\sqrt{B_1}$, and $n_2 = 1/\sqrt{B_2}$. In the above two equations, $\Delta B_{12}'' = \Delta B_{21}''$ for semiconductors with cubic symmetry.

The image intensity distribution for a mixed dislocation can be obtained by following exactly the same procedure taken to calculate the intensity distribution for a semicon-

ductor disc under diametrical compression in Section 2.3. The final expression for the intensity I will be the same as Eqn.(2.12) and is rewritten here for convenience.

$$I = (A^2/2)\ \sin^2 2(\alpha-\beta)\ \sin^2[\pi d(1/\lambda_1 - 1/\lambda_2)]\ , \qquad (2.43)$$

where A is the amplitude of the incident wave, α is the angle the polarizer makes with respect to the sample x_1'' axis, β is the angle given by

$$\beta = (1/2)\ \tan^{-1}\ [(\Delta B_{12}'' + \Delta B_{21}'')/(\Delta B_{11}'' - \Delta B_{22}'')]\ , \qquad (2.44)$$

d is the sample thickness along the x_3'' direction, $\lambda_1 = \lambda/n_1$, $\lambda_2 = \lambda/n_2$, and λ is the wavelength of the incident light in vacuum. In the above equation, $\Delta B_{12}'' = \Delta B_{21}''$ for semiconductors with cubic symmetry.

The critical steps in the process, hence, involve calculation of the direction cosines between the stress axes system and the sample axes system for any arbitrary orientation of the dislocation line within the crystal, and calculation of the edge and the screw components of the Burger vector from a knowledge of the angle between the dislocation line and its Burger vector. The knowledge of the sample orientation gives the direction cosines between the sample axes and the crystal principal axes and can be calculated directly from Eqns.(2.34) or (2.35) for the {100} or the {111} oriented samples respectively if the angle ϕ or γ is known. Once the dielectric impermeabilities along the sam-

ple axes are computed, the rest of the procedure of obtaining the intensity of the transmitted light through the sample is similar to the one described for the diametrical loading case given in Section 2.3. The problem though more tedious can be extended in a straightforward manner to the cases for which the incident light is not perpendicular to the sample. Even though this latter step is not carried out in this work here, an extension of the algorithm developed here will extend the analysis to cases involving non-perpendicular incidence of light onto the sample.

The algorithm developed in this work here is general in nature in that it can be used to generate a variety of data base for the images of dislocations with different orientations within the crystal, varying directions of the Burger vector with respect to the dislocation line, different sample orientations and varying incident light polarization directions. Then an image matching procedure can be used to compare the experimentally observed images to the simulated ones. This can, in principle, yield the information about the type of dislocation, its position, its orientation and the direction of its Burger vector. The advantages of this approach are that the process is non-destructive and that it is fast.

In the next section, a few specific cases are taken to illustrate the procedure of obtaining the fringe patterns

of various types of dislocations. The simulation results are presented in the next chapter.

2.5 Use of the Algorithm for Some Special Cases

As stated in Section 2.4.3, the algorithm developed for the calculation of the intensity distribution around dislocations is quite general in nature in that it can be used for a variety of situations. However, the critical steps of the algorithm include feeding the proper angles between the three axes systems to the computer program for the calculation of the direction cosines. Also the angle between the dislocation line and the Burger vector must be known for resolving the edge and screw components of the dislocation.

For any crystal lattice, the number of possible orientations of the dislocation line and the Burger vector is large. For example, in the most general case, the dislocation line can lie in any arbitrary direction making an arbitrary angle with the Burger vector. This shows the vastness of the problem encountered. However, the symmetry of the cubic crystal lattice cuts down the favorable orientations of the dislocation line and the Burger vector considerably. Chou [8] reported that for cubic lattices, the number of favorable orientations are four and they are given in Table 2.4.

Table 2.4

Most favorable orientations of the dislocation line and the Burger vector for a cubic lattice (after [8]).

Dislocation line direction	Burger vector on the crystal plane
[100]	{100}
[100]	{110}
[110]	{100}
[110]	{110}

This simplifies the problem considerably. In the following subsections specific cases are taken to illustrate the use of the algorithm for simulation of dislocation images.

2.5.1 An edge dislocation with the dislocation line along the <100> direction and the Burger vector on (001) plane on a (100) oriented sample

For this case the angle κ in Fig.2.8 is 90° as this is the case of a pure edge dislocation. It is assumed that the sample is (100) oriented with the crystal principal axis x_1' aligned with the sample axis x_3'' and is coming out from

the plane of the paper, and the axes x_2' and x_3' are aligned with the sample axes x_1'' and x_2'' respectively. Thus the angle ϕ in Fig.2.10 is zero. This assumption is made for convenience without losing generality. Also for this case the stress axes (x_1,x_2,x_3) are aligned with the sample axes (x_1'',x_2'',x_3''), with the dislocation line along the stress axis x_3 and the Burger vector along the axis x_1. Hence the angles between the sample axes and the stress axes are given by $\zeta_1 = 0°$, $\zeta_2 = 90°$, $\zeta_3 = 90°$, $\eta_1 = 90°$, $\eta_2 = 0°$, $\eta_3 = 90°$, $\chi_1 = 90°$, $\chi_2 = 90°$, and $\chi_3 = 0°$. The direction cosines between these two axes systems can be computed from Eqn.(2.30), and the stresses transformed from the stress axes system to the sample axes system using Eqn.(2.32). The transformation for this case yields:

$$\begin{aligned}
\sigma_{11}'' &= \sigma_{11} \ , \\
\sigma_{12}'' &= \sigma_{21}'' = \sigma_{12} \ , \\
\sigma_{13}'' &= \sigma_{31}'' = \sigma_{23}'' = \sigma_{32}'' = 0 \ , \\
\sigma_{22}'' &= \sigma_{22} \ , \\
\sigma_{33}'' &= \sigma_{33} \ .
\end{aligned} \tag{2.45}$$

The direction cosines between the sample axes and the crystal axes can now be computed from Eqn.(2.34) for $\phi = 0°$. The stress components are converted to the crystal principal axes system using Eqn.(2.36). For this case, they are given by:

$$\begin{aligned}
\sigma_{11}' &= \sigma_{33}'' \ , \\
\sigma_{12}' &= \sigma_{21}' = \sigma_{13}' = \sigma_{31}' = 0 \ ,
\end{aligned}$$

$$\sigma'_{22} = \sigma''_{11} ,$$

$$\sigma'_{23} = \sigma'_{32} = \sigma''_{12} ,$$

$$\sigma'_{33} = \sigma''_{22} . \qquad (2.46)$$

The changes in the dielectric impermeabilities in the crystal axes can be calculated from Eqn.(2.37). For this case, these are given by:

$$\Delta B'_{11} = \pi_{1111}\sigma'_{11} + \pi_{1122}(\sigma'_{22} + \sigma'_{33}) ,$$

$$\Delta B'_{12} = \Delta B'_{21} = \Delta B'_{13} = \Delta B'_{31} = 0 ,$$

$$\Delta B'_{22} = \pi_{1111}\sigma'_{22} + \pi_{1122}(\sigma'_{11} + \sigma'_{33}) ,$$

$$\Delta B'_{23} = \Delta B'_{32} = 2\pi_{1212}\sigma'_{23} ,$$

$$\Delta B'_{33} = \pi_{1111}\sigma'_{33} + \pi_{1122}(\sigma'_{11} + \sigma'_{22}) . \qquad (2.47)$$

These changes in the dielectric impermeability tensor elements are transformed back to the sample axes using Eqn.(2.38). These are given by:

$$\Delta B''_{11} = \Delta B'_{22} ,$$

$$\Delta B''_{12} = \Delta B''_{21} = \Delta B'_{23} ,$$

$$\Delta B''_{13} = \Delta B''_{31} = \Delta B''_{23} = \Delta B''_{32} = 0 ,$$

$$\Delta B''_{22} = \Delta B'_{33} ,$$

$$\Delta B''_{33} = \Delta B'_{11} . \qquad (2.48)$$

These values of the dielectric impermeabilities are used in Eqns.(2.41) and (2.42) for the calculation of the refractive indices along the minor and the major axes of the index ellipse respectively. The rest of the procedure of obtaining the resultant intensity distribution is quite straightforward as illustrated at the end of Section 2.4.3.

2.5.2 A screw dislocation with the dislocation line along the <010> direction and the Burger vector on (001) plane on a (100) oriented sample

For this case, the angle κ in Fig.2.8 is zero as it is a pure screw dislocation. Pure screw dislocations cannot be viewed along the dislocation line as shown in Appendix D. For this example, the dislocation line is assumed to be along the sample x_1'' axis in Fig.2.9, which is also the stress axis x_3. The stress axis x_2 is coincident with the sample axis x_2'', and the stress axis x_1 is along the sample $-x_3''$ direction in Fig.2.9. It is also assumed that the sample axes system is aligned with the crystal axes system, with the angle ϕ in Fig.2.10 being equal to zero, and the direction cosines between the sample axes and the crystal axes are given by Eqn.(2.34) with $\phi = 0°$. Hence, the sample is a (100) plane with the dislocation line along <010> direction, and the Burger vector lying on the (001) plane and pointing along the <010> direction.

The direction cosines in Eqn.(2.30) can be obtained from the angles between the sample axes and the stress axes which for this case are given by $\zeta_1 = 90°$, $\zeta_2 = 90°$, $\zeta_3 = 0°$, $\eta_1 = 90°$, $\eta_2 = 0°$, $\eta_3 = 90°$, $\chi_1 = 180°$, $\chi_2 = 90°$, and $\chi_3 = 90°$. The rest of the procedure is similar to the one described in Section 2.5.1 and is not repeated here for brevity.

2.5.3 A mixed dislocation with the dislocation line along the <110> direction and the Burger vector on (001) plane on a (111) oriented sample with an angle κ between the dislocation line and the Burger vector

For this case, the sample axes system chosen is shown in Fig.B.3a) on page 125. This is the case for a (111) oriented sample, and, hence, the calculation of the direction cosines is little tedious. The relation between the sample axes (x_1'', x_2'', x_3'') and stress axes (x_1, x_2, x_3) is shown in Fig.2.11a) and the axes systems as seen looking along direction x_1'' is shown in Fig.2.11b). In Fig.2.11a), the crystal principal axes are denoted by (x_1', x_2', x_3'). The dislocation line is along <110> direction and the Burger vector is on (001) plane which is the crystal plane $x_1'x_2'$. The stress axis x_1 must also lie on $x_1'x_2'$ plane. The sample is rotated such that axis x_1'' is parallel to axis x_1, and the angle γ in Fig.B.3a) on page 125 is equal to 90°. The knowledge of the angle κ permits the resolution of the Burger vector to its edge and screw components. The stresses now need to be transformed to the sample axes from the stress axes using Eqn.(2.32). For this the direction cosines a_{ij} needed can easily be computed from Eqn.(2.30) with reference to Fig.2.11b). A direct inspection shows that $\zeta_1 = 0°$, $\zeta_2 = 90°$, $\zeta_3 = 90°$, $\eta_1 = 90°$, $\eta_2 = 35.26°$, $\eta_3 = 125.26°$, $\chi_1 = 90°$, $\chi_2 = 54.74°$, and $\chi_3 = 35.26°$. These stresses can be converted to the crystal principal axes by Eqn.(2.36)

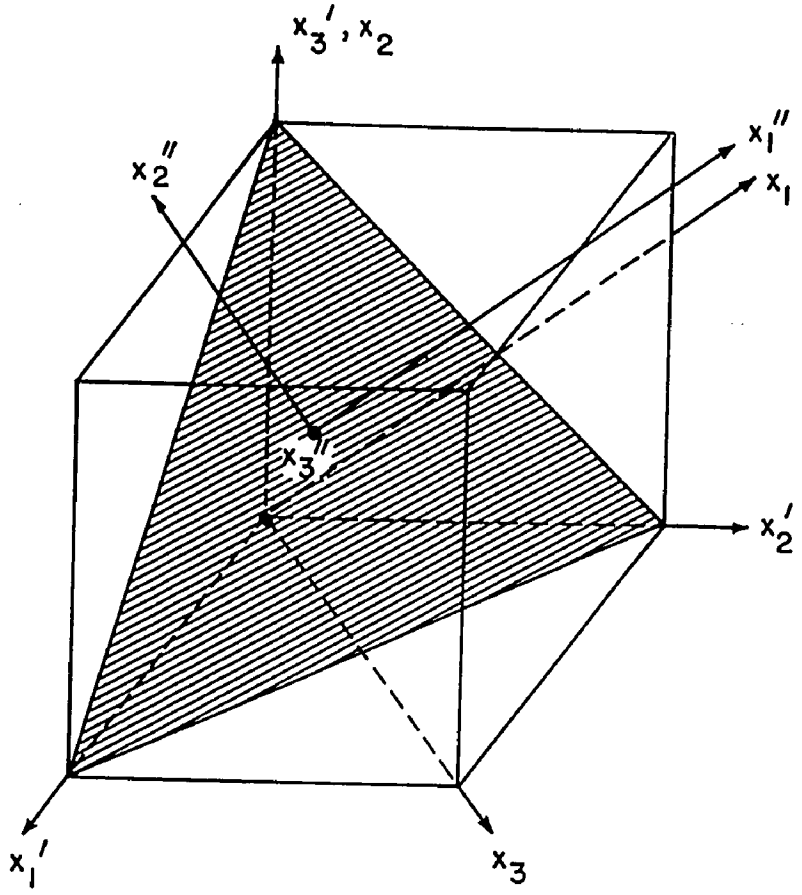

Fig.2.11 a) The relation between the three axes systems and b) the axes systems as seen looking along direction x_1''.

using the direction cosines given in Eqn.(2.35). The rest of the procedure of obtaining the intensity distribution equation is identical to that described in Section 2.4.3 and is not repeated here for conciseness.

2.5.4 A mixed dislocation with the dislocation line along the <110> direction and the Burger vector on (001) plane on a (100) oriented sample with an angle κ between the dislocation line and the Burger vector

For this case, the knowledge of κ gives the edge and the screw components of the Burger vector for this dislocation. It is assumed that the sample axes system and the crystal principal axes system are aligned with $\phi = 0°$ in Fig.2.10. The axes systems as seen looking along direction x_2'' is shown in Fig.2.12. The dislocation axis x_3 is along the <110> direction, i.e., at 45° with respect to the sample axis x_3'' on the sample $x_1''x_3''$ plane in Fig.2.12. The stress axis x_1 is at 90° with respect to axis x_3 and the Burger vector lies on the plane x_1x_3. This defines the direction of the stress axis x_1 for this case. The stress axis x_2 is perpendicular to both x_1 and x_3 and for this example, is coincident with the sample axis x_2''. The angles between the stress axes and the sample axes in Eqn.(2.30) can now be given by $\zeta_1 = 45°$, $\zeta_2 = 90°$, $\zeta_3 = 45°$, $\eta_1 = 90°$, $\eta_2 = 0°$, $\eta_3 = 90°$, $\chi_1 = 135°$, $\chi_2 = 90°$, and $\chi_3 = 45°$, and the result-

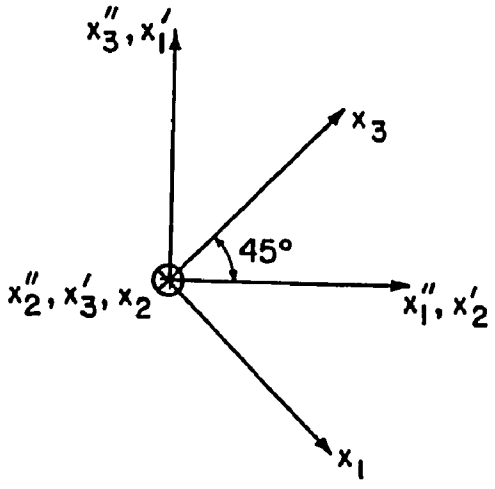

Fig.2.12 The three axes systems as seen looking along direction x_2''.

ing direction cosines are calculated from Eqn.(2.30). The rest of the procedure of obtaining the parameter values to be used in the intensity distribution equation is identical to that described at the end of Section 2.4.3.

Thus, four specific cases of interest are taken into consideration here to illustrate the procedure for the calculation of the critical parameter values which are used in the equation of the intensity distribution around dislocations. However, the algorithm is in no way restricted only to these special cases. Any arbitrary orientation of the sample, of the dislocation line with respect to the crystal principal axes, and of the Burger vector with respect to the dislocation line can be analyzed using the algorithm developed in Section 2.4.3. This makes the algorithm extremely general in nature though the calculation of the angles may, in some cases, be tedious.

CHAPTER 3

RESULTS AND DISCUSSIONS

3.1 Experimental Setup

A dark field plane polariscope was constructed to view the fringe patterns of diametrically loaded discs of silicon and gallium arsenide as well as the fringe patterns produced by the defects within the crystal. The setup is shown in Fig.3.1. Figure 3.1a) shows a general view of the setup while Fig.3.1b) shows the schematic arrangement. The light source used was a linearly polarized 19-mW He-Ne laser (Jodon HN-50) tuned to 1.15 μm wavelength. Both silicon and gallium arsenide with absorption cutoff wavelengths of 1.11 μm and 0.89 μm respectively are transparent at 1.15 μm wavelength. The spatial sensitivity of the laser is shown in Fig.3.2, which shows the small beam divergence full angle of 0.63 mrad at 1.15 μm wavelength. The nominal output power of the beam is 12.5 mW, the beam diameter is 2.34 mm at the exit port of the laser, and the beam comprising of the TEM_{oo} mode is vertically polarized.

A laser light source was selected over the more conventional filtered incoherent light sources because of its monochromaticity. The use of a laser as the source of illumination reduces the washing out effect observed in images formed with wider bandwidth sources. Also, the monochromat-

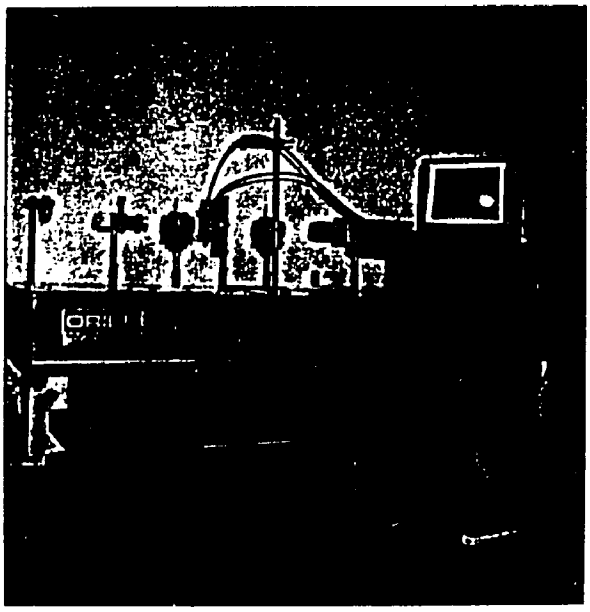

a)

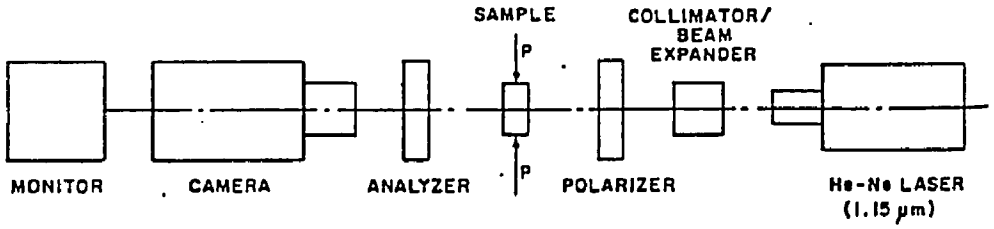

b)

Fig.3.1 a) The general view and b) the schematic arrangement of the experimental setup.

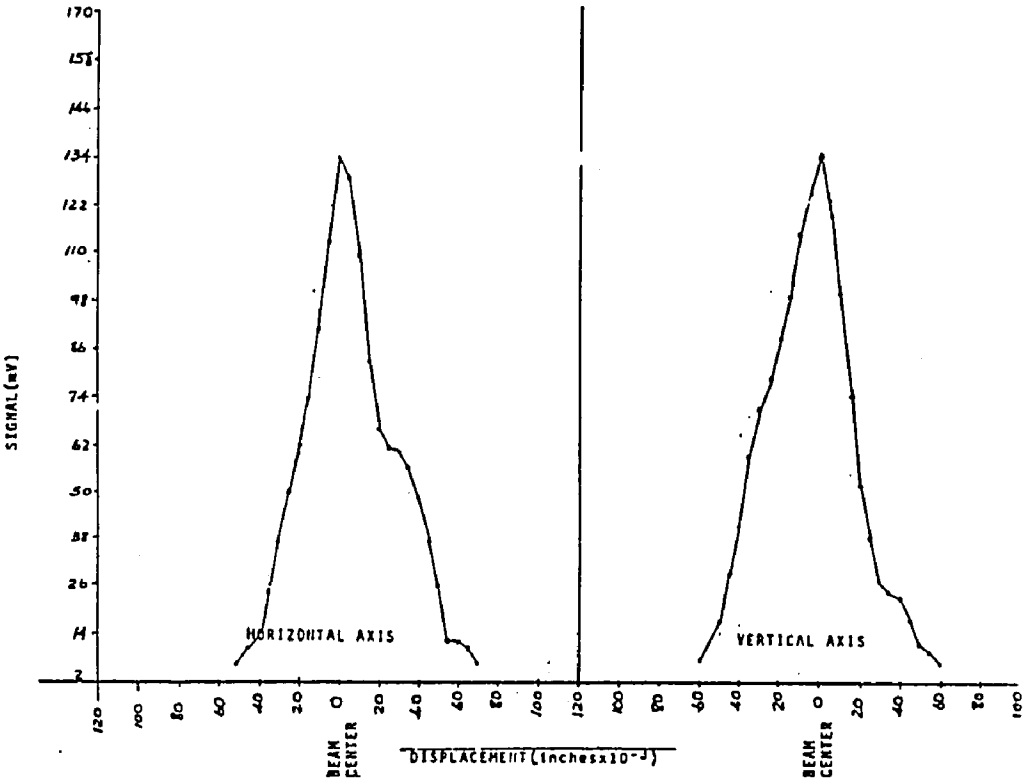

Fig.3.2 The spatial sensitivity of the laser (Jodon HN-50) used in this work.

icity and polarization of the laser light source enhance the resolution and contrast of the images [32]. A comparison of Figs.3.5a) and 3.6a) with Fig.3.7a), which is reproduced here from the reported work of Appel et al. [20], clearly shows improved contrast in the first two cases using a laser light source. An unfortunate artifact of the use of the laser is the production of speckle in the images. This can be seen in the experimental pictures as an overall graininess in the images.

Because of the size of the laser, the optical bench was folded into a two-tier arrangement using two 45° mirrors. The optical components were mounted on an Oriel vibration-free table. After the laser beam got reflected from the second mirror, it was passed through a spatial filter - beam expander arrangement. The spatial filter got rid of any unwanted stray lights, and the beam expander expanded the beam to a workable diameter of approximately 2.5 cm. The beam was then passed through a sheet film polarizer which transmitted the infrared light satisfactorily. In theory at least the use of the polarized laser beam would have precluded the need for using a polarizer ahead of the sample. However, even in the beam expanded state, the laser source proved to be too powerful and blinded the infrared sensitive camera used as the detector. Because of the need to rotate the plane of polarization of the light source, and also the need to reduce the light intensity, a polarizer was inserted into the optical path ahead of the sample.

The light was then passed through the sample and a sheet film type analyzer. The axis of the analyzer was at 90° to that of the polarizer for the dark-field polariscope configuration. After the analyzer, an infrared sensitive vidicon camera (Hamamatsu C-1000-03) was used to pick up the image and display it on a video monitor through the camera control unit (CCU). Typical signal output with illumination for the vidicon camera is shown in Fig.3.3. The vidicon camera used Lead Sulfide (PbS) as the detector material and has the sensitivity of 15 nA/μW at 1.15 μm wavelength. The camera has a resolution of 600 lines, the absolute image distortion of ± 2.0%, and the overall shading of less than 20%. The shading is the variation in the amplitude of the electrical signal when the illumination is uniform. The video monitor (Ikegami PM-125A) has a resolution of 700 lines and distortion less than 10%.

The experimental pictures were photographed directly from the screen of the monitor with a 35 mm camera. For the study of diametrical compression, the samples were placed between the polarizer and the analyzer and loaded by a pneumatically operated piston. The anvils of the compressor were made of flame-hardened mild steel and pieces of index card were used to protect the edges of the samples during compression. The cross-section of the piston plunger was 1 sq.in. ±1% in area. A pressure gauge calibrated in psig allowed the compressive force on the sample disc to be read

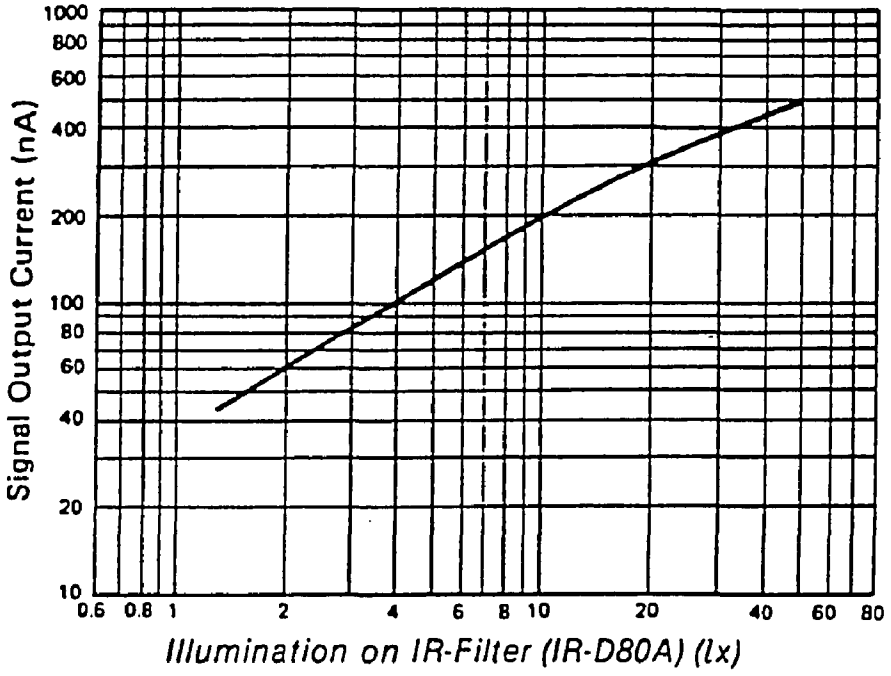

Fig.3.3 Typical signal output with illumination for the Hamamatsu (C-1000-03) vidicon camera.

directly. Figure 3.4 indicates the details of the arrangement for the application of compressive loads to the samples. For the study of defects, the samples were placed on a vertical X-Y stage.

3.2 Results for Diametrically Compressed Semiconductor Discs

The silicon samples used in this experiment were cut along the {111} orientation from a rod of single crystal silicon of 1.746 cm diameter. In order to prevent loss of intensity due to surface scattering, the sample surfaces were polished to a mirror finish. The polishing was done manually on both sides of the samples with SiC powder on a glass plate with light hand pressure, using a successively finer abrasive medium starting with 200-grit powder size and ending with 1200-grit powder size. After the mechanical polishing was completed, the samples were chemically polished for 2 min in CP-4A solution containing three parts HF, five parts HNO_3, and three parts CH_3COOH by volume.

Figure 3.5a) shows the observed image at 1.15 μm under the plane polariscope for a {111} oriented silicon crystal disc of 0.873 cm radius and 0.16 cm thickness. The applied load was 19 kg and the angle of polarization α in Fig.2.1 was 90°. Figure 3.5b) is the simulated image for these same conditions obtained from the analysis given in Section 2.3.

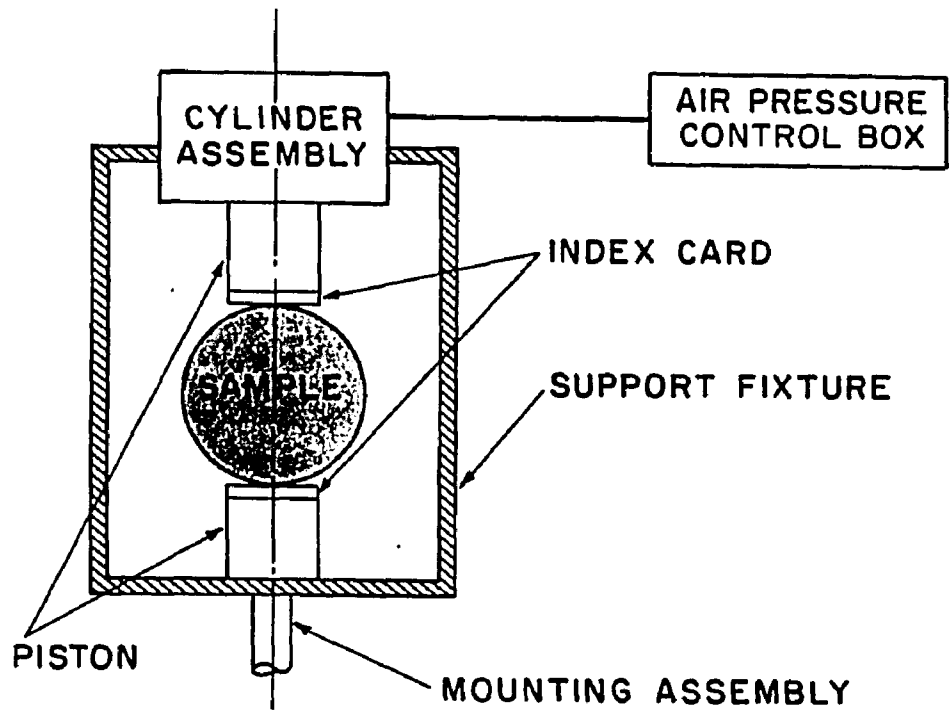

Fig.3.4 The arrangement for application of compressive load on samples.

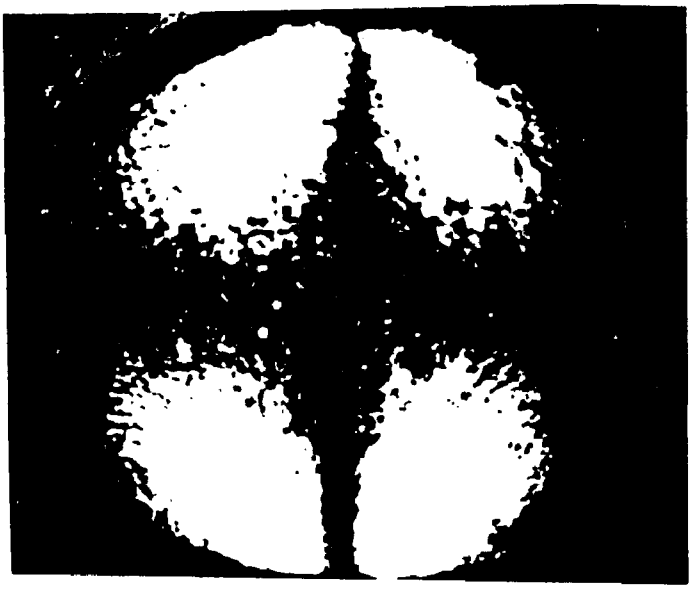

a)

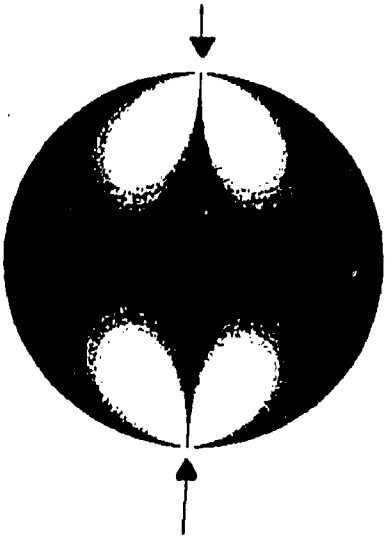

b)

Fig.3.5 a) Experimentally observed and b) simulated image on a {111} oriented silicon disc of radius 0.873 cm and thickness 1.6 mm under a diametrical compression load of 19 kg and angle of polarization α = 90°. Arrows indicate the loading direction.

The intensity levels shown in Fig.3.5b) were obtained by normalizing the maximum level to unity and then plotting in sixteen gray scale levels utilizing a logarithmic scale. Any intensity more than 0.1 in the normalized scale is plotted as white in the computed figure. The rest of the values are plotted in a linear gray scale with successive decrements of 0.1. Figure 3.6 compares the observed and the simulated images for the same conditions as Fig.3.5 but with the load now increased to 38 kg. A close observation of the simulated image of Fig.3.6b) shows small lobes around the point of loading. The latter are also present in the experimentally observed image indicating a good match between the computer simulations and the experimentally observed images. The small lobes which are present around the points of loading are actually the second order fringes. As the load increases, the order of the fringes also increases. In Fig.3.5, only the first order fringe is present.

The data reported by Appel et al. [20] of a silicon sample with radius R = 4.37 mm, thickness d = 1.88 mm, and the polarization angle $\alpha = 60^{\circ}$ are shown in Fig.3.7a). The crystal orientation of the sample was not mentioned in their paper. In this work, images were simulated assuming the sample orientation to be {100} and {111}. The results are shown in Figs.3.7b) and 3.7c), respectively, for the {100} and the {111} oriented silicon samples. The parameters used in the simulation were the same as those reported by Appel et al. [20].

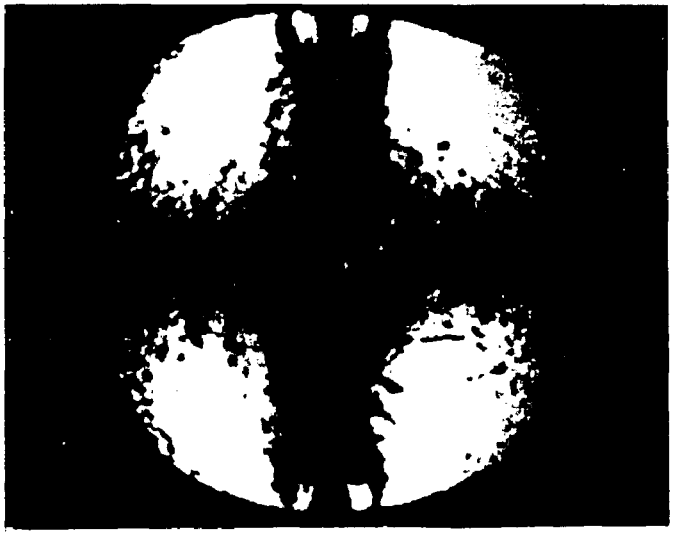

a)

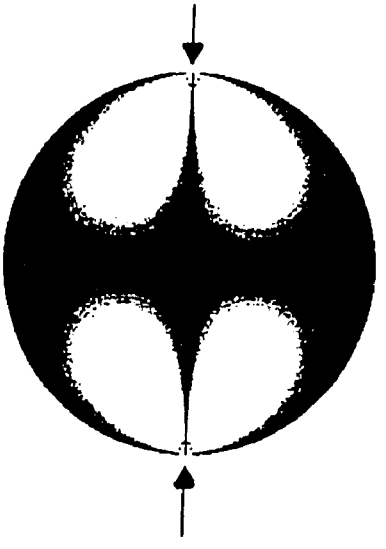

b)

Fig.3.6 a) Experimentally observed and b) simulated image on a {111} oriented silicon disc of radius 0.873 cm and thickness 1.6 mm under a diametrical compression load of 38 kg and angle of polarization $\alpha = 90°$. Arrows indicate loading direction.

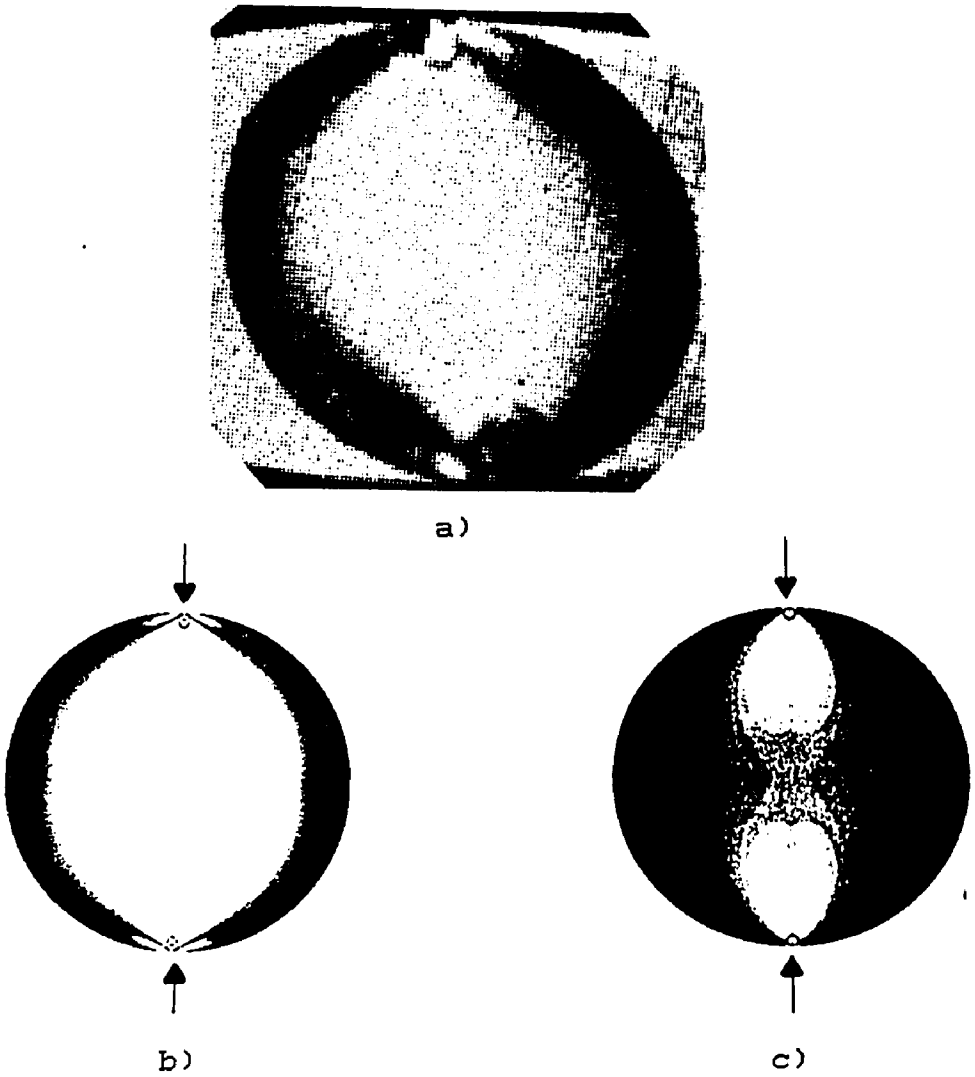

Fig.3.7 a) Experimentally observed image reported by Appel et al.[20] for a silicon sample of unknown orientation with a radius of 4.37 mm, thickness of 1.88 mm, load of 38 kg, and the angle of polarization $\alpha = 60°$. b) Simulated image for the same conditions as a) for {100} oriented sample. c) Simulated image for the same conditions as a) for {111} oriented sample. Arrows indicate the loading direction.

Comparing Fig.3.7a) with Figs.3.7b) and 3.7c), an excellent match is seen between the simulated image and the experimentally observed image for a {100} oriented sample, whereas the simulated image for a {111} oriented sample shows a poor match with the experimental one. The best match for the {100} orientation simulation was obtained for the case in which the load was applied along one of the crystal principal axes. Hence, we infer that the sample used in the work reported by Appel et al. [20] was of {100} orientation. These results have been published elsewhere [54].

The algorithm developed in this work, hence, can not only be used to predict the interference fringe pattern for any arbitrarily applied stress direction, but can also be used to predict the orientation of an unknown sample by putting it under a compressive load and then by comparing the resulting fringe pattern with the simulated ones.

The algorithm was also used to determine the fringe patterns for a diametrically loaded GaAs disc. The disc was single crystal undoped semi-insulating GaAs of {100} orientation, grown by the Liquid Encapsulated Czochralski (LEC) technique. It was 1.9 cm in diameter and 1.65 mm in thickness. Both its surfaces were polished to a mirror finish. Figure 3.8a) shows the simulated pattern for the above disc under a diametrical compression load of 20 kg, and the angle

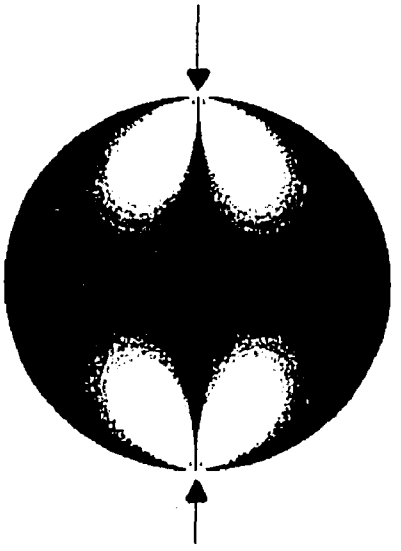

a)

b)

Fig.3.8 a) Simulated and b) experimentally obtained image on a {100} oriented gallium arsenide disc 1.9 cm in diameter and 1.65 mm in thickness under a diametrical compression load of 20 kg and angle of polarization $\alpha = 0^{\circ}$. Arrows indicate the loading direction.

of polarization α of 0°. Figure 3.8b) shows the experimentally obtained image for the disc subjected to the same conditions as in Fig.3.8a). Figures 3.9a) and 3.9b) show the simulated pattern and the experimentally obtained image of the same disc but with the load now increased to 40 kg and the angle of polarization α of the incident light changed to 45°.

Although the simulated and the experimentally observed images seem to be similar in nature, the match is not quite as good as that obtained for the Si discs under diametrical compression. The reason for this may well lie in the crystalline quality of the GaAs discs used in this work. Under no-load condition, there appeared an irregularly shaped bright area at the lower right hand corner of the experimental images indicating some built-in stress in the material. Built-in stress can be present in a wafer due to the crystal growth process or the subsequent processing procedures. This built-in stress seems to interfere with the applied stress resulting in differences between the simulated and the observed images on the lower right side of the wafer. Otherwise, the overall match is good and confirms the general nature of the algorithm developed here. This algorithm can be used for a variety of materials provided their piezooptic coefficients are known. The result reported here on GaAs disc under diametrical compression has been published elsewhere [55].

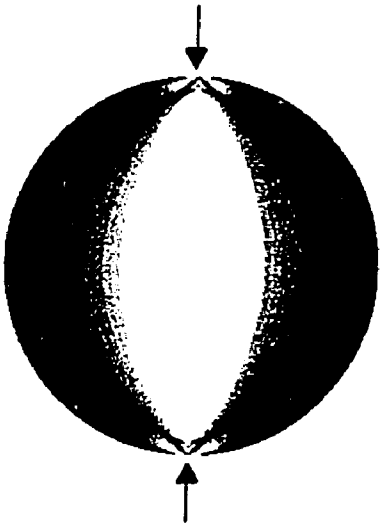

a)

b)

Fig.3.9 a) Simulated and b) experimentally obtained image on a {100} oriented gallium arsenide disc of diameter 1.9 cm and thickness 1.65 mm under a diametrical compression load of 40 kg and angle of polarization $\alpha = 45°$. Arrows indicate the loading direction.

3.3 The Stress-Optic Coefficient

Isotropic materials with spherical indicatrices can become anisotropic when stressed either by some external means such as the application of a load or by internal means such as defects within the material. The stress field can cause optical anisotropy and as a result the material can become birefringent with the indicatrix represented by an ellipsoid. The two components while traversing through the sample along the major and the minor axes of the cross-sectional ellipse of the indicatrix will build up a phase difference ϕ between them given by

$$\phi = C(\sigma_1-\sigma_2)2\pi d/\lambda \ , \qquad (3.1)$$

where C is the stress-optical constant of the material, σ_1 and σ_2 are the diagonalized elements of the stress matrix given by

$$\sigma_1 = (\sigma_{11}+\sigma_{22})/2 + (1/2)\sqrt{[(\sigma_{11}-\sigma_{22})^2+4\sigma_{12}^2]} \qquad (3.2)$$

and

$$\sigma_2 = (\sigma_{11}+\sigma_{22})/2 - (1/2)\sqrt{[(\sigma_{11}-\sigma_{22})^2+4\sigma_{12}^2]} \ . \qquad (3.3)$$

Here σ_{11}, σ_{22}, and σ_{12} are given by Eqns.(2.1-2.3) respectively, d is the material thickness, and λ is the wavelength of the incident light. This approach assumes a constant value of the stress-optic coefficient. However, the stress-optic coefficient can be taken as a constant only for isotropic materials. In an anisotropic medium, which is the

case for a diametrically compressed semiconductor sample, the value of the stress-optic coefficient C will depend on the orientation of the load with respect to the principal crystal axes. The values of C will also vary, in general, from one point of the sample surface to the next for a given load. However, the values of C do not depend on the magnitude of the applied load provided that a linear relationship between the pressure and the phase retardation holds. Giardini [14] has reported that this linearity holds upto a pressure of 450 kg/cm^2 for silicon.

In this work, a different approach is taken to examine the behavior of the stress-optic coefficient C for the case of diametrically compressed discs of semiconductors specifically silicon and gallium arsenide. The incident light while passing through the stressed sample splits into two components with different indices of refraction, and thus travels with different velocities. The velocity of light within a material with index of refraction n is given by c/n, where c is the velocity of light in free space. The light travelling along the minor axis has a velocity c/n_1 and that travelling along the major axis has a velocity c/n_2, with corresponding wavelengths λ_1 and λ_2 where n_1 and n_2 are the respective indices of refraction in the two directions. The phase shift ϕ_1 suffered by the component along the minor axis while traversing through the sample is given by $\phi_1 = 2\pi d/\lambda_1$. The phase shift ϕ_2 suffered by the

component along the major axis while traversing through the sample is given by $\phi_2 = 2\pi d/\lambda_2$. The phase angle difference ϕ between these two components is given by

$$\phi = \phi_2 - \phi_1 = 2\pi d(1/\lambda_2 - 1/\lambda_1) ,$$

or

$$\phi = 2\pi d(n_2 - n_1)/\lambda , \qquad (3.4)$$

where λ is the wavelength of the incident light in free space.

Comparison of Eqns.(3.1) and (3.4) gives

$$C = (n_2 - n_1)/(\sigma_1 - \sigma_2) . \qquad (3.5)$$

Equation (3.5) was used to compute the value of C at each point on the wafer for a semiconductor disc under diametrical compression. For both Si and GaAs {100} oriented samples, the value of C was found to vary along the sample surfaces. The value of C was also found to depend on the orientation of the load with respect to the principal crystal axes. However, for both Si and GaAs {111} oriented samples, C was found to be independent of the loading orientation or the position on the sample surfaces as expected from the crystal symmetry.

Consideration of the variation in the stress-optic coefficient C as carried out in this work here is novel as all the previous reported works in the subject have assumed a constant value for C as mentioned earlier in Section 1.2.

Only Bullough [25] had acknowledged that for a cubic crystal under stress, C should be a function of position as evident from the details of the results of this work.

The values of C calculated from the simulation as a function of position on the sample surface for a {100} oriented silicon disc are shown in Fig.3.10. Figure 3.11 gives similar results for a {100} oriented gallium arsenide disc. In both of these figures, the orientation of the load with respect to the principal crystal axes lying on the wafer surface is defined by the angle ϕ as shown in Fig.A.1 on page 121. Figure 3.10a) shows the values of the stress-optic coefficient C as a function of position on a {100} oriented Si surface for $\phi = 45°$, while Fig.3.10b) shows the same for $\phi = 75°$. Similarly, Figs.3.11a) and 3.11b) show the values of C for a {100} oriented GaAs sample for $\phi = 45°$ and $\phi = 75°$ cases respectively.

From Figs.3.10 and 3.11 it can be clearly seen that C cannot be taken as a constant with position on a wafer surface for a given load. As the angle of loading is changed, the pattern of C on the wafer changes. Therefore, it is a function of the orientation of the loading axes with repect to the principal crystal directions. For a {100} oriented silicon disc under diametrical compression, the values of C ranged from 2.0×10^{-12} cm^2/dyne to 3.0×10^{-12} cm^2/dyne and are plotted in Fig.3.10 in a linear gray scale with 11 lev-

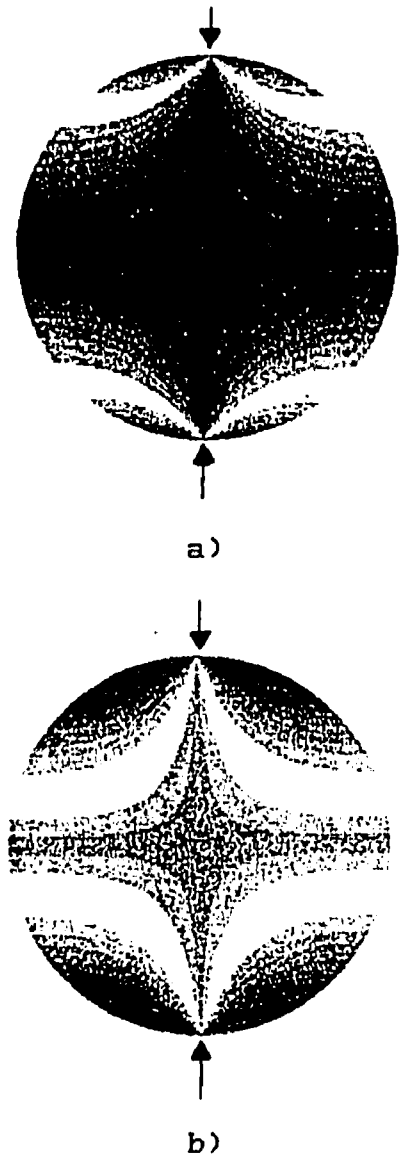

Fig.3.10 Wafer map of the computed values of the stress-optic coefficient C for a) ϕ = 45° and b) ϕ = 75° for a load of 19 kg for a {100} oriented silicon wafer with diameter of 1.746 cm and thickness of 1.6 mm. Plotted in 11 levels of a linear gray scale with white for C > 2.95×10^{-12} cm²/dyne and black for C < 2.05×10^{-12} cm²/dyne. Arrows indicate the loading direction.

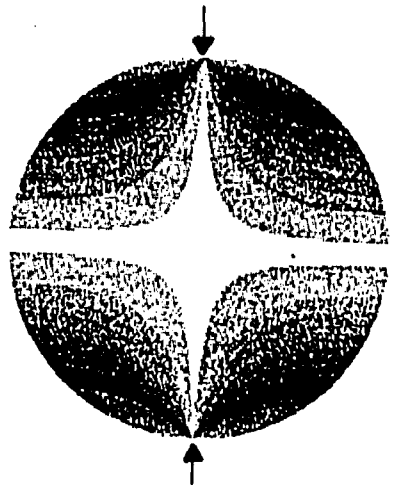

a)

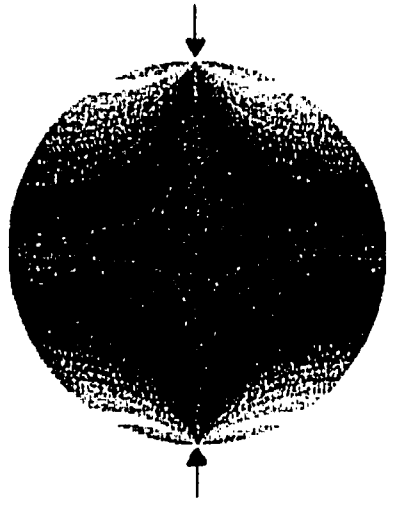

b)

Fig.3.11 Wafer map of the computed values of the stress-optic coefficient C for a) $\phi = 45°$ and b) $\phi = 75°$ for a load of 20 kg for a {100} oriented gallium arsenide wafer with diameter of 1.9 cm and thickness of 1.65 mm. Plotted in 10 levels of a linear gray scale with white for $C > 2.5 \times 10^{-12}$ cm²/dyne and black for $C < 0.9 \times 10^{-12}$ cm²/dyne. Arrows indicate the loading direction.

els. In the plot, a white scale was employed for $C > 2.95 \times 10^{-12}$ cm²/dyne and a black scale for $C < 2.05 \times 10^{-12}$ cm²/dyne. Intermediate values were plotted in nine levels varying in the shade of gray, with linear spacings. For a {100} oriented gallium arsenide disc under diametrical compression, the values of C ranged from 0.8×10^{-12} cm²/dyne to 2.6×10^{-12} cm²/dyne and are plotted in Fig.3.11 in a linear gray scale with 10 levels. In this plot, a white scale was employed for $C > 2.5 \times 10^{-12}$ cm²/dyne and a black scale for $C < 0.9 \times 10^{-12}$ cm²/dyne. Intermediate values were plotted in eight levels varying in the shade of gray, with linear spacings.

One important point to note is that though C varies as a function of position for a given load, the wafer map of C is independent of the magnitude of the applied load. For instance, Fig.3.10 is plotted for a load of 19 kg; and Fig.3.11 is plotted for a load of 20 kg. However, doubling the load to 38 or 40 kg respectively will not cause these two patterns to change. This is expected as long as the linearity between the stress and the phase retardation holds for the material under consideration.

For {111} oriented silicon or gallium arsenide samples due to the crystal symmetry, the value of C is independent of position for any given load and is also independent of the orientation of the loading axes with respect to the

principal crystal axes. The value obtained from the results of this work for {111} oriented silicon disc under diametrical compression is 2.33×10^{-12} cm²/dyne and that for gallium arsenide disc under diametrical compression is 1.94×10^{-12} cm²/dyne.

The value of C quoted by Appel et al. [20] for silicon is 2.1×10^{-12} cm²/dyne. Bullough [25] reported it as variable from 1.0×10^{-12} cm²/dyne to 2.3×10^{-12} cm²/dyne based on his studies of edge dislocations in silicon. Prussin and Stevenson [16] deduced a value of 2.0×10^{-12} cm²/dyne in their experiment on silicon bars subjected to pure bending. Their reported value compares favorably to those quoted by Bullough and by Appel et al. The values reported by Lederhandler [17] and Nikitenko and Dedukh [33] are little low with magnitudes of 0.95×10^{-12} cm²/dyne and 1.43×10^{-12} cm²/dyne, respectively. Both the works by Appel et al. and by Prussin and Stevenson measured the retardation as a function of the applied stress. From the observed linear relation between them, a mean value of the stress-optic coefficient C was found to fit the data, whereas Bullough adjusted the value of C to make his theoretical simulation of edge dislocations in silicon match with those experimentally observed by Bond and Andrus [22]. The incorporation of the variation of the stress-optic coefficient C in the analysis of the images of dislocations will certainly improve the resolution of the dislocation images, whereas a constant C will only highlight the basic features of the images.

In summary, the work shows that for {100} oriented silicon or gallium arsenide disc under diametrical compression, no unique value of C can be assigned as C varies from point to point on the wafer surface for any given load. The value of C also varies with the orientation of the load with respect to the crystal principal axes as well. However, no such dependence is found for {111} oriented samples due to crystal symmetry properties. For a {100} oriented silicon disc under diametrical compression, the values of C varied between 2.0×10^{-12} cm^2/dyne and 3.0×10^{-12} cm^2/dyne and are consistent with those reported earlier by others. For gallium arsenide, to our knowledge, no data for C has been reported so far. Our work on a {100} oriented gallium arsenide disc under diametrical compression showed that the values of C ranged between 0.8×10^{-12} cm^2/dyne and 2.6×10^{-12} cm^2/dyne. The value of C for a given position on the wafer will not change on increasing the load so long as the tensor elements π_{ijkl} of the piezooptic coefficient matrix remain constant. For {111} oriented silicon and gallium arsenide discs under diametrical compression, the value of C was found to be 2.33×10^{-12} cm^2/dyne and 1.94×10^{-12} cm^2/dyne respectively.

3.4 Results for Dislocation Images

The simulated and the experimental results for dislocations are presented in this section. Figure 3.12 shows the simulation results for a pure edge dislocation on a (100) oriented silicon sample with the dislocation line along the <100> direction making an angle of 90° with the Burger vector. The latter lies on the (001) plane with the angle κ in Fig.2.8 equal to 90°. The dislocation line lies along the direction x_3'' and the Burger vector is oriented along the axis x_1'' of Fig.2.9. For this case, the dislocation is viewed end-on, i.e., along the dislocation line. As shown in Fig.2.9, α is defined as the angle the polarizer makes with the axis x_1''. For this case, the sample axes system and the crystal principal axes system are aligned such that the angle ϕ in Fig.2.10 is equal to zero.

Figures 3.12a), b), c), and d) show the simulation results for the polarization angle α of 0°, 30°, 45°, and 60°, respectively. From the figures, it can clearly be seen that, for this case, when the polarizer makes an angle of 45° with the dislocation slip plane $x_1''x_3''$, the image is brightest with a four-petal rosette pattern with equal lobes.

Figure 3.13 shows the simulation results for a pure screw dislocation on a (100) oriented silicon sample with the dislocation line along <010> direction and the Burger

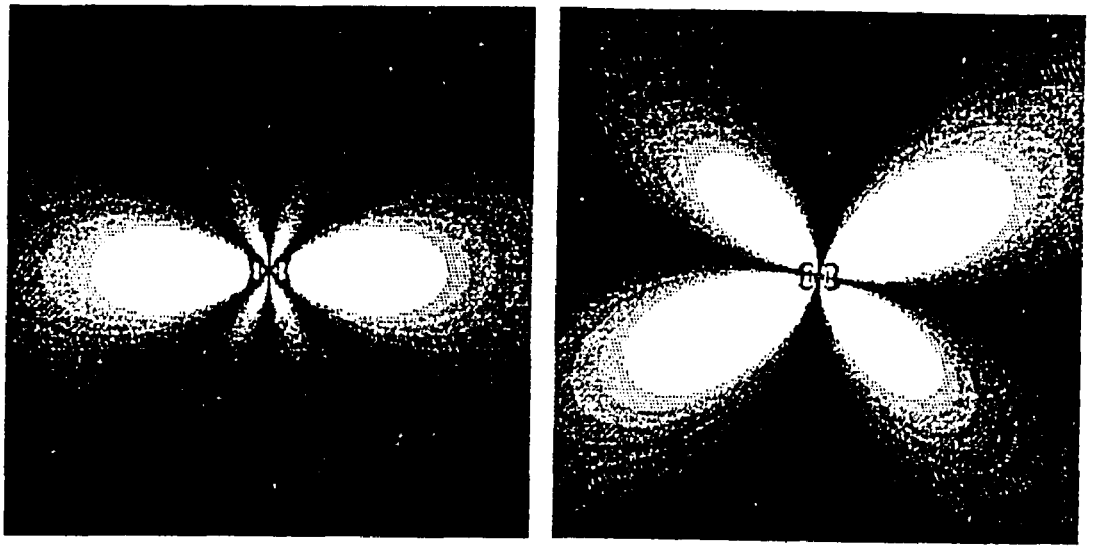

a) $\alpha = 0°$ b) $\alpha = 30°$

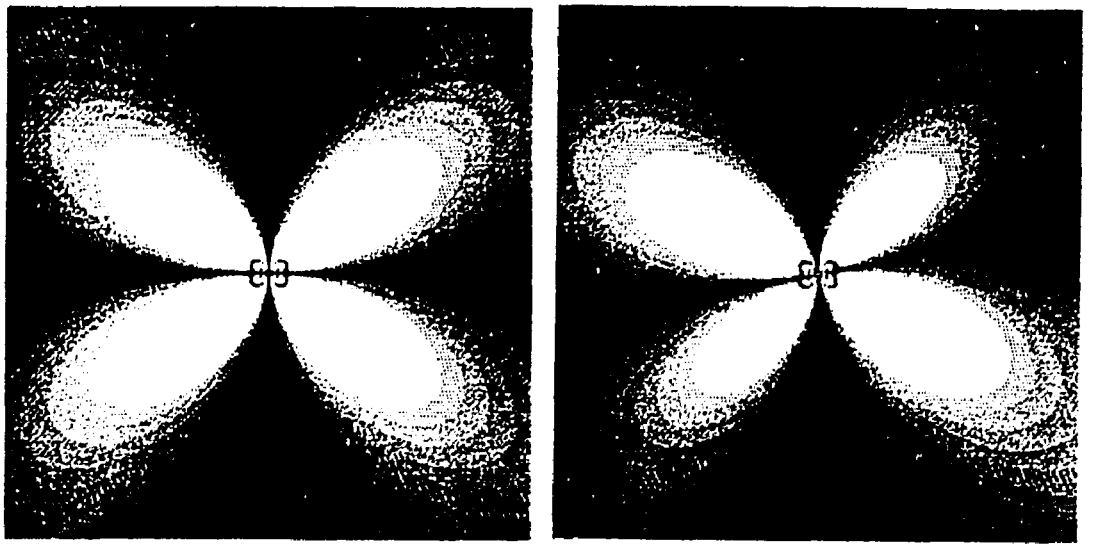

c) $\alpha = 45°$ d) $\alpha = 60°$

Fig.3.12 Simulation results for a pure edge dislocation with the dislocation line along the <100> direction and the Burger vector on (001) plane for a (100) oriented silicon sample. The incident light is along the dislocation line.

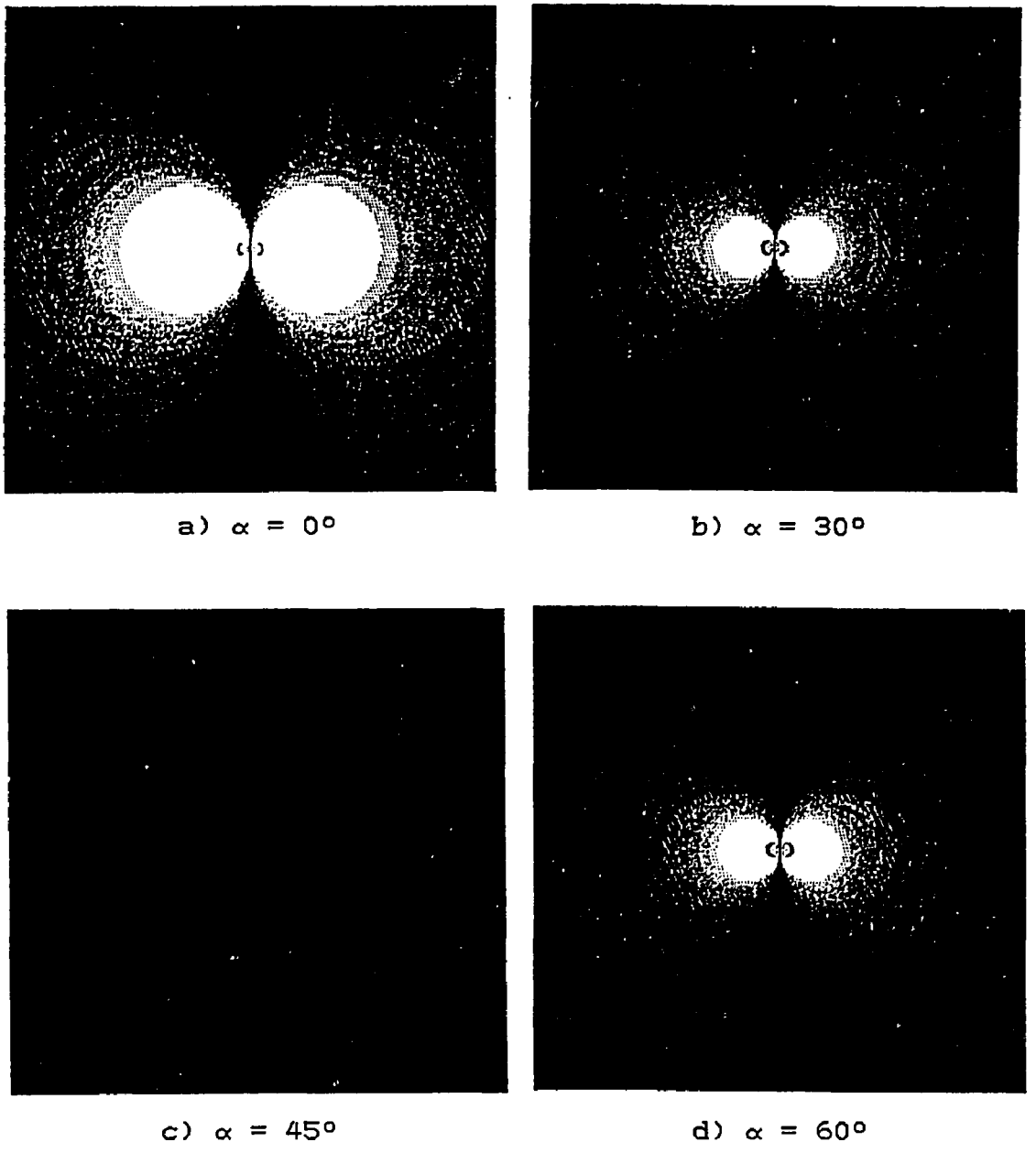

a) $\alpha = 0°$ b) $\alpha = 30°$

c) $\alpha = 45°$ d) $\alpha = 60°$

Fig.3.13 Simulation results for a pure screw dislocation with the dislocation line along the <010> direction and the Burger vector on (001) plane pointing along <010> direction for a (100) oriented silicon sample. The viewing direction is along the <100> axis.

vector on the (001) plane pointing along the <010> direction. It is known that screw dislocations cannot be viewed end-on, i.e., viewed along the dislocation line. An analytical proof is given in Appendix D. Hence, the dislocation line and the Burger vector for this example are chosen along the direction x_1' in Fig.2.9 while the illumination direction is along x_3'. The sample axes and the crystal principal axes systems are aligned for this case such that the angle ϕ in Fig.2.10 is equal to zero.

Figures 3.13a), b), c), and d) show the simulation results for α = 0°, 30°, 45°, and 60°, respectively, where α is the angle between the polarizer axis and the sample axis x_1' as shown in Fig.2.9. From a comparison of Figs.3.12 and 3.13, one can see the differences in the nature of the images for the two cases considered here. The images of a pure edge dislocation when viewed end-on have at least four lobes of approximately elliptical pattern, whereas the images of a pure screw dislocation when viewed at 90° to the dislocation line have two lobes of approximately circular shape.

Also, an important observation can be made on the simulation results. For the angle α of 45°, there is a total extinction of the image of a pure screw dislocation for the case considered here. From Eqn.(2.43), it is seen that this is possible either when $\beta = \alpha = 45°$, or when $\lambda_1 = \lambda_2$. How-

ever, $\lambda_1 = \lambda_2$ is an invalid condition here because for other values of α apart from 45° there exists an image as obvious from Figs.3.13a), b), and d). From Eqn.(2.44), it can be seen that β can take a value of 45° only when the denominator vanishes. The stress equations for a pure screw dislocation given in Eqns.(2.21-2.23) indicate that there is no principal stress component associated with them. This coupled with the symmetry properties of π_{ijkl} for cubic crystal ensures that ΔB_{ii} (i=1,2,3) will be zero and hence the denominator in Eqn.(2.44) vanish for this case. The angle β for a pure screw dislocation has a constant value of 45° for this specific case.

Figure 3.14 shows the simulation results for a mixed dislocation on a (100) oriented silicon sample with the dislocation line along the <100> direction and the Burger vector at an angle of 45° to the dislocation line on the (001) plane. This is the case for which the edge and the screw components of the Burger vector are equal in magnitude. Also for this case the sample axes and the crystal principal axes are aligned such that the angle ϕ in Fig.2.10 is zero. The dislocation line is along the sample axis x_3'' and the Burger vector is at an angle of 45° with respect to axis x_1'' on the $x_1''x_3''$ plane. Figures 3.14a), b), c), and d) show the simulation results for α = 0°, 30°, 45°, and 60°, respectively. Since screw dislocations cannot be seen end-on, only the edge dislocation component is present for this case. Hence, Figs.3.12 and 3.14 are similar in nature.

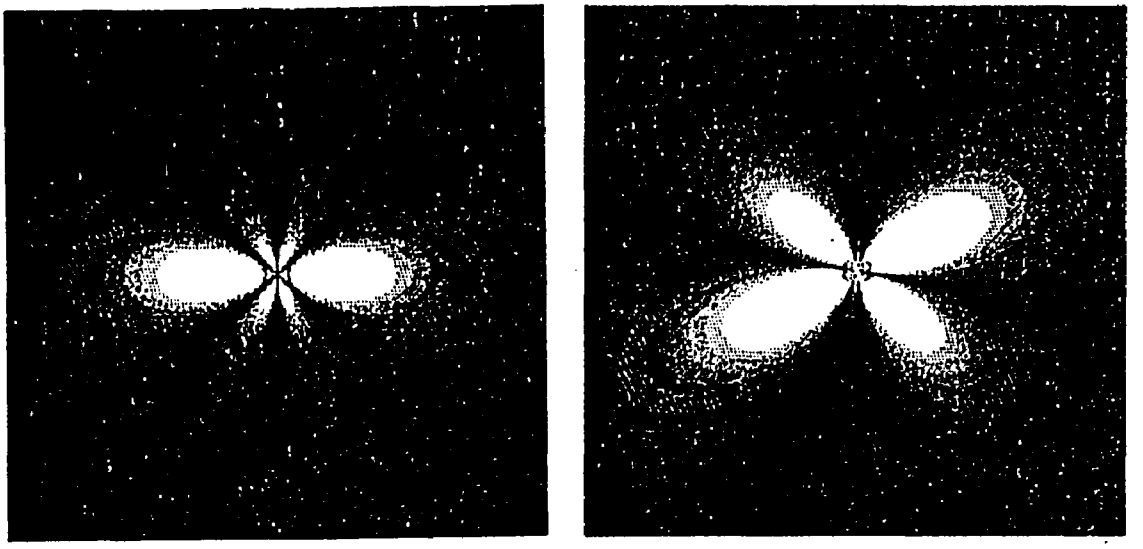

a) $\alpha = 0°$ b) $\alpha = 30°$

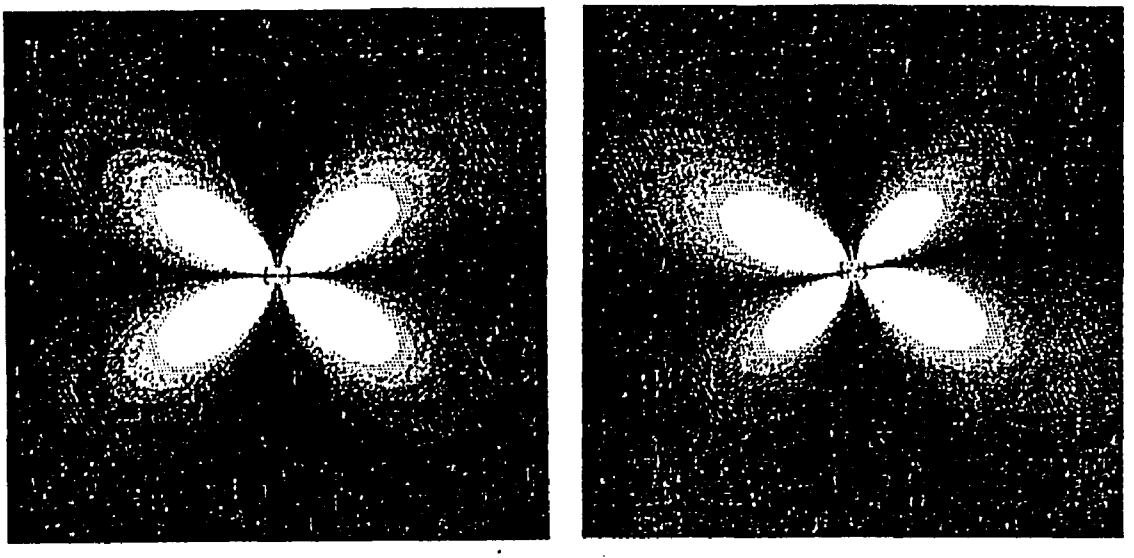

c) $\alpha = 45°$ d) $\alpha = 60°$

Fig.3.14 Simulation results for a mixed dislocation with the dislocation line along the <100> direction and the Burger vector on (001) plane making 45° angle with the dislocation line for a (100) oriented silicon sample.

Figure 3.15 shows the simulation results for a mixed dislocation on a (100) oriented silicon sample with the dislocation line along the <010> direction and the Burger vector at an angle of 45° to the dislocation line on the (001) plane. Figures 3.15a), b), c), and d) show the simulation results for α = 0°, 30°, 45°, and 60°, respectively. From Fig.3.15a), it can be seen that for α = 0°, the screw part of the dislocation shows up prominently. For other polarization angles, the images take on patterns different from the cases shown earlier in Figs.3.12-3.14.

Figure 3.16 shows the simulation results for a mixed dislocation on a (100) oriented silicon sample with the dislocation line along the <110> direction and the Burger vector on the (001) plane at an angle of 45° to the dislocation line. Thus, for this case also, the dislocation has edge and screw components of the Burger vector of equal magnitude. Figures 3.16a), b), c), and d) show the simulation results for polarization angle α = 0°, 30°, 45°, and 60°, respectively. The image patterns in Fig.3.16 are somewhat between a pure edge and a pure screw case. Figure 3.17 shows the simulation results for a mixed dislocation on a (111) oriented silicon sample with the dislocation line along the <110> direction and the Burger vector on the (001) plane at an angle of 60° to the dislocation line. In literature, this dislocation is called a 60° dislocation. Figures 3.17a), b), c), and d) show the simulation results for

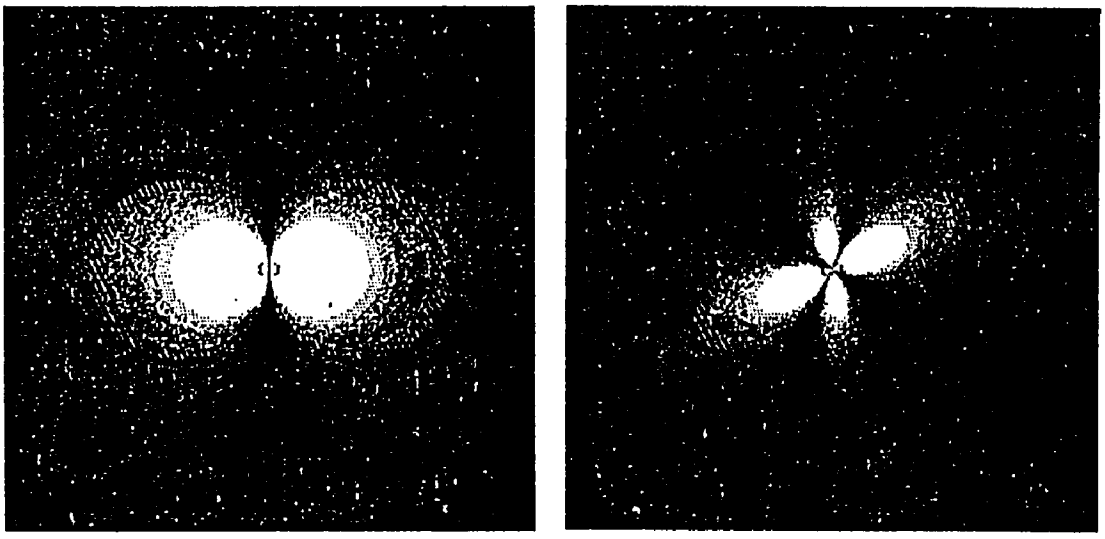

a) $\alpha = 0°$ b) $\alpha = 30°$

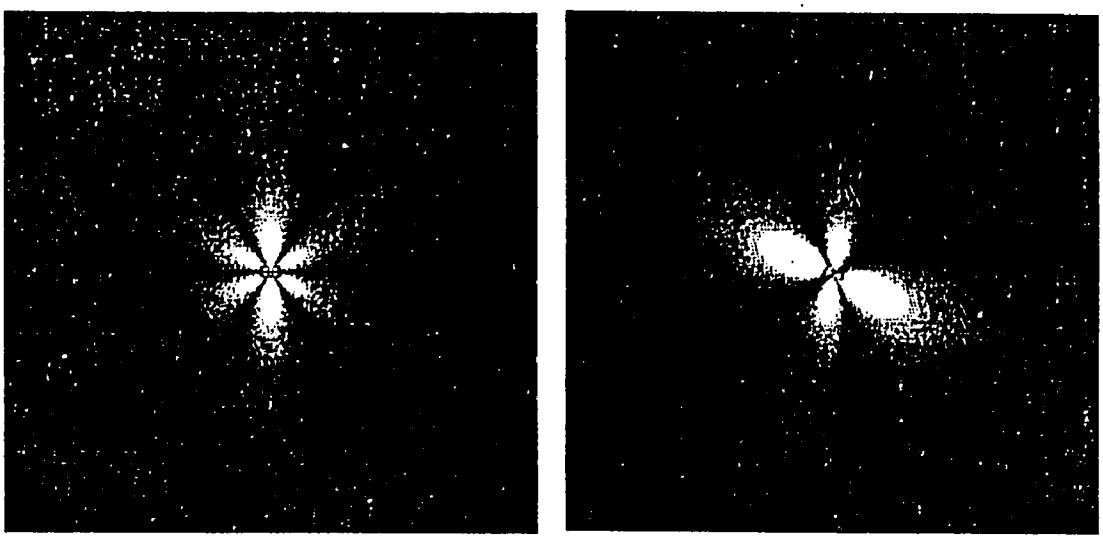

c) $\alpha = 45°$ d) $\alpha = 60°$

Fig.3.15 Simulation results for a mixed dislocation with the dislocation line along the <010> direction and the Burger vector on (001) plane making 45° angle with the dislocation line for a (100) oriented silicon sample.

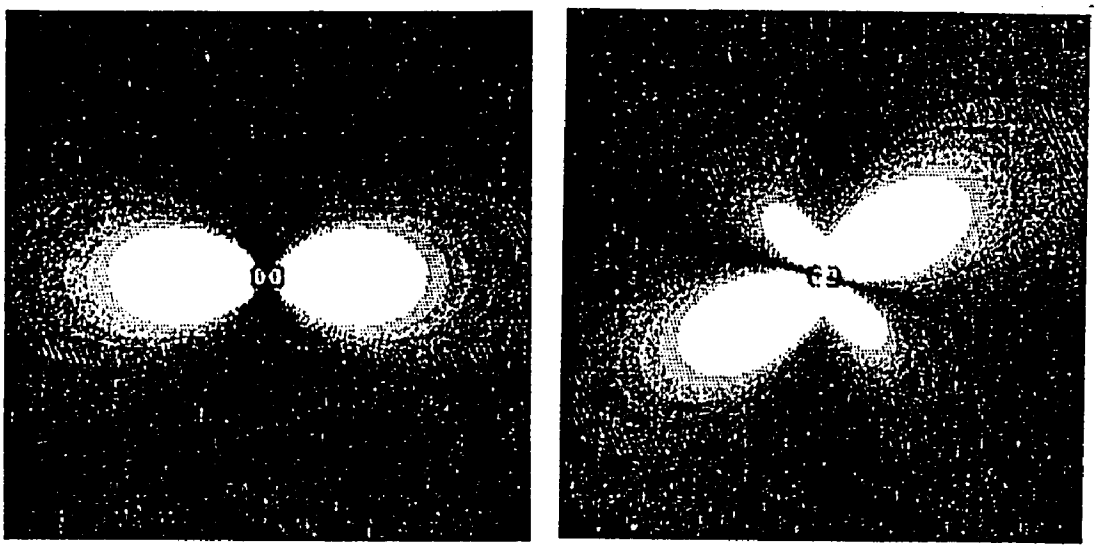

a) α = 0° b) α = 30°

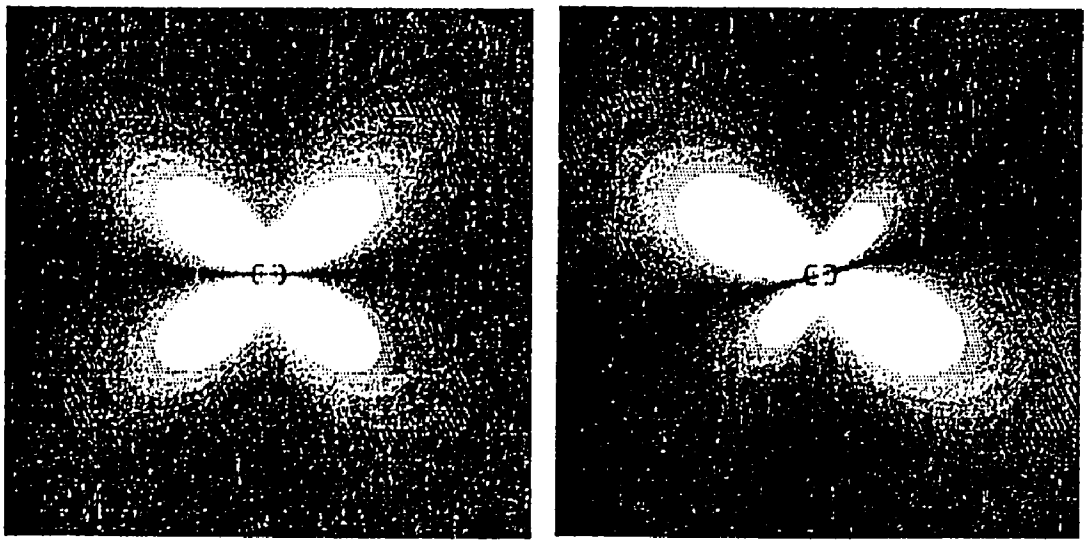

c) α = 45° d) α = 60°

Fig.3.16 Simulation results for a mixed dislocation with the dislocation line along the <110> direction and the Burger vector on (001) plane making an angle of 45° with the dislocation line for a (100) oriented silicon sample.

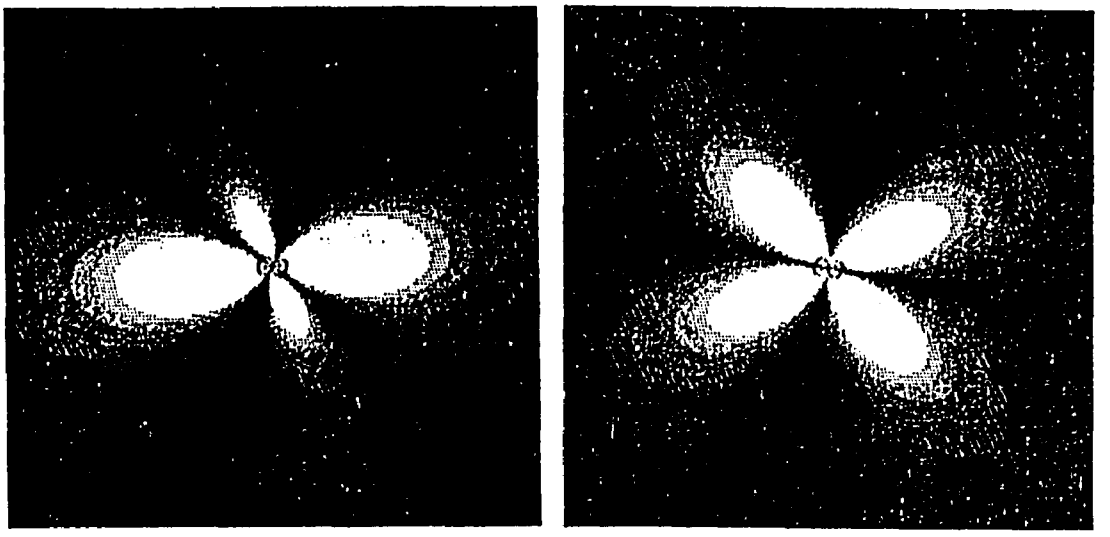

a) $\alpha = 0°$ b) $\alpha = 30°$

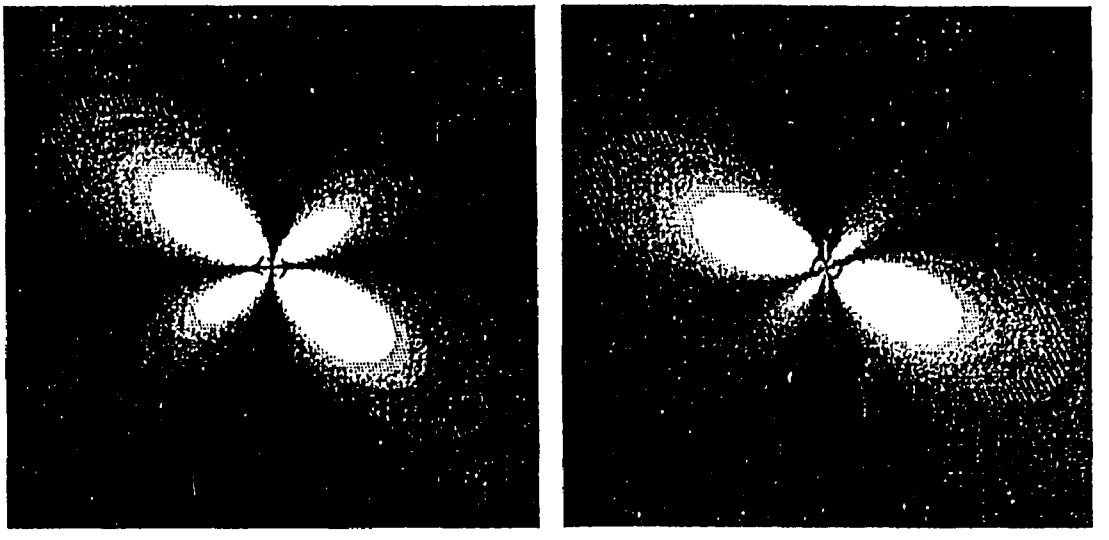

c) $\alpha = 45°$ d) $\alpha = 60°$

Fig.3.17 Simulation results for a mixed dislocation with the dislocation line along the <110> direction and the Burger vector on (001) plane making an angle of 60° with the dislocation line for a (111) oriented silicon sample.

the polarization angle α = 0°, 30°, 45°, and 60°, respectively.

For observation of dislocations, silicon samples were placed on a vertical X-Y stage between the polarizer and the analyzer. The samples investigated were (100) oriented silicon of approximate thickness of 7 mils and were polished on both sides. Figure 3.18 shows the experimentally observed image on a (100) oriented silicon sample. The orientations of the polarizer, the analyzer, and the principal axis [100] are shown in the figure. The images marked A and B in the figure have two-petal rosette patterns and have a good match with the simulated image of a pure screw dislocation with the dislocation line along <010> direction and the Burger vector on (001) plane pointing towards <010> direction as shown in Fig.3.13a). To find out if that was indeed the case, the polarizer and the analyzer pair were rotated by 45° and the resultant image is shown in Fig.3.19. It is seen that both the images disappeared completely which is analogous to the simulation findings as shown in Fig.3.13c). Therefore, based on the data we have, the images marked A and B in Fig.3.18 appear to be pure screw dislocations with the dislocation line along <010> direction and the Burger vector on (001) plane pointing along <010> direction. One bright spot marked C appeared in Fig.3.19 which was absent in Fig.3.18. This defect has not been characterized.

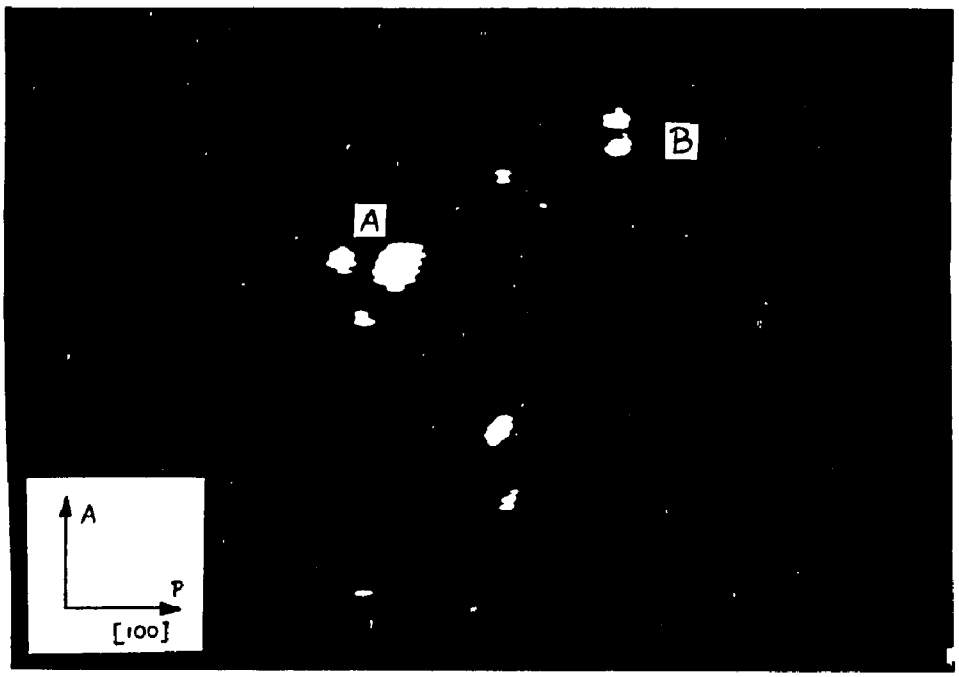

Fig.3.18 Experimentally observed image on (100) oriented silicon sample #8 for the polarization angle of 0°. Magnification x40.

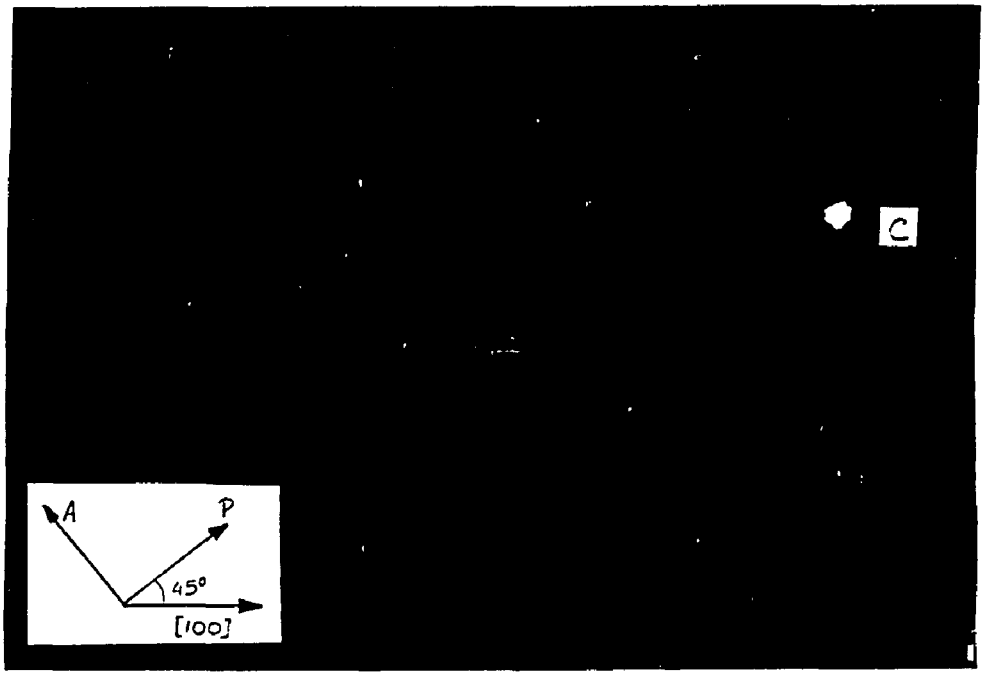

Fig.3.19 Experimentally observed image on (100) oriented silicon sample #8 for the polarization angle of 45°. Magnification x40.

Figure 3.20 shows the experimentally observed image on a (100) oriented silicon sample. The principal axis [100] is shown in the figure. The orientations of the polarizer and the analyzer are also shown in the figure. The image marked A in Fig.3.20 has a rosette pattern consisting of three petals, which resembles the simulated image of a pure edge dislocation with the dislocation line along <100> direction and the Burger vector on (001) plane as shown in Fig.3.12c). Near this image, another image is seen marked B in the figure. Also at the top of the figure, a single bright spot marked C is seen.

In order to observe how the patterns change with a change in the polarization angle α, the polarizer and the analyzer pair was rotated by 45° and the resultant image is shown in Fig.3.21. The three-petal image marked A in Fig.3.20 is transformed to a two-petal rosette pattern as shown marked A in Fig.3.21. The simulated images of a pure edge dislocation as shown in Fig.3.12 bears some similarity with the observed images. Therefore, based on the data we have, the image marked A in Figs.3.20 and 3.21 can be attributed to a pure edge dislocation with the dislocation line along <100> direction and the Burger vector on (001) plane. The images marked B and C in Fig.3.20 retained their patterns in Fig.3.21 and, may be caused by the precipitates on the sample surface. The disappearance of the fourth lobe from the image marked A in Fig.3.20 may have been caused by

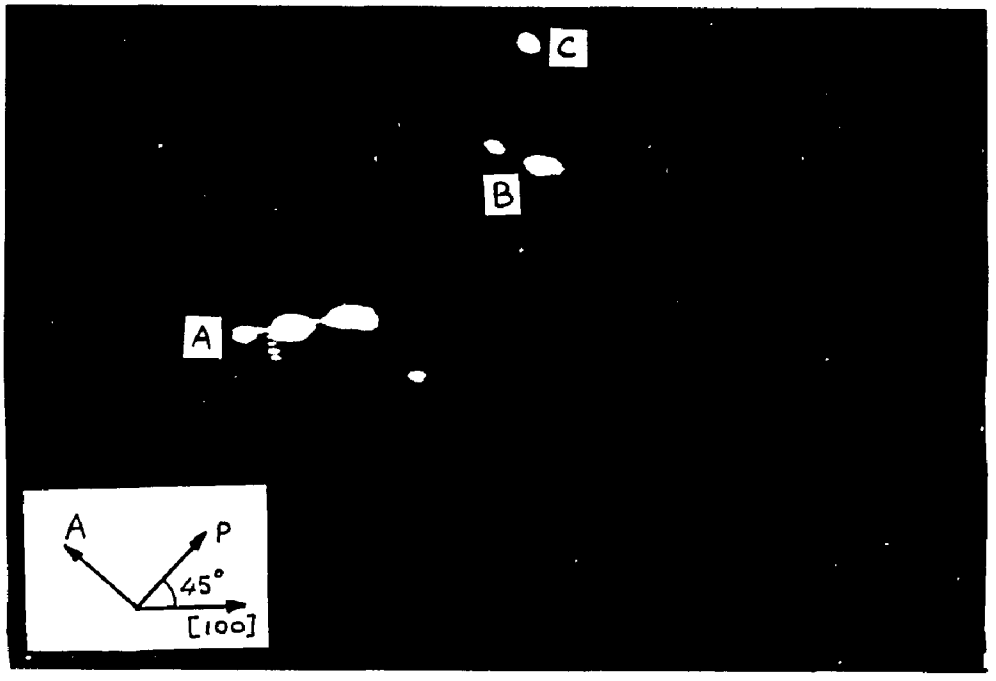

Fig.3.20 Experimentally observed image on (100) oriented silicon sample #5 for the polarization angle of 45°. Magnification ×40.

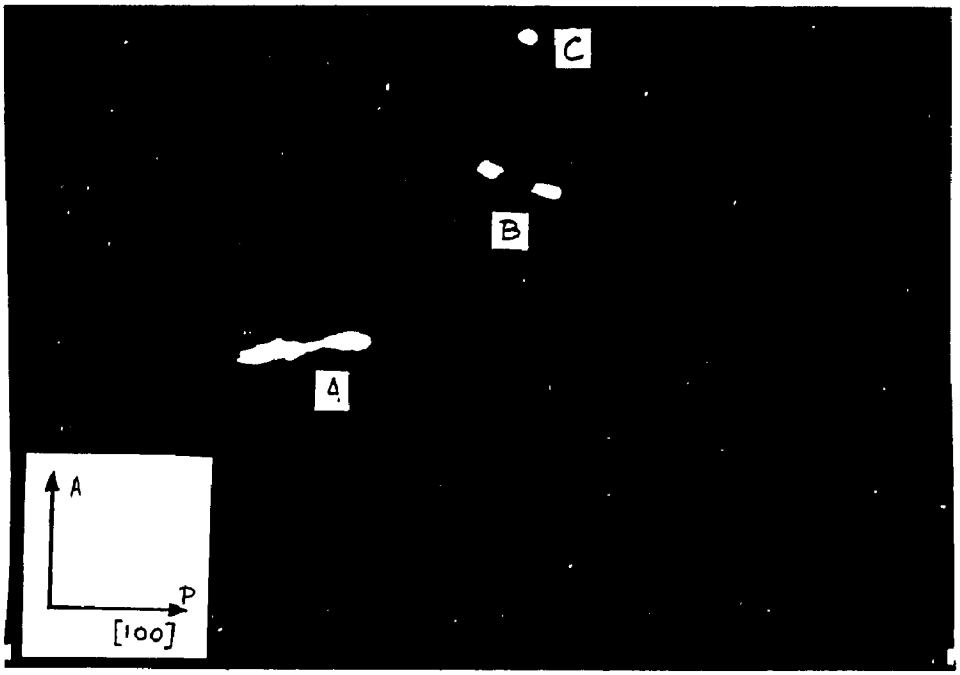

Fig.3.21 Experimentally observed image on (100) oriented silicon sample #5 for the polarization angle of 0°. Magnification ×40.

the internally built-in stress within the sample which interferes with the stress field of the dislocation under consideration.

Figure 3.22 shows the experimentally observed image on a (100) oriented silicon sample. The orientations of the polarizer, the analyzer, and the principal axis [100] are shown in the figure. The image marked A in the figure has a two-petal rosette pattern similar to the simulated image of a pure screw dislocation shown in Fig.3.13a). Around that image, other images with distortion are seen. Figure 3.23 shows the experimentally observed image for the same case but with the polarizer and the analyzer pair rotated by 45°. It is seen from the figure that all the images disappeared completely. Hence, the dislocation marked A in Fig.3.22 appears to be a pure screw dislocation identical to the situation discussed with reference to Figs.3.18 and 3.19. The other dislocation images seen in Fig.3.22 also appear to have strong screw components, though the exact orientations of the dislocation line and the Burger vector could not be characterized due to the distortion in the images.

Some of the experimentally observed images matched well with the simulated images. In principle, a number of simulated images can be stored in a computer for varying directions of the Burger vector with respect to the dislocation line, varying orientations of the dislocation line with

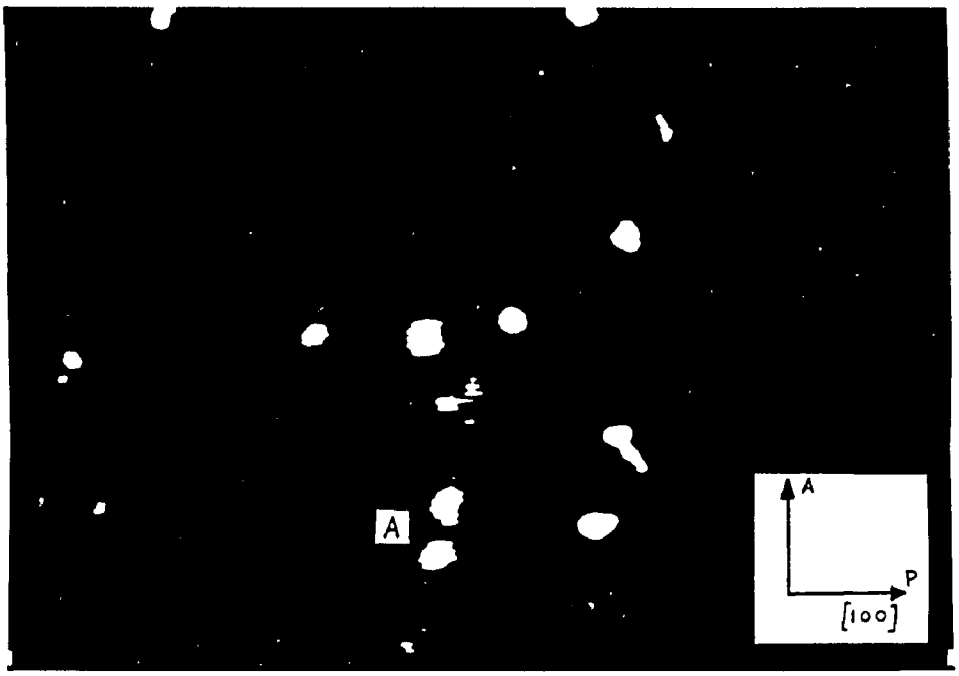

Fig.3.22 Experimentally observed image on (100) oriented silicon sample #6 for the polarization angle of 0°. Magnification ×40.

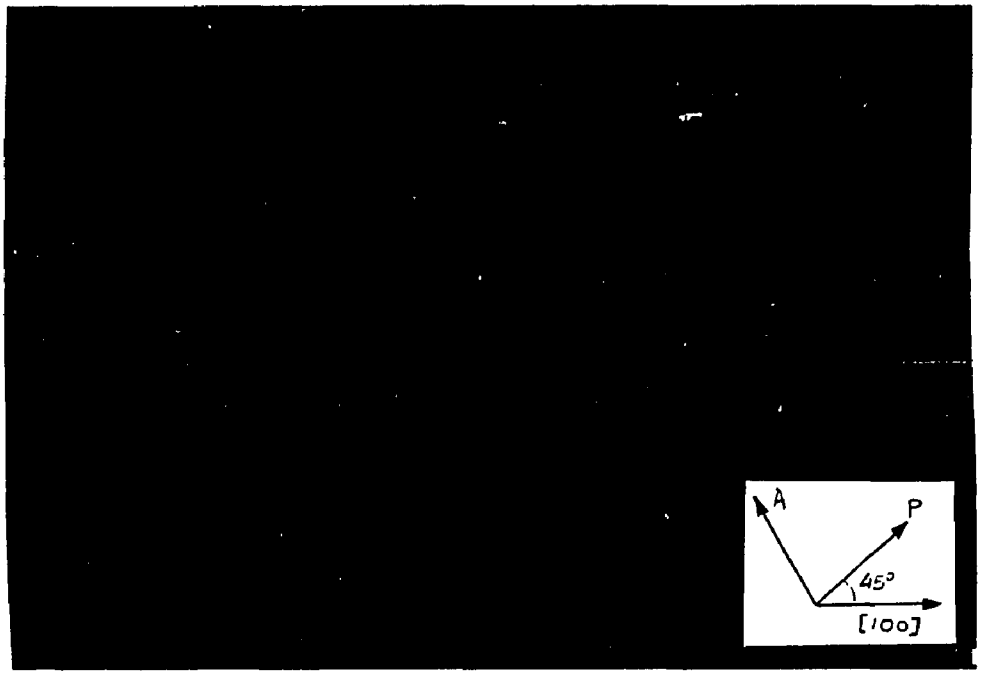

Fig.3.23 Experimentally observed image on (100) oriented silicon sample #6 for the polarization angle of 45°. Magnification ×40.

respect to the sample axes for {100} and {111} oriented samples for a set of values for polarization angle α. A sample with any arbitrary direction of the Burger vector and any arbitrary orientation of the dislocation line can then be placed under the polariscope and the experimental images obtained for different angles of polarization of the incident light. Then an image matching procedure can be utilized to compare the simulated images with the experimentally observed ones to determine the direction of the Burger vector and the orientation of the dislocation line. The match between the analytical images and the experimentally obtained ones provides the information on the dislocations present in the sample.

CHAPTER 4

SUMMARY, CONCLUSIONS AND RECOMMENDATIONS

A fast, accurate, and efficient technique which can characterize large defects in a semiconductor substrate can be useful to improve the yield of the electronic devices fabricated on the substrate. In this work, the technique of infrared piezobirefringence is investigated to characterize large defects in semiconductor materials. A dark field plane polariscope using 1.15 μm wavelength He-Ne infrared laser as the light source was constructed for this purpose.

As a first step towards defect characterization, the cases of diametrically loaded discs of semiconductor samples were considered. The semiconductor discs were placed between crossed polarizer and analyzer of a dark field plane polariscope. A computer algorithm was developed for simulation of the stress patterns and the resulting fringe patterns for these diametrically loaded discs of infrared transparent semiconductor materials. This was done to obtain a better understanding of the simulation algorithm for its subsequent use in line defect identification and characterization. The simulation results matched extremely well with the experimentally obtained images for diametrically compressed discs of Si and GaAs.

The behavior of the stress-optic coefficient C was also investigated in this work, which had been taken as a con-

stant in earlier works by other investigators. The investigation here showed that for {100} oriented Si and GaAs discs under diametrical compression, the value of C changed from one point to the next on the sample surface for a given load. The value of C was also found to depend on the direction of the applied load with respect to the principal crystal axis. However, the value of C for a given position on the wafer did not change upon increasing the magnitude of the load. This is expected from the linearity between the stress and the phase retardation. The values of C for both Si and GaAs discs of {111} orientation were found to be independent of position for any given load, as well as were independent of the orientation of the load with respect to the principal crystal axis, as expected from the crystal symmetry. The values for the stress-optic coefficient C found in this work for {100} oriented Si disc subjected to diametrical compression ranged from 2.0×10^{-12} cm²/dyne to 3.0×10^{-12} cm²/dyne, and for {100} oriented GaAs disc subjected to diametrical compression ranged from 0.8×10^{-12} cm²/dyne to 2.6×10^{-12} cm²/dyne for the cases investigated. For {111} oriented Si and GaAs discs under diametrical compression, the values obtained in this work were 2.33×10^{-12} cm²/dyne and 1.94×10^{-12} cm²/dyne, respectively.

Next, the above algorithm was modified and used to determine the fringe patterns for line dislocations. Some interesting observations were noted based on the image simulation

results. First, in agreement with previous authors, it was found that pure screw dislocations could not be viewed end-on, i.e., along the dislocation line. Also, for a {100} oriented silicon sample, it was found that the patterns of the images for a pure edge dislocation viewed end-on and a pure screw dislocation viewed perpendicular to the dislocation line had significant differences when the dislocation lines were oriented along principal crystal directions [100], providing an easy distinguishing feature between the two cases. Also, for the above two cases, when the angle of polarization α was equal to 45°, the image was the brightest with a four-petal rosette pattern with equal lobes for the pure edge dislocation case but was extinct for the pure screw dislocation case.

A variety of these images can be stored in a computer for varying directions of the Burger vector and varying orientations of the dislocation line for {100} and {111} oriented samples for different angles of polarization of the incident light. Then a sample can be placed under the polariscope and the experimental images obtained for varying angles of polarization of the incident light. An image matching procedure can then be used to specify the type of the dislocation, its position, and the direction of its Burger vector. In this work, a few cases of dislocations were investigated. Images corresponding to a pure edge dislocation and a pure screw dislocation among others were identified on (100) ori-

ented silicon samples by comparing the experimentally obtained images with the simulated ones.

A computer algorithm can be developed in future which can compare the experimentally obtained images of dislocations with the simulated ones for automated matching of the two. This can reduce the defect characterization time significantly. Also, the technique can be utilized to automatically test each wafer for dislocations rather than carrying out statistical batch analysis as is done currently. The technique can also be employed for process diagnostics in the IC manufacturing industries.

Though only semiconductor materials were investigated in this work, this method is in no way restricted only to them. Any photoelastic material which is isotropic when unstressed and becomes birefringent when stressed can be tested for defects using this method. However, the absorption cutoff of the material must be known so that the laser can be tuned to a wavelength longer than the cutoff wavelength.

Work on this field can be extended to interface stresses and their characterization. In particular, the stress caused by heterostructures with mismatching lattice parameters can be characterized by this method. A model needs to be developed which can simulate the stress patterns caused by these structures which can then be utilized with modifications in the program developed here to simulate the interference patterns produced by these stresses.

REFERENCES

1. Kane, P. F. and G. B. Larrabee; "Characterization of Semiconductor Materials"; McGraw-Hill, New York, 1970.

2. Tanner, B. K.; "X-Ray Diffraction Topography"; Pergamon Press, Oxford, 1976.

3. Eshelby, J. D.; "Edge Dislocations in Anisotropic Materials"; Philosophical Magazine; Vol. 40, No. 308, 1949, pp. 903-912.

4. Read, W. T., Jr.; "Dislocations in Crystals"; McGraw-Hill, New York, 1953.

5. Eshelby, J. D., W. T. Read, and W. Shockley; "Anisotropic Elasticity with Applications to Dislocation Theory"; Acta Metallurgica; Vol. 1, No. 3, 1953, pp. 251-259.

6. Spence, G. B.; "Theory of Extended Dislocations in Symmetry Directions in Anisotropic Infinite Crystals and Thin Plates"; Journal of Applied Physics; Vol. 33, No. 2, 1962, pp. 729-733.

7. Chou, Y. T.; "Interaction of Parallel Dislocations in a Hexagonal Crystal"; Journal of Applied Physics; Vol. 33, No. 9, 1962, pp. 2747-2751.

8. Chou, Y. T.; "Characteristics of Dislocation Stress Fields Due to Elastic Anisotropy"; Journal of Applied Physics; Vol. 34, No. 2, 1963, pp. 429-433.

9. Weertman, J. and J. R. Weertman; "Elementary Dislocation Theory"; Macmillan, New York, 1964.

10. Hirth, J. P. and J. Lothe; "Theory of Dislocations"; McGraw-Hill, New York, 1968.

11. DeNicola, R. O. and R. N. Tauber; "Effect of Growth Parameters on the Residual Stress and Dislocation Density of Czochralski-Grown Silicon Crystals"; Journal of Applied Physics; Vol. 42, No. 11, 1971, pp. 4262-4270.

12. Briggs, H. B.; "Optical Effects in Bulk Silicon and Germanium"; Physical Review; Vol. 77, 1950, p. 287.

13. Poindexter, E.; "Piezobirefringence in Diamond"; The American Mineralogist; Vol. 40, 1955, pp. 1032-1054.

14. Giardini, A. A.; "Piezobirefringence in Silicon"; The American Mineralogist; Vol. 43, 1958, pp. 249-262.

15. Hornstra, J. and P. Penning; "Birefringence Due to Residual Stress in Silicon"; Philips Research Reports; Vol. 14, 1959, pp. 237-249.

16. Prussin, S. and A. Stevenson; "Strain-Optic Coefficient of Silicon for Infrared Light"; Journal of Applied Physics; Vol. 30, 1959, pp. 452-453.

17. Lederhandler, S. R.; "Infrared Studies of Birefringence in Silicon"; Journal of Applied Physics; Vol. 30, No. 11, 1959, pp. 1631-1638.

18. Schimdt-Tiedemann, K. J.; "Stress Optical Constants of Germanium"; Journal of Applied Physics; Vol. 22, 1961, pp. 2058-2059.

19. Nikitenko, V. I. and G P. Martynenko; "Certain Photoelastic Properties of Gallium Arsenide and Silicon"; Soviet Physics - Solid State; Vol. 7, No. 2, 1965, pp. 494-496.

20. Appel, A. V., H. T. Betz, and D. A. Pontarelli; "Infrared Polariscope for Photoelastic Measurement of Semiconductors"; Applied Optics; Vol. 4, No. 11, 1965, pp. 1475-1478.

21. Carron, G. J. and L. K. Walford; "Comparison of X-Ray Topography and Infrared Birefringence for Investigating Thermal Stresses in Silicon"; Journal of Applied Physics; Vol. 38, No. 10, 1967, pp. 3949-3958.

22. Bond, W. L. and J. Andrus; "Photographs of the Stress Field around Edge Dislocations"; Physical Review; Vol. 101, 1956, p. 1211.

23. Fathers, D. J. and B. K. Tanner; "Line Defects in Barium Titanate Observed by Polarized Light Microscopy"; Philosophical Magazine; Vol. 28, 1973, pp. 749-770.

24. Chuan-Zhen, G., M. Nai-Ben, and F. Duan; "A Study of Screw Dislocations in Gadolinium Gallium Garnet and Yttrium Aluminium Garnet Crystals by Birefringence Topography"; Philosophical Magazine A; Vol. 53, No. 2, 1986, pp. 285-296.

25. Bullough, R.; "Birefringence Caused by Edge Dislocations in Silicon"; Physical Review; Vol. 110, No. 3, 1958, pp. 620-623.

26. Indenbom, V. L. and G. E. Tomilovskii; "Microstructure of Stresses in Lines of Slip and Dislocations"; Soviet Physics - Doklady; Vol. 3, No. 6, 1958, pp. 1097-1101.

27. Prescott, M. J. and J. Basterfield; "The Observation of Dislocations in Yttrium Gallium Garnet by a Photoelastic Method"; Journal of Materials Science; Vol. 2, 1967, pp. 583-588.

28. Matthews, J. W., T. S. Plaskett, and S. E. Blum; "Optical Birefringence Images of Dislocations in Large Gallium Phosphide Crystals"; Journal of Crystal Growth; Vol. 42, 1977, pp. 621-624.

29. Indenbom, V. L., V. I. Nikitenko, and L. S. Milevskii; "Analysis of Dislocation Structure in Crystals with Polarized Light"; Soviet Physics - Solid State; Vol. 4, No. 1, 1962, pp. 162-166.

30. Indenbom, V. L., V. I. Nikitenko, and L. S. Milevskii; "The Observation of Internal Stresses Surrounding Dislocations in Silicon"; Soviet Physics - Doklady; Vol. 6, No. 12, 1962, pp. 1034-1036.

31. Jenkins, D. A. and J. J. Hern; "Quantitative Piezobirefringence Studies of Dislocations in Transparent Crystals"; Philosophical Magazine; Vol. 33, No. 1, 1976, pp. 173-180.

32. Jenkins, D. A., T. S. Plaskett, and P. Chaudhuri; "Birefringence Images of Arbitrarily Oriented Dislocation Lines in (111) Silicon Wafers"; Philosophical Magazine; Vol. 39, No. 2, 1979, pp. 237-243.

33. Nikitenko, V. I. and L. M. Dedukh; "Application of the Photoelasticity Method to the Investigation of Stresses around Individual Dislocations and their Influence on Crystal Properties"; Physica Status Solidi (A); Vol. 3, 1970, pp. 383-392.

34. Tanner, B. K. and D. J. Fathers; "Contrast of Crystal Defects under Polarized Light"; Philosophical Magazine; Vol. 29, 1974, pp. 1081-1094.

35. Indenbom, V. L. and G. E. Tomilovskii; "Macroscopic Edge Dislocations in a Corundum Crystal"; Soviet Physics - Crystallography; Vol. 2, No. 1, 1957, pp. 183-187.

36. Matthews, J. W., T. S. Plaskett, and J. Ahn; "Observation of Dislocations in Large Crystals of Gadolinium Gallium Garnet"; Philosophical Magazine; Vol. 33, No. 1, 1976, pp. 73-85.

37. Matthews, J. W. and T. S. Plaskett; "Optical Birefringence Images of Edge Dislocations"; Physica Status Solidi (A); Vol. 37, 1976, pp. 499-503.

38. Matthews, J. W. and T. S. Plaskett; "Formation of Large Climb Loops at Decorated Dislocations in Gadolinium Gallium Garnet"; Physica Status Solidi (A); Vol. 38, 1976, pp. 577-585.

39. Matthews, J. W. and T. S. Plaskett; "Dislocations in Neodymium Gallium Garnet ($Nd_3Ga_5O_{12}$ or NdGG)"; Journal of Materials Science; Vol. 13, 1978, pp. 2029-2036.

40. Haydar, A. and R. Labusch; "Birefringence and Structural Defects in Cu_2O Crystals"; Journal of Applied Physics; Vol. 54, No. 5, 1983, pp. 2605-2610.

41. Xu, X. Y. and D. Feng; "Observation of Dislocations and Subboundaries in the Optically Active Crystal $Bi_{12}GeO_{20}$ with Reflection Birefringence Topography"; Journal of Materials Science; Vol. 20, 1985, pp. 612-619.

42. Hilgarth, J.; "Direct Observation of Dislocations in GaP Crystals"; Journal of Materials Science; Vol. 13, 1978, pp. 2697-2702.

43. Loschke, K. and P. Paufler; "On the Stress-Induced Birefringence Images of Edge Dislocations Viewed from the Side in GaP Single Crystals"; Philosophical Magazine A; Vol. 46, No. 4, 1982, pp. 699-705.

44. Paufler, P. and K. Loschke; "On the Visibility of Dislocations Perpendicular to the Optic Axis by Stress-Induced Birefringence in Elastically and Optically Isotropic Materials"; Philosophical Magazine A; Vol. 47, No. 1, 1983, pp. 79-91.

45. Ahearn, J. S., Jr., C. A. B. Ball, and C. Laird; "Stress-Induced Birefringence of Mismatching III-V Heterojunctions"; Physica Status Solidi (A); Vol. 38, 1976, pp. 315-320.

46. Bartels, W. J. and W. Nijman; "Asymmetry of Misfit Dislocations in Heteroepitaxial Layers on (001) GaAs Substrates"; Journal of Crystal Growth; Vol. 37, 1977, pp. 204-214.

47. Booyens, H. and J. H. Basson; "The Application of Elastobirefringence to the Study of Strain Fields and Dislocations in III-V Compounds"; Journal of Applied Physics; Vol. 51, No. 8, 1980, pp. 4368-4374.

48. Booyens, H. and J. H. Basson; "The Analysis of Dislocations in Strained III-V Semiconductor Crystals Using Elastobirefringence"; Journal of Applied Physics; Vol. 51, No. 8, 1980, pp. 4375-4378.

49. Booyens, H., J. H. Basson, and M. B. Small; "The Behavior of Dislocations in GaAs Substrates During the Growth of $Ga_xAl_{1-x}As$ Epitaxial Layers"; Journal of Applied Physics; Vol. 52, No. 6, 1981, pp. 4112-4114.

50. Booyens, H., G. R. Proto, and J. H. Basson; "Strain Effects Associated with SiO Layers Evaporated into GaAs"; Journal of Applied Physics; Vol. 54, No. 10, 1983, pp. 5779-5784.

51. Frocht, M. M.; "Photoelasticity"; John Wiley & Sons, New York, 1941.

52. Nye, J. F.; "Physical Properties of Crystals"; Clarendon Press, Oxford, 1957.

53. Frank, F. C.; "Crystal Dislocations - Elementary Concepts and Definitions"; Philosophical Magazine; Vol. 42, No. 331, 1951, pp. 809-819.

54. Ajmera, P. K., B. Huner, A. K. Dutta, and C. S. Hartley; "Simulation and Observation of Infrared Piezobirefringent Images in Diametrically Compressed Semiconductor Disks"; Applied Optics; Vol. 27, No. 4, 1988, pp. 752-757.

55. Dutta, A. K., P. K. Ajmera, and B. Huner; "Piezobirefringence Effect in GaAs Disks Subjected to Diametrical Compression"; Journal of Applied Physics; Vol. 65, No. 12, 1989, pp. 5230-5232.

APPENDICES

A. Calculation of the Direction Cosines between the Sample Axes and the Crystal Principal Axes for a {100} Oriented Sample under any Arbitrary Direction of Loading

Figure A.1 shows the axes system chosen. The loading axes system and the crystal principal axes system are denoted by (x_1'', x_2'', x_3'') and (x_1', x_2', x_3'), respectively. Axis x_3'' in the loading axes system and axis x_1' in the crystal principal axes system are aligned and come out of the plane of the paper. The crystal principal axis x_2' makes an angle ϕ with axis x_1'' of the loading axes system. The load P is applied along axis x_2''. The coordinates being so defined, the direction cosines can now be obtained. These are given by:

$$
\begin{aligned}
a_{11}' &= \cos x_1' \hat{} x_1'' = \cos 90^\circ = 0 , \\
a_{12}' &= \cos x_1' \hat{} x_2'' = \cos 90^\circ = 0 , \\
a_{13}' &= \cos x_1' \hat{} x_3'' = \cos 0^\circ = 1 , \\
a_{21}' &= \cos x_2' \hat{} x_1'' = \cos \phi , \\
a_{22}' &= \cos x_2' \hat{} x_2'' = \cos(90^\circ - \phi) , \\
a_{23}' &= \cos x_2' \hat{} x_3'' = \cos 90^\circ = 0 , \\
a_{31}' &= \cos x_3' \hat{} x_1'' = \cos(90^\circ + \phi) , \\
a_{32}' &= \cos x_3' \hat{} x_2'' = \cos \phi , \\
a_{33}' &= \cos x_3' \hat{} x_3'' = \cos 90^\circ = 0 .
\end{aligned}
\qquad (A.1)
$$

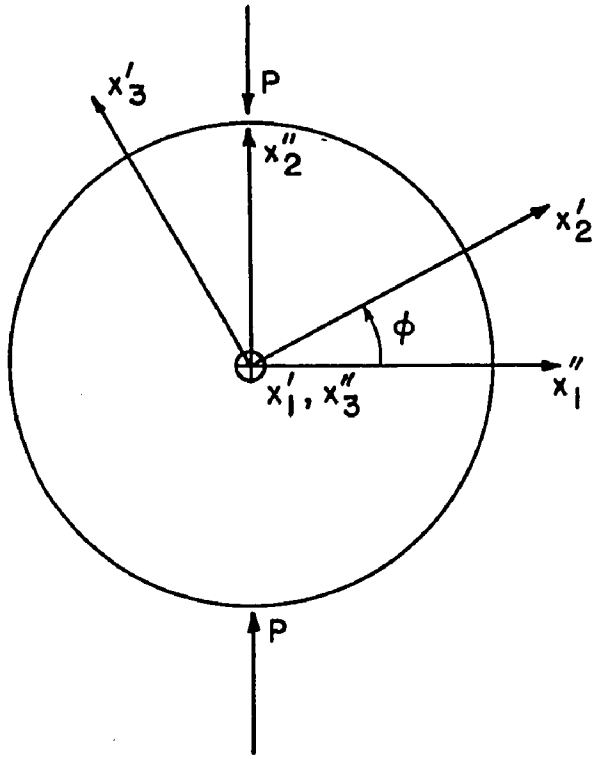

Fig.A.1 The loading and the crystal principal axes systems for a {100} oriented plane.

B. Calculation of the Direction Cosines between the Sample Axes and the Crystal Principal Axes for a {111} Oriented Sample under any Arbitrary Direction of Loading

The calculation of the direction cosines between the sample axes and the crystal principal axes for {111} oriented samples is more involved. Here, (x_1'', x_2'', x_3'') coordinate system refers to the loading axes system with x_2'' being the axis of loading. Axis x_1'' lies on the sample surface while axis x_3'' is normal to the plane of the paper as shown in Fig.B.1. Also, (x_1', x_2', x_3') refers to the crystal principal axes coordinate system as shown in Fig.B.2. The origin of both these coordinate systems is taken to be the substrate center O.

Let (x_1'', x_2'', x_3'') be the point on the wafer periphery where the load is applied. This arbitrary loading direction can be specified by an angle γ measured in the clockwise direction from axis x_2 as shown in Fig.B.3a). The latter is the projection of crystal principal axis x_1' on the wafer plane as indicated in Fig.B.3b). Axes x_3 and x_3'' are the same axis normal to the plane of the paper. Axis x_1 is in the plane of the wafer and is perpendicular to both x_2 and x_3. One needs to determine the direction cosines a_{ij}' that relate a point (x_1'', x_2'', x_3'') in the loading axes system to a point (x_1', x_2', x_3') in the crystal axes system. The transformation equation is given as:

$$x_i' = \sum_j a_{ij}' x_j'' \quad (j=1,2,3) \ . \tag{B.1}$$

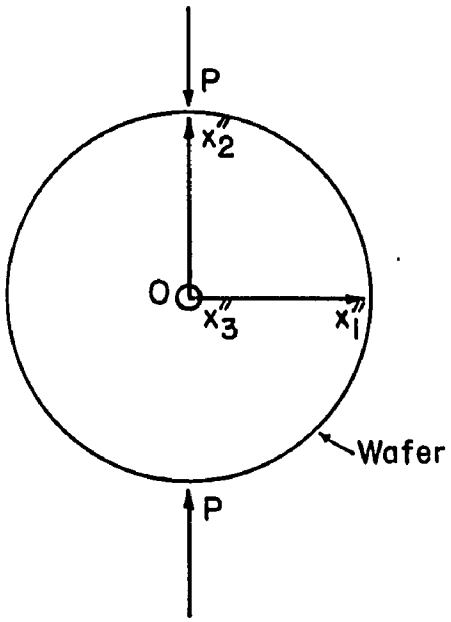

Fig.B.1 The loading axes coordinate system.

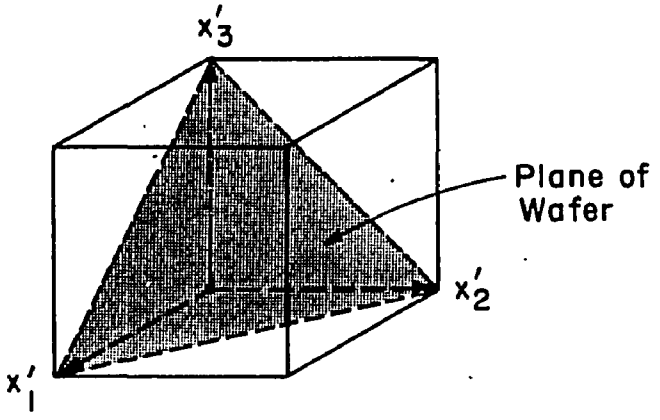

Fig.B.2 The crystal axes system and its orientation with respect to the plane of the wafer.

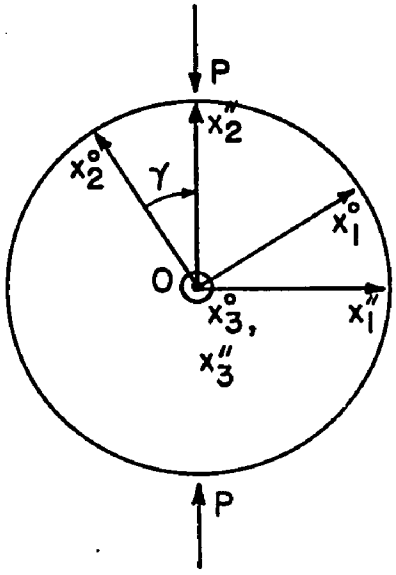

a) Top view

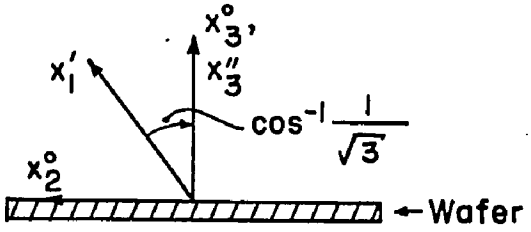

b) Side view

Fig.B.3 The $(x_1^\S, x_2^\S, x_3^\S)$ coordinate system and its relationship to the loading axes system and the crystal principal axes system.

This linear transformation is carried out in two steps as given below:

$$x_k^{\circ} = \sum_j a_{kj} x_j'' \quad (j=1,2,3) ,$$

and

$$x_i' = \sum_k a_{ik}'' x_k^{\circ} \quad (k=1,2,3) ,$$

or

$$x_i' = \sum_k a_{ik}'' \left(\sum_j a_{kj} x_j''\right) \quad (j,k=1,2,3) . \qquad (B.2)$$

Comparing Eqns.(B.1) and (B.2), one gets:

$$a_{ij}' = \sum_k a_{ik}'' a_{kj} \quad (k=1,2,3) . \qquad (B.3)$$

From Fig.B.3, one obtains by direct observation that:

$$\begin{aligned}
a_{11}^{\circ} &= \cos(x_1^{\circ} \hat{} x_1'') = \cos\gamma , \\
a_{12}^{\circ} &= \cos(x_1^{\circ} \hat{} x_2'') = \cos(90^{\circ}-\gamma) , \\
a_{13}^{\circ} &= \cos(x_1^{\circ} \hat{} x_3'') = 0 , \\
a_{21}^{\circ} &= \cos(x_2^{\circ} \hat{} x_1'') = \cos(90^{\circ}+\gamma) , \\
a_{22}^{\circ} &= \cos(x_2^{\circ} \hat{} x_2'') = \cos\gamma , \\
a_{23}^{\circ} &= \cos(x_2^{\circ} \hat{} x_3'') = 0 , \\
a_{31}^{\circ} &= \cos(x_3^{\circ} \hat{} x_1'') = 0 , \\
a_{32}^{\circ} &= \cos(x_3^{\circ} \hat{} x_2'') = 0 , \\
a_{33}^{\circ} &= \cos(x_3^{\circ} \hat{} x_3'') = 1 . \qquad (B.4)
\end{aligned}$$

In the crystal axes system, from Fig.B.2, one can write the unit vector $\hat{x_2}^{\circ}$ along the axis x_2° as:

$$\hat{x_2}^{\circ} = (2/\sqrt{6})\hat{x_1}' - (1/\sqrt{6})\hat{x_2}' - (1/\sqrt{6})\hat{x_3}' , \qquad (B.5)$$

where x_1', x_2', x_3' are unit vectors along the three crystal principal axes. This is obtained by considering the intercept of the {111} crystal plane on x_1' axis as (a,0,0) and then by translating the origin by (a/3,a/3,a/3) to the substrate center to give the point coordinates as (2a/3,-a/3,-a/3). Here, a is the crystal lattice constant. The unit vector pointing from the origin (0,0,0) to this point is given by Eqn.(B.5). The unit vector x_3° along the direction perpendicular to the {111} plane is given from analytical geometry as:

$$x_3^{\circ} = (1/\sqrt{3})x_1' + (1/\sqrt{3})x_2' + (1/\sqrt{3})x_3' \ . \qquad (B.6)$$

The unit vector $x_1^{\circ} = x_2^{\circ} \times x_3^{\circ}$ and is given by:

$$x_1^{\circ} = -(1/\sqrt{2})x_2' + (1/\sqrt{2})x_3' \ . \qquad (B.7)$$

Use of Eqns.(B.5-B.7) gives:

$$\begin{aligned}
a''_{11} &= \cos(x_1' \hat{} x_1^{\circ}) = 0 \ , \\
a''_{12} &= \cos(x_1' \hat{} x_2^{\circ}) = \cos(35.264^{\circ}) = 2/\sqrt{6} \ , \\
a''_{13} &= \cos(x_1' \hat{} x_3^{\circ}) = \cos(54.736^{\circ}) = 1/\sqrt{3} \ , \\
a''_{21} &= \cos(x_2' \hat{} x_1^{\circ}) = \cos(135^{\circ}) = -1/\sqrt{2} \ , \\
a''_{22} &= \cos(x_2' \hat{} x_2^{\circ}) = \cos(114.095^{\circ}) = -1/\sqrt{6} \ , \\
a''_{23} &= \cos(x_2' \hat{} x_3^{\circ}) = \cos(54.736^{\circ}) = 1/\sqrt{3} \ , \\
a''_{31} &= \cos(x_3' \hat{} x_1^{\circ}) = \cos(45^{\circ}) = 1/\sqrt{2} \ , \\
a''_{32} &= \cos(x_3' \hat{} x_2^{\circ}) = \cos(114.095^{\circ}) = -1/\sqrt{6} \ , \\
a''_{33} &= \cos(x_3' \hat{} x_3^{\circ}) = \cos(54.736^{\circ}) = 1/\sqrt{3} \ . \qquad (B.8)
\end{aligned}$$

Using Eqns.(B.4) and (B.8), one can get the direction cosines a'_{ij} from Eqn.(B.3). These are given by:

$$
\begin{aligned}
a'_{11} &= (2/\sqrt{6})\cos(90^\circ+\gamma) \ , \\
a'_{12} &= (2/\sqrt{6})\cos\gamma \ , \\
a'_{13} &= 1/\sqrt{3} \ , \\
a'_{21} &= -(1/\sqrt{2})\cos\gamma - (1/\sqrt{6})\cos(90^\circ+\gamma) \ , \\
a'_{22} &= -(1/\sqrt{2})\cos(90^\circ-\gamma) - (1/\sqrt{6})\cos\gamma \ , \\
a'_{23} &= 1/\sqrt{3} \ , \\
a'_{31} &= (1/\sqrt{2})\cos\gamma - (1/\sqrt{6})\cos(90^\circ+\gamma) \ , \\
a'_{32} &= (1/\sqrt{2})\cos(90^\circ-\gamma) - (1/\sqrt{6})\cos\gamma \ , \\
a'_{33} &= 1/\sqrt{3} \ . \qquad \text{(B.9)}
\end{aligned}
$$

For the special case when the loading axis x''_2 coincides with the axis x'_2, $\gamma = 0$ and the direction cosines are given by Eqn.(B.8). For any other value of γ, the direction cosines are given by Eqn.(B.9).

C. Derivation of the Piezooptic Coefficients for Gallium Arsenide from the Elastooptic Coefficients and the Stiffness Constants

In this section, the piezooptic coefficients for GaAs are derived from the elastooptic coefficients and the stiffness constants. The notations used by Nye [52] are followed. The compliance is denoted by s, the stiffness by c, the elastooptic coefficients by p, and the piezooptic coefficients by π. All of these parameters are fourth-rank tensors with each of them having a total of possible 81 terms. The generalized form of Hooke's law can be written as:

$$\epsilon_{ij} = \sum_{k,l} s_{ijkl}\sigma_{kl} \quad (k,l=1,2,3) \ , \tag{C.1}$$

where k and l are summation indices, the ϵ_{ij} denotes strain, the σ_{kl} denotes stress, and the s_{ijkl} denotes crystal compliance. Equation (C.1) can also be written in an alternate form as:

$$\sigma_{ij} = \sum_{k,l} c_{ijkl}\epsilon_{kl} \quad (k,l=1,2,3) \ , \tag{C.2}$$

where c_{ijkl} are the stiffness constants of the crystal. For both s_{ijkl} and c_{ijkl}, the following relations are true:

$$s_{ijkl} = s_{ijlk} = s_{jikl} = s_{jilk} \ ,$$

and

$$c_{ijkl} = c_{ijlk} = c_{jikl} = c_{jilk} \ . \tag{C.3}$$

Using the reduced notation of Nye as given in Table 2.1 on page 24, Eqns.(C.1) and (C.2) can be written as:

$$\epsilon_i = \sum_j s_{ij}\sigma_j \quad (i,j=1,2,\ldots,6) \ ,$$

and

$$\sigma_i = \sum_j c_{ij}\epsilon_j \quad (i,j=1,2,\ldots,6) \ . \qquad (C.4)$$

However, changing the notation from tensor to matrix introduces factors of 2 and 4 as follows. For the compliances:

$$\begin{aligned} s_{ijkl} &= s_{mn} \text{ when m and n are 1, 2, or 3 ,} \\ 2s_{ijkl} &= s_{mn} \text{ when either m or n are 4, 5, or 6 ,} \\ 4s_{ijkl} &= s_{mn} \text{ when both m and n are 4, 5, or 6 .} \end{aligned} \qquad (C.5)$$

For the stiffness, no factors of 2 or 4 are necessary, however. It can simply be written as:

$$c_{ijkl} = c_{mn} \quad (i,j,k,l=1,2,3,\ m,n=1,2,\ldots,6) \ . \qquad (C.6)$$

The total maximum possible number of non-equal elements after taking into account the identities (C.3) is 36. However, as the crystal possesses more and more symmetry elements, the number of non-equal parameters reduces. For the cubic crystals, this number becomes only three with the matrix elements given by:

$$\begin{bmatrix} x_{11} & x_{12} & x_{12} & 0 & 0 & 0 \\ x_{12} & x_{11} & x_{12} & 0 & 0 & 0 \\ x_{12} & x_{12} & x_{11} & 0 & 0 & 0 \\ 0 & 0 & 0 & x_{44} & 0 & 0 \\ 0 & 0 & 0 & 0 & x_{44} & 0 \\ 0 & 0 & 0 & 0 & 0 & x_{44} \end{bmatrix} \qquad (C.7)$$

where x can stand for c, s, p, or π.

For cubic systems, s_{11}, s_{12}, s_{44} and c_{11}, c_{12}, c_{44}, are related by [52]:

$$\frac{s_{11} + s_{12}}{(s_{11} - s_{12})(s_{11} + 2s_{12})} = c_{11} ,$$

$$\frac{- s_{12}}{(s_{11} - s_{12})(s_{11} + 2s_{12})} = c_{12} ,$$

and

$$s_{44} = \frac{1}{c_{44}} . \qquad (C.8)$$

Solving the above equations for s_{11} and s_{12}, one gets:

$$s_{11} = \frac{c_{11} + c_{12}}{(c_{11} - c_{12})(c_{11} + 2c_{12})} ,$$

$$s_{12} = \frac{- c_{12}}{(c_{11} - c_{12})(c_{11} + 2c_{12})} . \qquad (C.9)$$

In the absence of any applied electric field, the change in the dielectric impermeability due to the strain can be given as [52]:

$$\Delta B_{ij} = \sum_{r,s} p_{ijrs}\epsilon_{rs} \quad (r,s=1,2,3) \ , \tag{C.10}$$

where

$$p_{ijrs} = \sum_{k,l} \pi_{ijkl}c_{klrs} \quad (k,l=1,2,3) \ , \tag{C.11}$$

and

$$\pi_{ijkl} = \sum_{r,s} p_{ijrs}s_{rskl} \quad (r,s=1,2,3) \ . \tag{C.12}$$

The elastooptic coefficients p_{ijrs} are dimensionless, whereas the piezooptic coefficients π_{ijkl} have the dimension of stress. Both π and p follow the same matrix form in reduced notation as given in Eqn.(C.7).

Equation (C.12) can be written in the reduced form as:

$$\pi_{mn} = \sum_{r} p_{mr}s_{rn} \quad (r=1,2,\ldots,6) \ , \tag{C.13}$$

where m and n can take on values between 1 and 6. However, for cubic systems, as is the case here, the only possible values of non-zero and non-equal components are π_{11}, π_{12}, and π_{44}. The non-zero components are defined by the identities:

1) $\pi_{11} = \pi_{22} = \pi_{33}$,

2) $\pi_{12} = \pi_{23} = \pi_{31} = \pi_{13} = \pi_{32} = \pi_{21}$,

3) $\pi_{44} = \pi_{55} = \pi_{66}$.

The rest of the components are zero.

From Eqn.(C.13)

$$\pi_{11} = \sum_{r} p_{1r}s_{r1} \quad (r=1,2,\ldots,6)$$

$$= p_{11}s_{11} + p_{12}s_{21} + p_{13}s_{31} + p_{14}s_{41} + p_{15}s_{51} + p_{16}s_{61} .$$

Now, $s_{21} = s_{31} = s_{12}$, $p_{13} = p_{12}$, and $p_{14} = p_{15} = p_{16} = 0$. Therefore,

$$\pi_{11} = p_{11}s_{11} + 2p_{12}s_{12} . \qquad (C.14)$$

Similarly,

$$\pi_{12} = \sum_{r} p_{1r}s_{r2} \quad (r=1,2,\ldots,6)$$

$$= p_{11}s_{12} + p_{12}s_{22} + p_{13}s_{32} + p_{14}s_{42} + p_{15}s_{52} + p_{16}s_{62} .$$

Remembering the above relations and also $s_{22} = s_{11}$, the above equation reduces to:

$$\pi_{12} = p_{11}s_{12} + p_{12}(s_{11} + s_{12}) . \qquad (C.15)$$

Also,

$$\pi_{44} = \sum_{r} p_{4r}s_{r4} \quad (r=1,2,\ldots,6)$$

$$= p_{41}s_{14} + p_{42}s_{24} + p_{43}s_{34} + p_{44}s_{44} + p_{45}s_{54} + p_{46}s_{64} ,$$

which reduces to:

$$\pi_{44} = p_{44}s_{44} . \qquad (C.16)$$

The values of p_{11}, p_{12}, and p_{44}, as well as of c_{11}, c_{12}, and c_{44} are given in the paper by Booyens and Basson [47] and are shown in Table C.1.

Table C.1

The values of the elastooptic coefficients (p_{ij}) and the stiffness (c_{ij}) for GaAs after Booyens and Basson [47].

(p_{ij} are dimensionless, c_{ij} are in dyne/cm^2)

p_{11}	p_{12}	p_{44}	c_{11}	c_{12}	c_{44}
-0.165	-0.14	-0.072	118.8×10^{10}	53.8×10^{10}	59.4×10^{10}

The coefficients c_{ij} are easily converted to the s_{ij} by Eqns.(C.8) and (C.9). This yields $s_{11} = 1.1728 \times 10^{-12}$ cm^2/dyne, $s_{12} = -3.6558 \times 10^{-12}$ cm^2/dyne, and $s_{44} = 1.6835 \times 10^{-12}$ cm^2/dyne. Substituting for the values of s_{ij} obtained above and the values of p_{ij} from Table C.1 in Eqns.(C.14-C.16), one obtains the piezooptic coefficients as follows:

$$\pi_{11} = -9.115 \times 10^{-14} \text{ cm}^2/\text{dyne},$$

$$\pi_{12} = -5.269 \times 10^{-14} \text{ cm}^2/\text{dyne},$$

and $$\pi_{44} = -1.212 \times 10^{-13} \text{ cm}^2/\text{dyne}. \qquad \text{(C.17)}$$

However, for the π_{ij}, the following identities hold:

$$\pi_{mn} = \pi_{ijkl} \quad \text{when } n=1,2,3,$$

and $$\pi_{mn} = 2\pi_{ijkl} \quad \text{when } n=4,5,6.$$

Taking into account the above identities, the piezooptic coefficients for GaAs are given as:

$$\pi_{1111} = -9.115 \times 10^{-14} \text{ cm}^2/\text{dyne} ,$$

$$\pi_{1122} = -5.269 \times 10^{-14} \text{ cm}^2/\text{dyne} ,$$

and $$\pi_{1212} = -6.061 \times 10^{-14} \text{ cm}^2/\text{dyne} . \qquad (C.18)$$

D. Proof that pure screw dislocations cannot be viewed end-on

The coordinate system used to represent the stresses for a pure screw dislocation is shown in Fig.2.7. The sense of the dislocation is assumed to be along the x_3 direction, and the Burger vector is also along the x_3 direction as the Burger vector for a pure screw dislocation is parallel to the dislocation line. The sample axes system (x_1'', x_2'', x_3'') shown in Fig.2.9 is aligned with the stress axes system (x_1, x_2, x_3). For simplicity of expression, a (100) oriented sample is taken with the relation between the sample axes (x_1'', x_2'', x_3'') and the crystal principal axes (x_1', x_2', x_3') shown in Fig.2.10. The angle ϕ shown in Fig.2.10 can take on any value between 0° and 90°. The stresses associated with a pure screw dislocation is given by Eqns.(2.21-2.23). These stresses are converted to the sample axes system using Eqn.(2.32) with substitution of the direction cosines from Eqn.(2.30) and the results are given by:

$$\sigma_{11}'' = \sigma_{12}'' = \sigma_{21}'' = \sigma_{22}'' = \sigma_{33}'' = 0 \ ,$$

$$\sigma_{13}'' = \sigma_{31}'' = \sigma_{13} \ ,$$

and $$\sigma_{23}'' = \sigma_{32}'' = \sigma_{23} \ . \qquad (D.1)$$

These stresses are converted to the crystal principal axes system using Eqn.(2.36) with the direction cosines substituted from Eqn.(2.34) and the results are given by:

$$\sigma_{11}' = \sigma_{22}' = \sigma_{23}' = \sigma_{32}' = \sigma_{33}' = 0 \ ,$$

$$\sigma'_{12} = \sigma'_{21} = a'_{13}a'_{21}\sigma''_{13} + a'_{13}a'_{22}\sigma''_{23} ,$$

and $$\sigma'_{13} = \sigma'_{31} = a'_{13}a'_{31}\sigma''_{13} + a'_{13}a'_{32}\sigma''_{23} . \qquad (D.2)$$

The changes in the dielectric impermeability tensor elements are calculated using Eqn.(2.37) with the results given as:

$$\Delta B'_{11} = \Delta B'_{22} = \Delta B'_{23} = \Delta B'_{32} = \Delta B'_{33} = 0 ,$$

$$\Delta B'_{12} = \Delta B'_{21} = 2\pi_{12}\pi_{12}\sigma'_{12} ,$$

and $$\Delta B'_{13} = \Delta B'_{31} = 2\pi_{12}\pi_{12}\sigma'_{13} . \qquad (D.3)$$

These changes in the dielectric impermeability tensor elements are transformed back to the sample axes system by the transformation Eqn.(2.38) and the results are given by:

$$\Delta B''_{11} = \Delta B''_{12} = \Delta B''_{21} = \Delta B''_{22} = \Delta B''_{33} = 0 ,$$

$$\Delta B''_{13} = \Delta B''_{31} = a'_{21}a'_{13}\Delta B'_{12} + a'_{31}a'_{13}\Delta B'_{13} ,$$

and $$\Delta B'_{23} = \Delta B'_{32} = a'_{22}a'_{13}\Delta B'_{12} + a'_{32}a'_{13}\Delta B'_{13} . \qquad (D.4)$$

The light is incident along direction - x''_3 as the dislocation is being viewed end-on. Hence, the cross-section the incident light faces can be obtained by expanding the indicatrix given in Eqn.(2.39) and substituting $x''_3 = 0$. The result is given by:

$$(B_0+\Delta B''_{11})x''^2_1 + (B_0+\Delta B''_{22})x''^2_2 + 2\Delta B''_{12}x''_1x''_2 = 1 . \qquad (D.5)$$

However, one can see from Eqn.(D.4) that $\Delta B''_{11} = \Delta B''_{12} = \Delta B''_{22} = 0$. Hence, Eqn.(D.5) reduces to:

$$B_0x''^2_1 + B_0x''^2_2 = 1 , \qquad (D.6)$$

which is the equation of a circle, and, hence, there is no birefringence associated with it. Therefore, it is proved that a pure screw dislocation cannot be viewed end-on, i.e., along the dislocation line.

VITA

Aloke Kumar Dutta was born in Calcutta, India on November 24, 1960. He received his Bachelor's degree in Electrical Engineering from Jadavpur University, Calcutta, India, in 1982. He came first in the order of merit in the Bachelor of Engineering final examination held in May 1982 at Jadavpur University, Calcutta, India, and was the recipient of five medals. Then he worked in an Engineering Consulting Company in India for a year and a half. He joined Louisiana State University, Baton Rouge, in the Spring of 1984 and received his Master's degree in the Summer of 1985. Since then, he has been pursuing the doctoral degree under the supervision of Dr. Pratul Ajmera. His research was awarded the best research prize among all the doctoral students in the College of Engineering at LSU in 1987-88. He was a research and teaching assistant in the Department of Electrical and Computer Engineering. He is a member of Eta Kappa Nu, Phi Kappa Phi, and a student member of IEEE.

He is presently a candidate for the degree of Doctor of Philosophy in the Department of Electrical and Computer Engineering.

DOCTORAL EXAMINATION AND DISSERTATION REPORT

Candidate: Aloke Kumar Dutta

Major Field: Electrical Engineering

Title of Dissertation: Use of Infrared Piezobirefringence for Observation of Dislocations in Semiconductors with Cubic Symmetry

Approved:

P. K. Gimerra
Major Professor and Chairman

F. Glen Kemberg
Dean of the Graduate School

EXAMINING COMMITTEE:

Burke Hanes

Ayhan Ltk

A. Elamawy

William O'Hara

J R Dorroh

Date of Examination:

November 13, 1989